A study on inclusions in ice layers formed by melting and refreezing processes in ice cores

アイスコアに含まれる融解再凍結によって形成された

氷板内の不純物に関する研究

Kaoru KAWAKAMI

Ph. D. Dissertation

Graduate School of Environmental Science
Hokkaido University

March 2023

Abstract

Recent Arctic warming has accelerated the surface melting in the Greenland ice sheet. In the percolation zone, meltwater percolates and refreezes in the snowpack and is detected mainly as ice layers in ice cores drilled in these regions. The melting and refreezing processes redistribute impurities originating from atmospheric aerosols and disturb proxies in the ice cores. Although bulk analyses, such as ion concentrations in the ice layers, were discussed at the 10^2 mm order, how the formation of ice layers in the ice core disturbs the proxies is not understood in detail. In order to properly understand environmental proxies in the context of increasing surface melting and associated ice layer formation due to global warming, it is important to understand the characteristics of inclusions in the ice layers. In this study, the location, size, and chemical composition of inclusions were analyzed with two ice cores drilled in different regions of the Greenland ice sheet with 10^{-3} to 10^2 mm scale. Then it is discussed how the inclusions in ice layers are redistributed during melting and refreezing processes. The aim of this study is to establish new proxies that reflect the environment when ice layers were formed.

The SIGMA-A ice core in northwestern Greenland (60 m depth) and the SE-Dome II ice core in southeastern Greenland (250 m depth) were analyzed. First, the depth-age scales were established, and then the annual accumulation rates were determined. The age and thickness of the ice layers were also detected from visual observation and photography using transmitted light. The ice layer samples were then melted under clean conditions and analyzed for ion concentrations and water isotope ratios in the meltwater. The inclusions in ice layers were observed with a measuring microscope in a cold room (−22 °C), and the chemical compositions of the inclusions were identified with a Raman spectroscopy (−30 °C). Ice layer samples were sublimated at −22 ºC to extract nonvolatile inclusions as residues, and the location, size, and elemental composition of the nonvolatile inclusions were analyzed by scanning electron microscope and energy dispersive X-ray spectroscopy.

Ice layers greater than 1 mm in thickness were found in 243 layers (average thickness of 14 mm) in the SIGMA-A core (1903–2017) and 89 layers (average thickness of 10 mm) in the SE-Dome II ice core (1799–2020). The number and thickness of ice layers in both cores and melt feature percentage (MFP) have increased with rapid warming in the Arctic since 1995. The ice layers in the SIGMA-A core contain inclusions greater than 30 μm in diameter, which are formed by melting and refreezing processes, and were classified into three types based on their shapes:

particle-like, rod-like, and columnar-like inclusions. Columnar-like inclusions are within ice grains that consist of $CaSO_4 \cdot 2H_2O$ (gypsum). Rod-like inclusions in grain boundaries contain brine with mainly Cl^- and Na^+. Particle-like inclusions have both characteristics. Rod-like inclusions were 100–1000 μm in diameter, suggesting that they were formed at the last of the freezing with large amounts of meltwater containing Cl^- and Na^+.

For the SE-Dome II ice core, inclusions greater than 30 μm in diameter were also detected in the ice layers, and rod-like inclusions with about 0.5 mm in diameter were detected. In the ice layers of the SIGMA-A ice core and the SE-Dome II ice core, rod-like inclusions were commonly detected. However, the chemical compositions of rod-like inclusions are different, as the rod-like inclusions of SIGMA-A ice core contain much more Na and Cl, whereas those of SE-Dome II ice core contain much more S. The difference in chemical composition is attributed to the difference in ion balance of the meltwater forming the ice layers of both ice cores, suggesting that the chemical composition of rod-like inclusions reflects ion species and concentrations in the meltwater. This study proposes that rod-like inclusions are a proxy for melting and refreezing in past warm periods and their chemical compositions reflect the ion species and balances in the meltwater.

Contents

1 Introduction

1.1 Greenland ice sheet and ice cores

In the Arctic, the temperature has dramatically changed over the last two centuries. The cold period, called the Little Ice Age, lasted from the 14th century to the last half of the 19th century (Kaufman et al., 2009). Then, warming accelerated in the 1920s (Chylek et al., 2006), and reached a maximum around 1940 (Johannessen 2004). Afterward, temperature declined through the 1960s and 1970s, followed by rapid warming after 1995, and the warming trend has continued to the present (Serreze et al., 2006). Based on model analyses by Aizawa et al (2021; 2022), the warm period of the first half of the 1900s was mainly due to natural variability, which was a combination of the increase of temperature and low volcanic activities. The subsequent cold periods in the 1960s and 1970s were attributed to anthropogenic factors resulting from increased emissions of anthropogenic aerosols, and the acceleration of warming after 1995 was reported to be due to the increase in anthropogenic greenhouse gases. In the future, Arctic temperature rises will be more than twice the global average (IPCC AR6, 2021), and natural environment and human activities will be affected.

Glaciers and ice sheets which are located in high elevation mountain areas or high latitude, are formed by snow accumulated over many years and are compacted by its own weight. Glaciers and ice sheets lose its permeability at a certain depth and turns into ice. In the upper areas of the glaciers and ice sheets, there is an accumulation zone where snow accumulate, in the lower areas, and an ablation zone where snow and ice melt (Benson, 1962, Muller, 1962). The accumulation area is further divided into four zones: superimposed ice zone where the annual increment of superimposed ice exposed at the surface, wet snow zone where the snow deposited since the previous summer raised to 0 °C, a percolation zone where snow accumulates and melts during high summer temperatures, and a dry snow zone where snow does not melt (Paterson, 2006; Kameda and Takahashi 2014).

The Greenland ice sheet, located in the Arctic region, is the second largest ice mass in the world, covering approximately 78% of Greenland (1.7 million km^2) (Kameda and Takahashi 2014). Surface temperature on the ice sheet have increased by 0.5°C during 2000–2012 with recent Arctic warming (Hall et al., 2013). The rate of ice sheet mass loss has increased with a loss

of about 210 Gt yr^{-1} from 2003 to 2008 (equivalent to about 0.6 mm yr^{-1} of sea level rise) compared to a loss of about 55 Gt yr^{-1} from 1993 to 1999 (Krabill et al., 2004), a nearly fourfold increase in loss (Shepherd et al., 2012). Thus, mass loss of the Greenland ice sheet has become more severe in recent years (van den Broeke et al., 2016, Otosaka et al., 2020). The main factor of mass loss has changed with the progression of warming (Tedesco et al., 2015), and while before the progression of warming the main driver was the discharge of ice bodies into the ocean due to the flow of the ice itself, after the progression the main driver is considered to be the change in surface mass balance (SMB) due to the accumulation and ablation on the ice sheet (e.g., van den Broeke, 2006; Enderlin et al., 2014). Temporal accumulation variations are considered to be the primary factor driving interannual elevation (and SMB) variations in inland Greenland (McConnell et al., 2000), while variations in meltwater runoff are considered to have an important influence on SMB at the ice sheet margin.

Ice cores drilled in the Greenland ice sheet are one of the archives that preserve past environmental information in the Arctic region. After the first ice core drilled at Camp Century in 1966, deep ice cores were drilled at DYE3 (Clausen and Hammer, 1988), GRIP (Johnsen et al., 1995), NGRIP (Dahl-Jensen et al., 2002), and NEEM (NEEM community members, 2013) to depths greater than 1000 m. These deep ice cores have provided a wide range of data on climate and environmental changes over the past few thousand to tens of thousands years. For example, these ice cores reveal cold and warm cycles during the last glacial period (e.g., Dansgaard et al., 1982; Rasmussen et al. 2014). In northern Greenland, the warmest period was reported around 126,000 years ago, corresponding to the beginning of the last interglacial, when temperatures were about 8°C higher than at present (NEEM community members, 2013).

In addition to the deep ice cores mentioned above, shallow ice cores of several tens to several hundred meters have been drilled in various locations to reconstruct climatic and environmental changes over the past several decades to several hundred years. Shallow cores include, for example, the Site J ice core (Kameda et al., 1995), the ACT-3 ice core (Keegan et al., 2014), and the SE-Dome I ice core (Iizuka et al., 2017). The PARCA (Program for Arctic Regional Climate Assessment) project drilled shallow ice cores over a wide area of Greenland to investigate the spatial distribution of annual accumulation rate in the Greenland ice sheet over the past few decades (Mosley-Thompson et al., 2001). Using shallow ice cores, annual layers can be determined with ease by variations in water stable isotope ratios and other factors described below,

allowing to reconstruct accumulation rates and concentrations of chemical constituents on a seasonal scale. In addition, the obtained results can be compared with meteorological observation data, reanalysis data, and satellite observation data, allowing discussion of past climatic and environmental changes at high resolution.

1.2 Age scale and accumulation rate reconstructed from Greenland ice cores

In order to interpret paleoclimate proxies preserved in ice cores, it is essential to determine the precise relationship between ice age and depth (hereafter as age scale) (e.g., Meese et al. 1997). The age scale and density profiles are able to reconstruct the accumulation rate, which is one of the basic parameters that the reanalysis data and climate model cannot reconstruct and essential for reconstruction of the flux of chemical species in the ice cores. Thus, age scale and accumulation rate are important for ice core studies.

The age scales of ice cores can be reconstructed by using a specific time marker layer or annual layer counting. Natural and anthropogenic events, which are detected in several Greenland ice cores, can be used as specific time markers. Large-scale or high-latitude volcanic eruptions are preserved in the ice cores as large amounts of sulfate and volcanic ash layer, which can be detected in ice core, as peaks in electrical conductivity and dielectric constant (Hammer, 1980; Clausen et al., 1997; Mojtabavi et al., 2020) by the continuous dielectric profile (DEP) method (Moore et al. 1987; Wilhelm et al., 1998), or sulfate concentrations peaks (Rasmussen et al., 2008) by ion analysis. In addition, volcanic identity can be confirmed by the tephra of the volcanic ash layer that is chemically and stratigraphically consistent with the sediments of the presumed original volcano (Zielinski et al., 1994; Abbott and Davies., 2012; Bourne et al., 2015; Cook et al., 2018). Nuclear materials originating from H-bomb test, reaching its peak in 1963, have been recorded as tritium peaks and are particularly useful for shallow ice cores (Qiao et al., 2021). Other reference layers are melt features, especially formed during extreme surface melting in 2012 (Westhoff et al., 2022), which are detected by visual observations, or a continuous density profile measured using for example the X-ray transmission method (Hori et al., 1999).

As annual layer counting, seasonal variations in water isotope ratio and ion concentrations have been used to establish age scales for many ice cores (e.g. Dansgaard, 1964). Hydrogen peroxide (H_2O_2) is often used as a robust tool for annual layer counting because of its clear seasonality following solar cycle (e.g., Sigg and Neftel, 1988; Frey et al., 2006). However,

in low accumulation sites where longtime records are expected in ice cores, H_2O_2 in ice suffer from post-depositional effects such as remobilization in firn and decomposition by dust, which hamper precise dating by making its seasonal cycle unclear (Anklin et al., 1998; Gfeller et al., 2014). By contrast, it has been shown that, in case of Antarctic ice cores, the H_2O_2 seasonal signal is clearly preserved to a few hundred years at high accumulation sites where the accumulation rate exceeds ~0.3 m (Frey et al., 2006). It is therefore expected that ice cores at high accumulation site in Greenland can be also dated using H_2O_2.

Accumulation rate on the Greenland ice sheet has been studied using a variety of methods, including ice cores, snow-pit observations, radar observations, and climate modeling. The accumulation rate shows regional variations in Greenland ice sheet. For example, Karlsson et al (2020) conducted radar observations between the northern NGRIP and NEEM sites from 2007 to 2015 and reported accumulation rates of 0.11–0.26 m w.e. yr^{-1}. Miège et al (2013) also measured accumulation rates in the southern region by ice cores and reported a maximum accumulation rate of 1.26 m w.e. yr^{-1}. According to a regional climate model (RCM), the accumulation in the southeast is about 30% of the total accumulation in the Greenland ice sheet (Burgess et al., 2010). Therefore, interannual variations in accumulation in this region strongly influence the surface mass balance of the entire Greenland ice sheet (Burgess et al., 2010). However, the limited field observations of accumulation in the southeast make it difficult to assess accumulation rates and patterns with climate models. In fact, of the accumulation reconstructed by the climate model, the southeastern region has large discrepancies, with a maximum of 2.0 m yr^{-1} (Fettweis et al., 2020). Therefore, detailed field observations of accumulation rates, particularly in the southeastern region, are needed.

1.3 Reconstruction of paleoclimate from Greenland ice cores

Aerosols are micro droplets or particles with liquid or solid phase in the atmosphere, which are classified into two categories: natural aerosols and anthropogenic aerosols. The anthropogenic aerosols are detected for the last 200 years with increasing human activity. In the Arctic, natural aerosols include NaCl (sea salt; e.g. Legrand and Mayewski, 1997), $CaSO_4$ (terrestrial materials; e.g. Legrand and Mayewski, 1997), $(NH_4)_2SO_4$ and NH_4NO_3 (biomass burning or bacterial decomposition in soils; Silvente and Legrand, 1993; Hansson and Holmén, 2001), H_2SO_4 (marine biogenic materials or volcanic materials; e.g. Hansson and Saltzman, 1993). Arctic regions are located in a close proximity to the northern mid-latitude areas with high human activity, which supplies anthropogenic aerosols such as nitrogen oxides (NOx), sulfate oxides (SOx), black carbon (BC). Natural aerosols are characterized by relatively large particle sizes (> 30 μm in diameter), whereas anthropogenic aerosols are sub μm, and both are seldom larger than 30 μm in diameter (Whitby, 1978).

After dry or wet deposition on the ice sheet, aerosols are incorporated into the interior of the ice as impurities. Thus, the impurities from the past to the present can be extracted from ice cores drilled in the ice sheet, which are used as proxies to reconstruct the paleoenvironment, including the transport process and origin of impurities. The chemical composition of impurities preserved in ice cores and their time-series variations have been discussed by melting ice cores with every 10^2 mm order and measuring the bulk concentrations of major cations and anions in the meltwater (e.g., Iizuka et al., 2002; Mayewski, 1993).

The origin and peak timing of major ionic components are summarized in the following. Ca^{2+} originated from terrestrial dust has a peak in late winter to spring (Legrand and Mayewski et al.,1997; Kuramoto et al., 2011), which has been increasing since 2000 (e.g., Iizuka et al., 2018; Nagatsuka et al., 2021). Na^+ and Cl^- originate from sea salt, peaking in winter to early spring (Beer et al., 1991; Davidson et al., 1993; Kuramoto et al., 2011; Gfeller et al., 2014; Curtis et al., 2018). NH_4^+ originates mainly from natural sources such as bacterial decomposition and biomass burning, peaking in the summer (Whitlow et al., 1992, Fuhrer et al., 1996, Legrand and Mayewski, 1997, Kuramoto et al., 2011). Both NO_3^- and SO_4^{2-} have natural and anthropogenic sources. Natural NO_3^- originates from biomass burning and bacterial decomposition, and lightning, which has a strong peak in the summer (Fuhrer et al., 1996; Silvente and Legrand., 1993; Hansson and

Holmén, 2001; Fischer et al., 2015). The natural source SO_4^{2-} is from marine biogenic activity and continental biogenic emissions, peaking in the summer (Kuramoto et al., 2011). The anthropogenic NO_3^- and SO_4^{2-} originates from human activities such as fossil fuel combustion, both of which peak in winter to early spring (e.g. Beer et al., 1991; Kuramoto et al., 2011). The emissions of the anthropogenic NO_3^- and SO_4^{2-} was at a maximum from 1970s to 1980s (Fischer et al., 1998).

Bulk ion concentration analysis described above is well suited for tracking seasonal and interannual variations in chemical compositions derived from atmospheric aerosols. However, this method has the disadvantage of melting ice core samples with about 10^2 mm order, which results in the loss of original information on the chemical composition and size of each impurity, which is useful for estimating the transport process and origin. Therefore, as described in the section 1.4, methods for analyzing impurities in ice cores have been established without melting ice core samples.

In the percolation zone of the accumulation area, summer meltwater percolates into the snowpack and refreezes to form the ice layer (Benson, 1962; Koerner, 1977; de la Peña et al., 2015; MacFerrin et al., 2019). The ice layer has been observed and discussed by radar (e.g., Otosaka et al., 2020), satellite remote sensing (e.g., Tedesco et al., 2013), climate models (e.g., MacFerrin et al., 2019) and ice cores (Fujita et al., 2021). In a percolation zone, ice layers can cause meltwater to runoff much more rapidly, increasing the mass loss and associated sea-level rise (Culberg et al., 2021). Thus, it is important to determine how ice layers respond to a warming trend, particularly with the occurrence of Arctic amplification of global warming (e.g., AMAP, 2017). Direct measurements of ice layers involve analyzing ice cores drilled in the ice sheet to determine the melt-feature percentage (MFP), which is then used to reconstruct the history of such surface melting (e.g., Langway, 1967; Koerner, 1977; Herron et al., 1981; Koerner and Fisher, 1990; Kameda et al., 1995; Graeter et al., 2018; Fujita et al., 2021). The number and thickness of ice layers have been increasing with warming, and ice layer thickness has been considered an indicator of summer temperatures (Kameda et al., 1995). After examining recent Greenlandic ice cores, Graeter et al (2018) argued that a warming of 1.2 °C in the summertime led to a near doubling of the MFP in 1995–2015 compared to that in 1870–1900. Moreover, on 14 August 2021, rain fell at the summit area of Greenland, the areas first rain in recorded history that dates from 1950 (Scambos et al., 2021), implying that even such a dry snow zone may someday be a

percolation zone (e.g., McGrath et al., 2013).

The recent Arctic warming should affect not only the thickness but also the chemical impurity content of the ice layers. In the case of snowpack melt, ionic species eluted with different efficiencies. Previous studies (e.g. Eichler et al., 2001; Li et al., 2017) discussed the patterns of the concentration ratios the elution sequence and for example $SO_4^{2-} > Ca^{2+} \sim Mg^{2+} > Na^+ > NO_3^- > NH_4^+ > Cl^-$ was established (Eichler et al., 2001). By different efficiencies, Iizuka et al (2002) suggests that Mg^{2+} / Na^+ can be a proxy in refrozen ice such as ice layers. Assuming that Mg^{2+} / Na^+ in snowfall is equal to the sea-salt ratio (0.11), the high Mg^{2+} / Na^+ ratio in the ice layer is likely due to the inflow of meltwater and refreezing (e.g., Iizuka et al., 2002). If meltwater refreezing is incomplete (e.g., Ashmore et al., 2019), then the resulting runoff flushes out chemical impurities from the refrozen meltwater (e.g., Cragin et al., 1993). Such flushing points to the importance of understanding the chemical characteristics of ice layers, particularly in the inclusions formed by melting-refreezing processes. However, determining how the ice layers response during melting and refreezing requires knowledge of their chemical composition and inclusion properties, both of which are presently lacking.

1.4 Inclusions preserved in ice cores

SEM (scanning electron microscope)–EDS (energy dispersive X-ray spectroscopy) and Raman spectroscopy have been used as tools to analyze the size, location, and chemical composition of inclusions in ice cores without melting them (Ohno et al., 2005; 2006; Stoll et al., 2020). For example, Mulvaney et al. (1988) used SEM– EDS microanalysis on polar ice from Antarctica to show that H_2SO_4 concentrations are several orders of magnitude higher at triple junctions than in grain interiors. A similar finding was later made for H_2SO_4 and HNO_3 using Raman spectroscopy (Fukazawa et al., 1998). In addition, solid Na_2SO_4 and $CaSO_4$ salts in ice grains have been found in polar ice from Antarctica using Raman spectroscopy (Ohno et al., 2005, 2006; Sakurai et al., 2011). The use of SEM–EDS also showed the inclusions were mainly in triple junctions and grain boundaries, with Na and Cl primarily in the Greenland ice core (GISP2), whereas Mg and S were primarily in an Antarctic ice core (Byrd) (Cullen and Baker, 2001; Obbard et al., 2003). Using a similar method, Stoll et al. (2020) reported that insoluble inclusions are often found in the grain interior, whereas soluble inclusions occur at both the grain boundaries and grain interior. Iizuka et al. (2009) established a sublimation method that can statistically measure the chemical composition of soluble and insoluble inclusions extracted by sublimation of ice core samples. The diameter of inclusions detected by the method described in Iizuka et al (2009) is less than 30 μm. All of the above studies were conducted on ice cores that had not experienced melting.

However, for an ice core with melting, these methods have yet to be applied. With melt-refreezing, the inclusions in meltwater become concentrated in the liquid phase during freezing, collecting mainly in the triple junctions in the last region of freezing (e.g., Takenaka et al., 1996; Bartels-Rausch et al., 2014). However, there is little understanding of the chemical characteristics of inclusions distributed by the refreezing. Therefore, it is essential to investigate how inclusions are distributed and preserved in the ice layer.

1.5 Objective of this study

Recent Arctic warming has accelerated the melting of the Greenland ice sheet. Meltwater in the percolation zone refreezes in the snowpack and is detected mainly as ice layers in ice cores. The melting and refreezing processes redistribute inclusions originated from atmospheric aerosol and disturb the proxies in the ice layers. However, the extent to which ice layers in ice cores disturb proxies can only be discussed by so-called bulk analyses such as ion concentrations in the ice layers, and not by spatial information such as where and in what form inclusions are preserved in the ice layers, or chemical composition. In order to properly understand proxies in the context of increasing surface melting and associated ice layer formation due to global warming, it is important to characterize the inclusions in the ice sheet. Therefore, in this study, two ice cores from Greenland were used to observe the number and thickness of ice layers, in addition to the basic physical and chemical data obtained from the ice cores, such as density, electrical conductivity, and ion concentrations. Then micro-Raman spectroscopy and sublimation techniques were used to analyze the size, location, and chemical composition of inclusions in ice layers with the 10^{-3} –10^{2} mm scale, and discussed how impurities in ice layers are redistributed. This study aims to establish a new environmental proxy that can reconstruct the atmospheric environment at the time of ice layers formed.

2 Methods

The analyses of ice layers were performed on the SIGMA-A ice core drilled in the northwestern Greenland (78°03′06″N, 67°37′42″W, 1490 m a.s.l.), and the SE-Dome II ice core drilled in southeastern Greenland (67°19′17″ N, 36°47′03″ W, 3160 m a.s.l.) (Figure 2-1). With the following method, the ice cores were analyzed in order to determine the age of the ice, reconstruct accumulation rate, and analyze the inclusions in ice layers. The ice cores and methods are summarized in the Table 2-1.

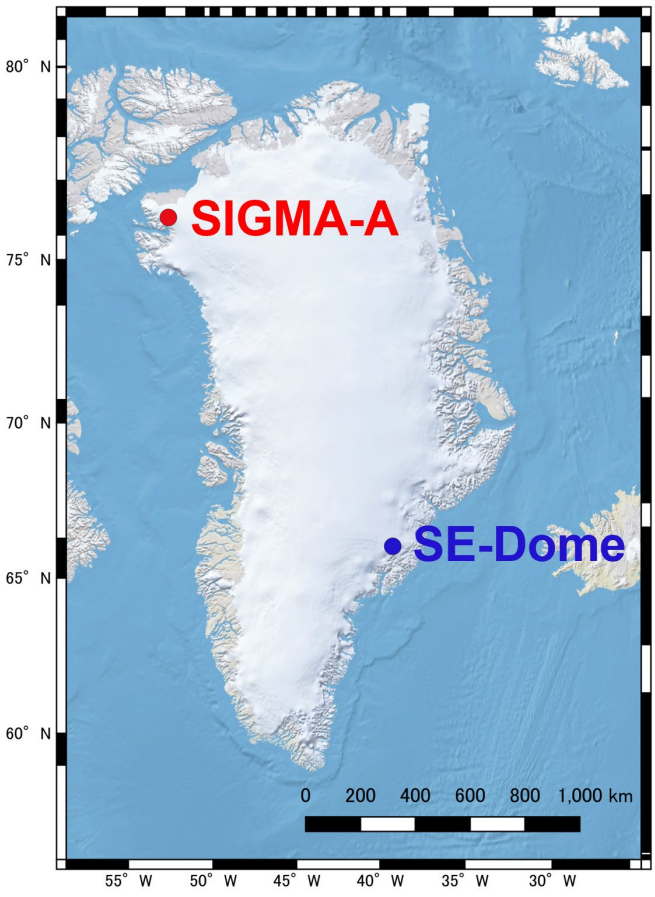

Figure 2-1 The map of the SIGMA-A site (78º 03′06″N, 67º 37′42″W, 1490 m a.s.l.) and the SE-Dome II site (67°19′17″ N, 36°47′03″ W, 3160 m a.s.l.).

Table 2-1. The methods applied to the two ice cores, the SIGMA-A ice core and the SE-Dome II ice core.

	SIGMA-A	SE-Dome II
Entire ice core		
Melt feature observation	○	○
Bulk density	◊	○
High-resolution density	◊	○
DEP	◊	○
Tritium concentration	◊	○
H_2O_2 concentration	×	○
Ion concentration	◊	○
Water isotope ratio	◊	×
Ice layer		
Microscope observation	○	○
Raman measurement	○	○
Sublimation and SEM-EDS analysis	○	○
Detailed ion concentration	○	×
Detailed water isotope ratio	○	×

○: This study

◊: Previous study (Kurosaki et al., 2020)

×: Not shown in this study

2.1 SIGMA-A ice core

Between 23–28 May 2017, a 60.19 m ice core was drilled near the SIGMA-A observation site (78°03′06″N, 67°37′42″W, 1490 m above sea level (a.s.l.); Figure 2-1) in northwestern Greenland (Matoba et al., 2018). The site lies on the ridge of the Hayes Peninsula, 70 km northeast of the seaside village of Qaanaaq, in a percolation zone with an estimated annual average accumulation rate of 0.25 to 0.40 m yr^{-1} between 1903 and 2005 (Kurosaki et al., 2020). The temperature at 20 m depth is −18.9 °C. The SIGMA-A ice core consisted of 124 sections, with an average section length of 0.48 m. Each SIGMA-A core section was cut to ~30 mm thickness with a band saw (Ryowa, BSW-200), and its surface was then microtomed to obtain parallel planes for physical observation in a cold room of the Institute of Low Temperature Science at Hokkaido University, Japan (Figure 2-2). The SIGMA-A ice core was dated reliably during 1903–2005 by examining the measured $\delta^{18}O$, high resolution density with X-ray transmission method, electric conductivities, and tritium content (Kurosaki et al., 2020).

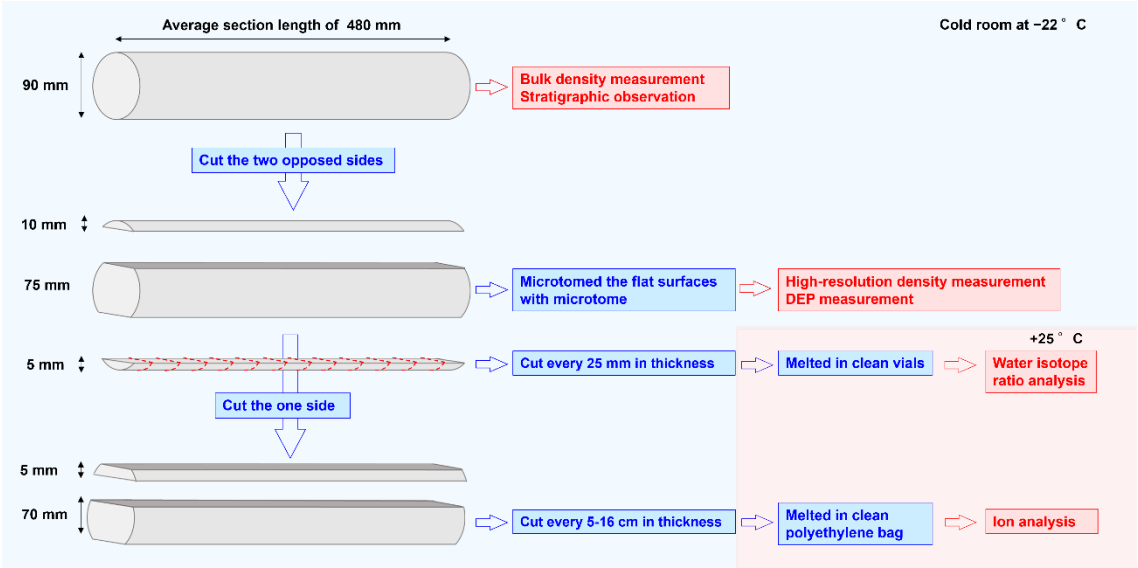

Figure 2-2 Cutting and analysis plan for the SIGMA-A ice core.

2.2 SE-Dome II ice core

Between 12 May – 2 June in 2021, a 250.79 m-long ice core (hereafter SE-Dome II ice core) was drilled at SE-Dome in south-east Greenland (67°19′17″ N, 36°47′03″ W, 3160 m a.s.l.; Figure 2-1). The details of the ice core drilling were described in Iizuka et al (2021). The SE-Dome II ice core consisted of 552 sections, with an average section length of 0.45 m. The top depth of the SE-Dome II ice core is 1.27 m from the ice sheet surface. After melt features observation (section 2.3.1) and bulk density measurement (section 2.3.2), one lateral side of the ice core section was cut 10 mm from 1.27 m to 88.8 m depth and 7 mm from 88.8 m to the 252.06 m depth, and the opposite side was cut 7 mm parallel from 1.27 m to 252.06 m depth with a band saw (Figure 2-3). Its surfaces were then microtomed to obtain parallel flat surfaces for physical analyses and made 552 ice sections by equalizing the thickness with an average of about 75 mm. The average thickness of 189 ice sections was 74 mm (above 88.8 m) and that of 363 sections was 77 mm (below 88.8 m).

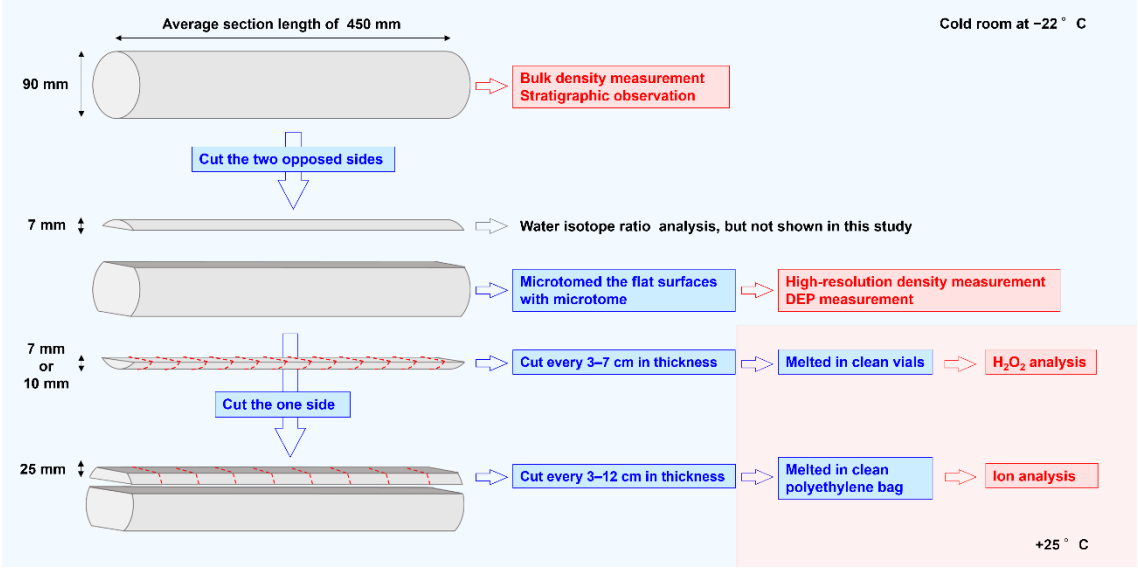

Figure 2-3 Cutting and analysis plan for the SE-Dome II ice core.

2.3 Measurements with the entire ice core

2.3.1 Melt feature observations

Each SIGMA-A ice core sections was observed and photographed on the LED Daylight with 920 lm (Elpa, ALT-1090IR(D)) using a Nikon D3300 camera in a cold room (−22 °C). For the SIGMA-A ice core, ice layers more than 1 mm in thickness were observed. Also, each SE-Dome II ice core section was observed on the LED Daylight with 920 lm (Elpa, ALT-1090IR(D)) in a cold room (−22 °C). Then, melt features were divided into three types: (1) 'ice layer' originating from refrozen aquifer (Figure 2-4a) with more than 1 mm in thickness, (2) 'layer with percolated ice (LPI)' consisting of refrozen meltwater during percolation without forming an aquifer (Figure 2-4b) with more than 1 mm in thickness, and (3) 'thin ice layer' of unknown origin with 1 mm or less in thickness (Figure 2-4c) were also observed. Each section was photographed using a Nikon D3300 camera in a dark cold room (−22 °C). As described in Figure 2-4, the firn was darker than the blight melt features due to the lower transmittance of light in firn.

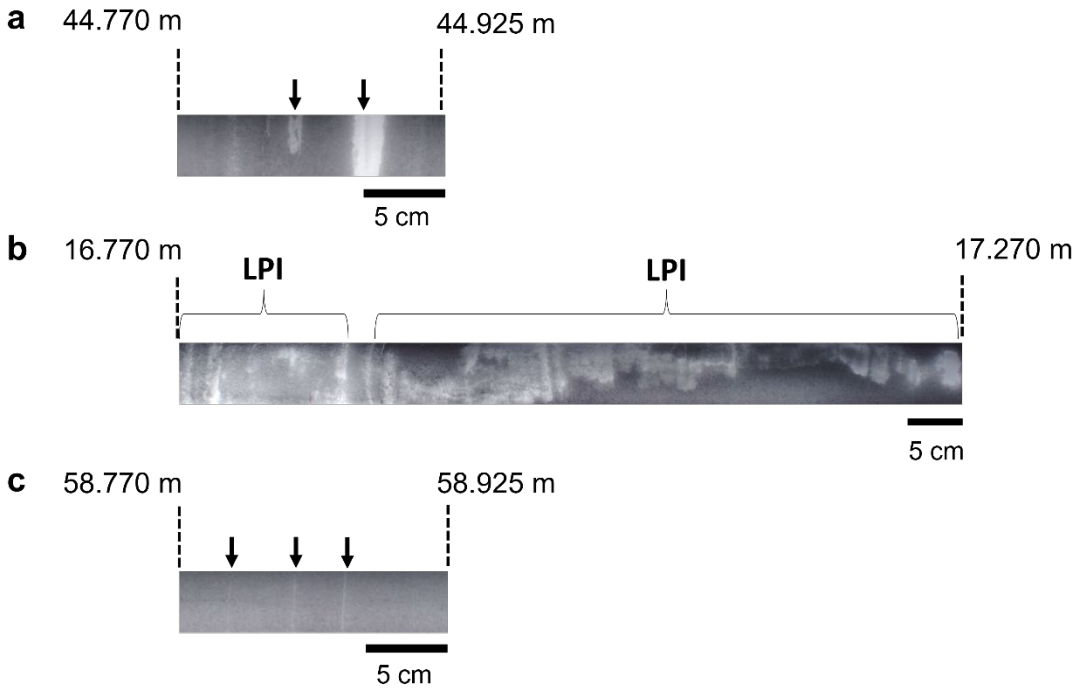

Figure 2-4 The examples of (a) the ice layer (> 1 mm), (b) the layer with percolated ice (LPI; > 1 mm), and (c) the thin ice layer (≤ 1 mm). The example photograph was all from the SE-Dome II ice core.

2.3.2 Density measurements

For the SIGMA-A ice core, the bulk density and high-resolution density was reported in Kurosaki et al (2020). The bulk density of each section from the SE-Dome II ice core was measured by the weight and size of the cores (volumetric method). In addition, a continuous density profile of the microtomed core was measured using the X-ray transmission method (Hori et al., 1999). In this method, the intensity of X-rays transmitted through a core sample was continuously measured using an X-ray detector during the translation of the sample across the beam. The X-ray intensity profile was then converted into a density profile using a calibration curve for X-ray absorption based on ice thickness. The spatial resolution of the density profile was approximately 1 mm.

2.3.3 Continuous dielectric profile (DEP)

To detect volcanic events, electrical conductivity on the whole sections of the SE-Dome II ice core was measured by the continuous dielectric profile (DEP) method (Moore et al. 1987; Wilhelm et al., 1998) with an average temperature of −22 °C. This method produced a profile of electrical conductivity at 250 kHz and provided the signal of the acid content (Wollf et al., 2020). The spational resolution was 10 mm. The electrical conductivity of the SIGMA-A ice core was measured in Kurosaki et al (2020).

2.3.4 Tritium measurement

The tritium content was determined using a liquid scintillation counter (LSC-LB3, Aloka Co. Ltd.). 24 samples from 76.831 m to 89.750 m in depth from the SE-Dome II ice core were measured. The average length of the samples was 565mm, corresponding to a half-year time resolution. The tritium content of the SIGMA-A ice core was reported in Kurosaki et al (2020).

2.3.5 H_2O_2 concentration measurement and dating of the ice core

Samples of 10 or 7 mm thickness were measured for H_2O_2 concentrations at the depth resolutions of 3–7 cm (Figure 2-3) for the determination of H_2O_2 concentrations to establish age scale by assuming that minimal and maximal in H_2O_2 correspond to mid-winter and mid-summer, respectively (Figure. 2-5; Hattori et al., 2021 and Wang et al., 2021). Total sample number was 4968 covering the whole SE-Dome II ice core. The samples were put into pre-cleaned 15 mL tubes and melted at room temperature (+25 °C). H_2O_2 concentrations were determined by the

fluorometric method (Lazrus et al., 1985). Briefly, the water samples were transferred by autosampler and peristaltic pump to a continuous flow system, in which the fluorescent dimer is produced via the reaction of H_2O_2 with 4-ethylphenol catalyzed by enzyme peroxidase, and detected by a fluorescent detector (Jasco, FP-4025) at an excitation and emission wavelengths at 326 nm and 410 nm, respectively, at pH > 12. The reproducibility was estimated by analyzing 20 sets of standard samples ranging 0–350 μg kg^{-1}, which were also used to calibrate 140 samples in a measurement day. The uncertainty varied depending on the concentration of standards: ± 2.1 ppb and ± 7.4 ppb for 8.75 ppb and 350 ppb standards, respectively. Absolute concentration of liquid H_2O_2 standard was determined by titration with $KMnO_4$ at the beginning and end of the measurement period (three months), which showed little decay (<5%). The H_2O_2 measurements were not conducted with the SIGMA-A ice core.

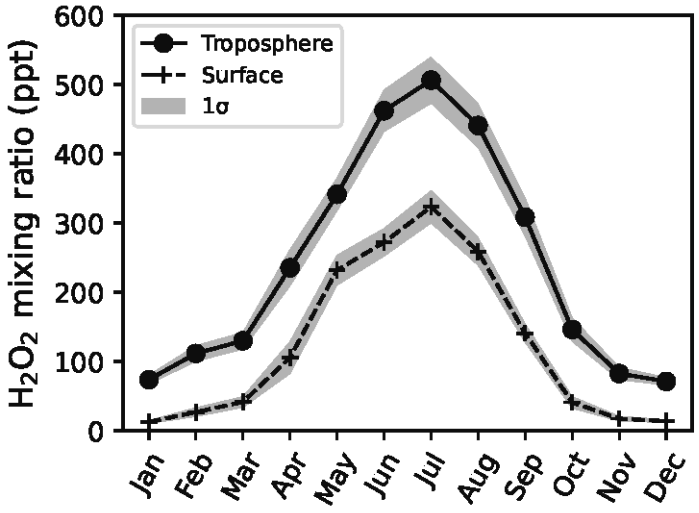

Figure 2-5 The seasonality of atmospheric H_2O_2 mixing ratio simulated by the GEOS-Chem global chemistry transport model (version 12.5; see Hattori et al. (2021) and Wang et al. (2021) for details) (Ishino, personal communication). The dots and crosses show tropospheric and surface layer H_2O_2 mixing ratios averaged within the area where air mass reaching the SE-Dome travels within 3 days (longitude: 70°W to 0°, latitude: 55 to 80°N). The plots and grey shade are the mean and 1σ standard deviation among the model output of different five years (1960, 1973, 1986, 1999, and 2013).

2.3.6 Ion concentration and water isotope ratio

The SE-Dome II ice core was cut in a cold room (−22 ºC) into 2656 samples with depth intervals 30–120 mm for analysis of the ion concentration (Figure 2-3). Samples were decontaminated by shaving off the surface using a clean ceramic knife in a cold clean room (class 10000) and put into cleaned polyethylene bags. The bagged ice was melted at room temperature in a clean room (+25 ºC). Major ion concentrations of $CH_3SO_3^-$, Cl^-, SO_4^{2-}, NO_3^-, Na^+, Ca^{2+}, NH_4^+, Mg^{2+}, and K^+ were measured using ion chromatography (Thermo Scientific ICS-2100). For the cations, the column is Dionex CS-12A, and the eluent is 20 mM MSA. For the anions, the column is Dionex AS-14A, and the eluent is 23 mM NaOH. The injection volumes are 1,000 μL for anion and 500 μL for cation. Analytical precision of the ion concentration is 10%. The water isotope ratio in SE-Dome II ice core was not measured in this study.

For the ion concentrations and isotope measurements, the entire SIGMA-A ice core was cut into 894 samples with depth intervals 50–160 mm (average thickness of 67 mm) in a cold room (−22 ºC). The data is published in Kurosaki et al (2020).

2.4 Measurements with ice layers

For the SIGMA-A ice core, the ice layers selected for analyses are listed in Table 2-2. 10 thin ice layers at random depths (Table 2-2) plus the two thickest ice layers from 4.330–4.480 and 6.056–6.211 m (Table 2-2) were selected from the SIGMA-A ice core. For the SE-Dome II ice core, ice layers at 16.808–16.816 m and 100.403–100.418 m were selected (Table 2-3). With the following methods, the shape, the location and chemical forms of inclusions in the ice layers from the SIGMA-A ice core and the SE-Dome II ice core were examined. In addition, the depth distribution of inclusions in the two thick ice layers at 4.330–4.480 m and 6.056–6.211 m depths from the SIGMA-A ice core were investigated.

Table 2-2. The methods applied to ice layers from SIGMA-A ice core in different depths and years.

Depth (m)	Year	Method							
		Bulk ion concentration	Detailed ion concentration	Detailed stable water isotope	Micro-scope	Raman	Ice sublimation method (−22 °C)	Ice sublimation method (−50 °C)	SEM- EDS
	snow							○	○
2.780–2.805	2014	○			○	○		○	○
4.330–4.480	2012	○	○	○	○	○	○		○
6.056–6.211	2006	○	○	○	○	○	○		○
19.700–19.705	1982	○					○		○
20.581–20.596	1981	○			○	○		○	○
22.611–22.631	1977	○						○	○
22.975–22.987	1976	○					○		○
33.879–33.882	1957	○					○		○
33.979–33.990	1956	○					○		○
34.610–34.661	1955	○			○	○	○		○
44.608–44.618	1935	○					○		○
51.373–51.378	1921	○					○		○

Table 2-3. The methods applied to ice layers from SE-Dome II ice core in different depths and years.

Depth (m)	Year	Method							
		Bulk ion concentration	Detailed ion concentration	Detailed stable water isotope	Micro-scope	Raman	Ice sublimation method (−22 °C)	Ice sublimation method (−50 °C)	SEM- EDS
16.808–16.816	2012	○			○	○	○		○
100.403–100.418	1950	○					○		○

2.4.1 Microscope observations and Raman spectroscopy analyses of inclusions

In order to analyze the shape, location, and chemical compositions of inclusions in ice layers, the ice layers were selected from the SIGMA-A ice core and the SE-Dome II ice core. In the SIGMA-A ice core, the ice layers were selected from 2.780–2.805 m, 20.581–20.596 m, 34.610–34.661 m depth, as well as the two thick ice layers from 4.330–4.480 and 6.056–6.211 m (Table 2-4). In the SE-Dome II ice core, the ice layer from 16.808–16.816 m were selected (Table 2-5). Using microscopes (Olympus STU-UM and Nikon MM-400) in a cold room of −22 °C, micro inclusions in cuboid samples were observed. The objective lens for Olympus STU-UM is an Olympus ULWD Neo SPlan 50, with settings of numerical aperture (NA) 0.55, magnification 50× and 500×. For Nikon MM-400, the objective lens is a Nikon TU Plan ELWD, with settings of numerical aperture (NA) 0.60, magnification 50× and 500×. The samples were scanned while adjusting the z-axis by 5 mm to scan the depth. Any inclusion greater than 1 μm across were observed, noting its location, shape, and size.

Using micro-Raman spectroscopy (T64000, Horiba Jobin-Yvon) with a laser (Quantum Torus 532, Horiba), the chemical form of selected inclusions was determined. The method is that described by Ohno et al. (2005, 2006) and Sakurai et al. (2010a). A heating wire for temperature control was connected to a Dewar tank filled with liquid nitrogen and heated the inside of the tank to fill the chamber with nitrogen gas to keep the temperature at −30 °C. Laser light (532 nm wavelength, software NGS LabSpec ver.5.64.15) of power 140 mW was focused on an inclusion using a long-working-distance objective lens with 6 mm focal length (M Plan Apo 100×; Mitutoyo). A silicon wafer was used to calibrate the Raman spectra at 520 cm^{-1}. To identify chemical compositions in the inclusion, the obtained spectra were compared to reference data (Ohno et al., 2005, 2014, 2016; Sakurai et al., 2010b, 2011).

In addition, the reference data were obtained by Raman experiments with regents. Each H_2SO_4 (Wako, 97 %), HCl (Wako, 35-37 %), Na_2SO_4 (Kishida, 99 %), $(NH_4)_2SO_4$ (Kishida, 99.5 %) was mixed with ultrapure water to form 0.1 mol/L solution. Then, the solutions were mixture at the ratio listed in Table 2-6. The 10 μL solution was dropped and frozen on the slide glass put in the chamber at −30 °C. The Raman spectra was then measured on the frozen solution. Laser intensity and measurement time were the same as for the measurement of inclusions in ice layers described above. The Raman peaks, phases, and chemical compositions are summarized in Table 2-7.

Table 2-4. SIGMA-A sample sizes analyzed by Raman spectroscopy.

Depth (m)	Year	Size: x(thickness) ×y×z (mm)	Number of observed inclusions
2.780–2.805 m	2014	25×15×5	3
4.330–4.480 m	2012	150×15×5	128
6.056–6.211 m	2006	155×15×5	287
20.581–20.596 m	1981	15×10×5	46
34.610–34.661 m	1955	51×15×5	49

Table 2-5. SE-Dome II sample sizes analyzed by Raman spectroscopy.

Depth (m)	Year	Size: x(thickness) ×y×z (mm)	Number of observed inclusions
16.808–16.816 m	2012	8[1)]×10×5	30

1) The 8 mm part was chosen from the whole ice layer formed in 2012.

Table 2-6. Mixtures with reagents and their mixing ratios.

Regent	H_2SO_4：Na_2SO_4	HCl：Na_2SO_4	$(NH_4)_2SO_4$: H_2SO_4
Ratio	99:1 95:5 88:12 82:18 75:25	90:10 75:25 62:38 50:50	90:10 80:20 60:40 40:60 30:70 10:90

Table 2-7. The summary of Raman peaks, phases, and chemical compositions detected in this study.

Raman peak (cm^{-1})	Phase	Chemical compositions
982	Liquid	$(NH_4)_2SO_4$
984	Liquid	H_2SO_4
990	Solid	$Na_2SO_4 \cdot 10H_2O$
1008	Solid	$CaSO_4 \cdot 2H_2O$

2.4.2 Observation of nonvolatile inclusions by the sublimation–EDS method

To extract the nonvolatile inclusions in the ice layers, two ice sublimation methods were used. In the first method, nine cuboid samples from SIGMA-A ice core (Table 2-8) and two cuboid samples from SE-Dome II ice core (Table 2-9) were selected. Each sample has dimensions with x (the ice layer thickness), y (5 or 8 mm), and z (5 mm). Then each sample was decontaminated by shaving off its surfaces using a clean ceramic knife in a cold clean room (class 10000). After that, the sample was put on a clean and mirror-processed metal plate (stainless SUS304), and then place the plate on a polycarbonate membrane filter (diameter 47 mm, pore size 0.45 μm, Advantec 11040004) in a precleaned chamber (Suction Filter Holder with Receiver Flask, Sartorius AG) kept at −22 °C. The chamber was placed in a clean bench (Simple Type Clean Booth AI Type-C, class 1000), and clean air of 15.0 L min^{-1} was supplied to the chamber for 2–3 days by using a pump (NRK Unipump UP-2) to sublimate all volatile materials including ice. After the sublimation, the nonvolatile inclusions were deposited on the metal plate as residue, and the metal plate was kept at room temperature in a dry desiccator until SEM-EDS analyses. In the second method, four samples randomly collected from the surface snow as well as ice layers in the 2.780–2.805, 20.581–20.596, and 22.611–22.631 m depths from SIGMA-A ice core (Table 2-2) were pulverized. The nonvolatile inclusions were then extracted from each 1 g sample at −50 ºC by following the sublimation method described in Iizuka et al. (2009). Compared to the first method (−22 ºC), the main difference with the second method (−50 ºC) is the pulverizing of the samples, which is done to enable sublimation at low temperature given small sample quantities. With this method information about the residues original position (depth) in the ice was lost. Additionally, with this method, sublimation occurs on a Teflon membrane filter (pore size 0.45 μm) in a closed system, so the nonvolatile inclusions larger than 0.45 μm are collected without loss on the membrane filter.

Constituent elements, inclusion diameters, and areas of each nonvolatile residue were measured using two SEM-EDS system: a JSM-6360LV (Japan Electron Optics Laboratory) SEM and a JED2201 (JEOL) EDS system, and a Flex SEM 1000 II (HITACHI) SEM and a Xplore compact 30 (OXFORD) EDS system. The SEM-EDS system by JEOL was used for the SIGMA-A ice core, and that by HITACHI and OXFORD was used for the SE-Dome II ice core. For the both SEM-EDS systems, the accelerating voltage was 20 keV with a working distance of 20 mm and a collecting time of 30–60 s. The levels of Si, Al, S, Cl, Na, Mg, and Ca in the inclusions,

which were the major detected elements, were determined. In this analysis, O, C, and N were also detected but their levels were considered unreliable due to their light masses.

Inclusions containing Si are assumed to have silicate material, and almost all S and Cl in the nonvolatile inclusions are from soluble material of sulfate and chloride compounds (Iizuka et al., 2009, 2012b). The dry-air ventilation removes gas-phase acidic compounds such as HCl and HNO_3, and the remnant liquid acid droplets (H_2SO_4) are unstable under the measurement environment in a vacuum at +25 ˚C of the SEM chamber. The coefficient of variation (CV) of the atomicity ratio from the SEM-EDS is based on the average values and standard deviations of these 20 measurements, which gives a value of 0.40 (Iizuka et al., 2012a). The sublimation EDS method cannot be used to investigate the phase and location of inclusions in the ice matrix, though it can be used to investigate the diameter, surface shape, and elemental compositions.

Table 2-8. Sample sizes of ice layers from the SIGMA-A ice core before the −22 °C sublimation and SEM-EDS analysis.

Depth (m)	Year	Size: x(thickness) ×y×z (mm)
4.330–4.480 m	2012	150×8×5
6.056–6.211 m	2006	155×8×5
19.700–19.705 m	1982	5×5×5
22.975–22.987 m	1976	8×5×5
33.879–33.882 m	1957	3×5×5
33.979–33.990 m	1956	11×5×5
34.610–34.661 m	1955	51×8×5
44.608–44.618 m	1935	10×5×5
51.373–51.378 m	1921	5×5×5

Table 2-9. Same as Table 2-8 but of SE-Dome II ice core.

Depth (m)	Year	Size: x(thickness) ×y×z (mm)
16.808–16.816 m	2012	8[1)]×8×5
100.403–100.418 m	1950	15×8×5

1) The 8 mm part was chosen from the whole ice layer formed in 2012.

2.4.3 Ion concentration and water isotope ratio measurements

To investigate the depth distribution of ion concentration and water isotope ratio in the thick ice layers, the two thickest ice layers in the SIGMA-A ice core at 4.330–4.480 m and 6.056–6.211 m depth, which are 150 and 155 mm thick, were used. To measure the ion concentrations and the water isotope ratio of these ice layers, the ice layers from the core sections were cut in the cold room (−22 ºC). Using a clean ceramic knife in the cold clean room (class 10,000), the SIGMA-A samples were further divided into 15 samples 10 mm thick for the 150 mm ice layer and into 31 samples 5 mm thick for the 155 mm ice layer. Then, the samples were put into clean polyethylene bags. The bagged ice was then melted at room temperature in a clean room (+25 ºC). The ion concentrations of $CH_3SO_3^-$, Cl^-, SO_4^{2-}, NO_3^-, Na^+, Ca^{2+}, NH_4^+, Mg^{2+}, and K^+ were measured using ion chromatography (Thermo Scientific ICS-2100). For the cations, the column was Dionex CS-12A, and the eluent was 20 mM MSA. For the anions, the column was Dionex AS-17A column with 1–18 mM KOH gradient eluent. The injection volumes were 1,000 µL for anion and 500 µL for cation. The analytical precision of the ion concentration was 10%. Also, the stable isotope ratios of the samples were analyzed using a water isotope analyzer (Picarro, L2120-i) with an evaporating device (Picarro, A0212 vaporizer). The analytical precisions of $\delta^{18}O$ and δD were 0.08‰ and 0.8‰, respectively.

2.5 ERA5 reanalysis climate data

The ERA5 reanalysis datasets distributed by the European Centre for Medium-Range Weather Forecasts (Hersbach et al., 2020) was used to evaluate climate records in the SE-Dome II ice core (1950–present) (Fujita, personal communication). The hourly air temperature at the SE-Dome site (T_{PL}, °C) was extracted from the hourly pressure level temperatures (T_p and T_{p+1}, °C) at the closest geopotential heights (z_p and z_{p+1}, m a.s.l.) including the site elevation (z_{site}, m a.s.l.) as:

$$T_{PL} = \frac{T_{p+1} - T_p}{z_{p+1} - z_p}\left(z_{site} - z_p\right) + T_p$$

here p is a pressure level that satisfies $z_p \leq z_{site} < z_{p+1}$ (Sakai et al., 2015; Khalzan et al., 2022). With the hourly air temperature (T_{PL}, °C), a positive degree hour sum (PDH, °C h) in summer (June, July, and August) of each year was calculated as:

$$PDH = \sum \max[0, (T_{PL} - T_T)]$$

here T_T is a threshold temperature (°C) because the snow melting could occur even below 0 °C, and the ERA5 based temperature could have a certain bias. The threshold temperature was changed from –8 °C to 0 °C at an 0.5 °C interval, and then obtained correlation coefficient with the ice layer thickness during 1950 to 2020 for each threshold temperature (Sect. 4.3).

3 The characteristics of inclusions in ice layers of the SIGMA-A ice core

3.1 Ice core colorology and ice layers of the SIGMA-A ice core

Figure 3-1a shows that the high-resolution density increases steadily with increasing depth. Above 6.5 m, a few particularly large peaks exceed 830 kg m^{-3}. Such high values exist sporadically through the ice core and indicate thick ice layers corresponding with ice layers observed by visual observation. By visual observation, there are 243 ice layers thicker than 1 mm, with an average thickness of 13.8 mm (Figure 3-1b). These visual observations and density characteristics show that the frequency and the thickness of the ice layers increases at a shallower depth. The four thick ice layers more than 150 mm in thickness are detected in a range of 3.757–3.924 m (166 mm), 4.093–4.486 m (392 mm), 5.711–5.896 m (185 mm), and 6.000–6.211 m (211 mm) (Figure 3-1b).

The previous study (Kurosaki et al., 2020) was conducted to establish the age scale from 1903 to 2005 with annual counting of the water isotope ratio. The minimum peak at 6.44 m depth corresponds to the winter in 2005 (Kurosaki et al., 2020). In the region shallower than 6.44 m depth, the variations of water isotope ratio are disturbed by ice layers, resulting in unreliable peak counts. Therefore, in this section, the age at shallow depths was determined using the depth and thickness of ice layers.

Based on the absence of ice layers and distinct minimum peaks of water stable isotope ratio at 0–2 m, the 1.31 m peak corresponds to winter 2016 and the 0.24 m peak to winter 2017 (Figure 3-2a). Given that 2012 was the year when extreme surface melting occurred (Nghiem et al., 2012), the thickest ice layer, 4.093–4.486 m (392 mm), was probably formed in 2012. Furthermore, meteorological observations at the SIGMA-A site reported no accumulation in 2015 (Hirose et al., 2021). Therefore, the ice layers in the range of 2.12–2.80 m are assumed to have formed in 2014 and the ice layers in the range of 3.19 –3.39 m are assumed to have formed in 2013 (Figure 3-2b). During the 2005–2012 period, temperatures at Qaanaaq on the coast near the SIGMA-A site were higher in 2006, 2007, and 2011 than in previous years before 2005 (Wang et al., 2021). Therefore, the thicker ice layers at 5.711–5.896 m (185 mm) and 6.000–6.211 m (211 mm) were likely formed in 2007 and 2006, respectively (Figure 3-2b).

For the other ice layers, the year was attempted to determine by using the variation in high-resolution density (Figure 3-2b). The high-resolution density value increases at the depths of ice layers present and decreases at the depths of ice layers absent. Therefore, all ice layers in

the range of the maximum peak of the high-resolution density were assumed to have formed in the same year. Then, the ice layers in a range 5.000–6.300 m depth are divided to be formed in 2006, 2007, 2008 and 2009. It is considered that the 2012 ice layers are much thicker than other ice layers, suggesting they cover the firn layers corresponding to 2010–2012. The middle depth between ranges of ice layers was defined as the boundary of the years. Some Na^+ peaks with maxima detected in winter in these boundaries (Figure 3-2c). As a result, the age scale from 2017 to 2006 could be constructed (Figure 3-2). Using the obtained age scale and bulk density, the accumulation rate was calculated and the average annual accumulation rate from 1903 to 2017 was determined to be 0.36 m w.e. yr^{-1}.

The age profiles of the number and thickness of ice layers were examined using the obtained age scale from 1903 to 2017 (Figure 3-1b). As mentioned above, 243 ice layers with an average thickness of 13.8 mm were detected since 1903. Since 1995, 96 ice layers with an average thickness of 23 mm were detected, confirming that the number and thickness of ice layers have increased with Arctic warming. The melt feature percentage (MFP%) profile (Figure 3-1b), which is the annual ice layer thickness in the annual layer thickness, also shows the same trends. Compared to the Arctic temperature, the MFP (%) is low during the cooler periods of 1960s–1970s and high during the warmer periods of 1940–1950s and recent decades. This suggests a synchronous oscillation between Arctic temperature and MFP reconstructed from the SIGMA-A ice core.

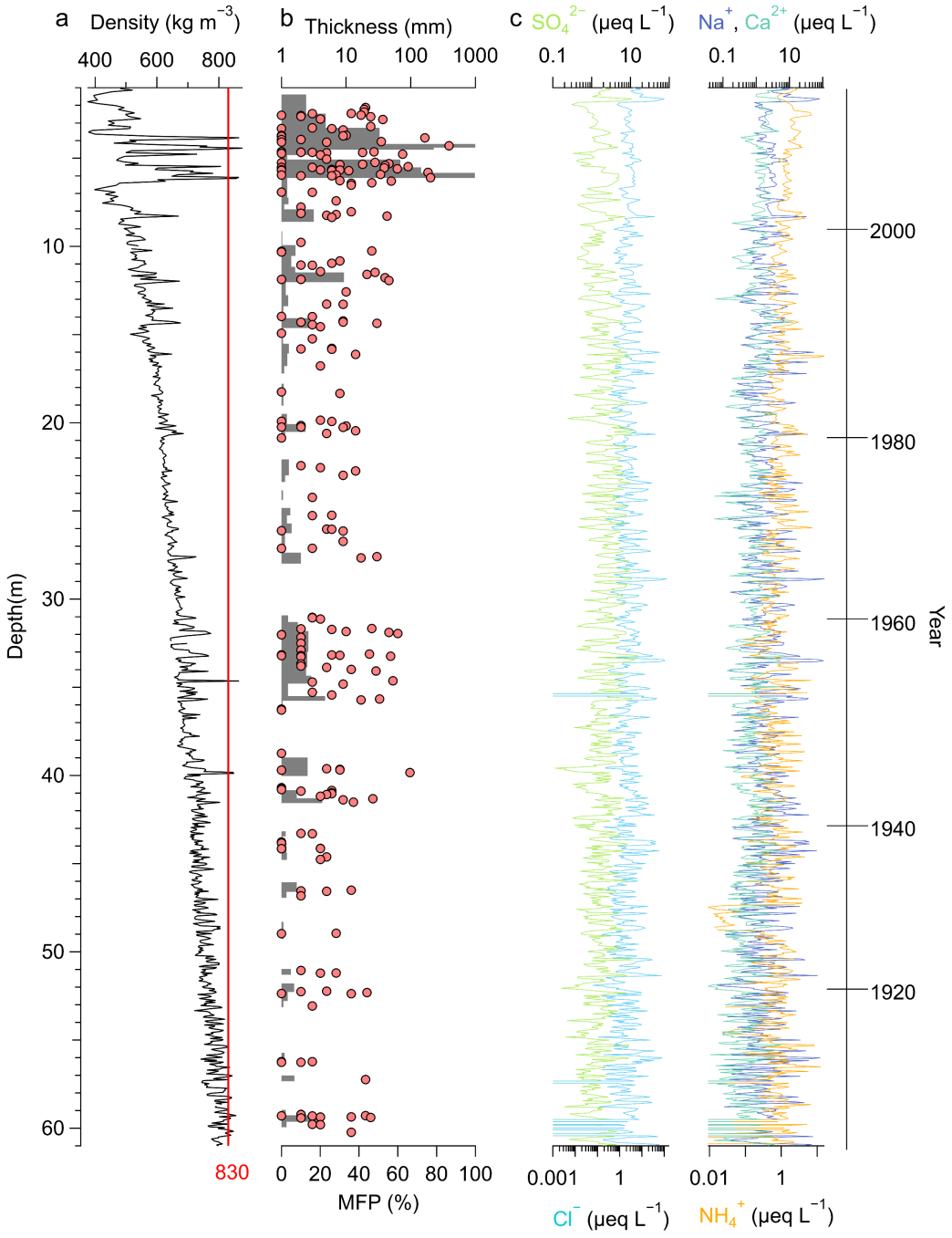

Figure 3-1 Depth and age profiles of physical properties and major ions in the SIGMA-A ice core. (a) high resolution density, (b) ice layer thickness (mm) and melt feature percentage per year (%), and (c) ion concentrations (SO_4^{2-}, Cl^-, Na^+, Ca^{2+}, NH_4^+).

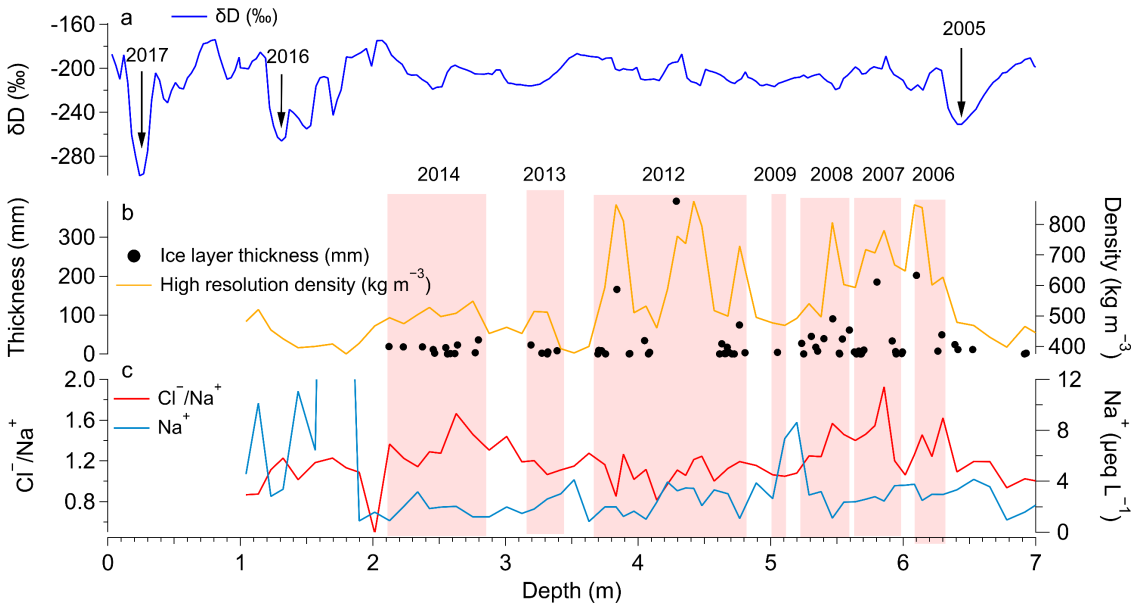

Figure 3-2 Depth profiles of (a) δD (‰), (b) high-resolution density (kg m^{-3}) and ice layer thickness (mm), (c) Na^+ (μeq L^{-1}) concentration and Cl^-/Na^+.

3.2 Ion concentration of the SIGMA-A ice core

Ion concentration profiles in Fig. 3-1c are averaged over 10-year periods in Table 3-1. In the Table, SO_4^{2-} has high concentrations during 1950–1980s (average of 3.35 μeq L^{-1}), a period when the emission of anthropogenic SO_4^{2-} was at a maximum (Fischer et al., 1998). In contrast, the core-average concentrations of NH_4^+ and Ca^{2+} are much less, at 1.08 μeq L^{-1} and 1.05 μeq L^{-1}. Their values increase after 2000, a trend also observed in ice cores obtained from southeastern and northwestern Greenland (e.g., Iizuka et al., 2018; Nagatsuka et al., 2021). The highest core-averaged concentrations come from Na^+ and Cl^-, at 4.51 μeq L^{-1} and 5.29 μeq L^{-1}, generally over twice the averages of the other four ion species, suggesting a high impurity contribution from sea salt (Curtis et al., 2018), which is likely due to the site being in a coastal region. These Na^+ and Cl^- concentrations vary by roughly a factor of two between decades, though the decadal mean values hardly change over the past 100 years.

Table 3-1 The average of major ion concentrations (μeq L^{-1}) in the entire SIGMA-A ice core.

	Cl^-	SO_4^{2-}	Na^+	NH_4^+	Mg^{2+}	Ca^{2+}	Mg^{2+}/Na^+
2016–2010	6.49	1.89	5.65	2.49	1.17	2.02	0.09
2009–2000	4.23	2.19	3.48	1.53	0.74	1.42	0.13
1999–1990	3.56	1.79	2.86	1.13	0.72	1.44	0.14
1989–1980	5.28	3.18	4.42	1.38	1.12	1.17	0.14
1979–1970	3.86	3.23	3.08	1.18	0.81	0.85	0.14
1969–1960	6.74	3.63	5.26	0.75	1.31	1.23	0.17
1959–1950	7.79	3.37	6.75	0.76	1.65	1.21	0.17
1949–1940	4.10	1.97	3.70	0.83	0.92	0.95	0.14
1939–1930	5.63	2.16	5.41	0.89	1.42	0.94	0.18
1929–1920	4.13	1.93	3.63	0.76	0.85	0.59	0.17
1919–1910	5.63	1.85	4.99	1.15	1.19	0.74	0.21
1909–1903	6.20	1.41	4.85	1.25	1.19	0.76	0.18
Core average	5.29	2.42	4.51	1.08	1.10	1.05	0.16

Snowmelt and refreezing processes affect ion concentrations (e.g., Iizuka et al., 2002), so it is expected to differ between firn and ice layer. The average concentrations (μeq L^{-1}) of Na^+ and Cl^- are 5.25 and 5.65 in the upper firn, which are just above the ice layers, 4.07 and 4.97 in the ice layers, and 3.99 and 4.90 in the lower firn, which are just below the ice layers. In Figure 3-3, the values in a given depth region are compared to that in the region above; in particular, the ratios of the ice layers to the upper firn values, and of the lower firn to the ice layers values. For Na^+ and Cl^- ratios for the ice layers to the upper firn (orange), there are a relatively large number of values for ratios over 1.0, compared to the same ratios for the lower firn to the ice layers. This shift suggests ion enrichment from the upper firn to the ice layers, presumably due to the transportation of ions by meltwater percolation. Figure 3-3c also shows the general trend in Mg^{2+}/Na^+ for the upper firn, ice layers, and lower firn. If Mg^{2+}/Na^+ for the precipitation is equal to the sea salt ratio (0.11), then a high ratio in the ice layers can only be attributed to the inflow of meltwater (e.g., Iizuka et al., 2002). From Figure 3-3c, the Mg^{2+}/Na^+ in the upper firn tends to be less than 0.11, whereas that in the ice layers tends to exceed 0.11. These results suggest that the chemical compositions tend to concentrate in the ice layers from the upper firn.

For the Na^+ and Cl^- ratios of the lower firn to that in the ice layers, the values seem to show two peaks in Figure 3-3a and 3-3b, one of which is less than 1.0 and the other is around 1.5. The peak below 1.0 suggests that the ice layers can collect ions that would otherwise flush to the lower firn; on the other hand, the peak near 1.5 suggests further ion migration occurred to the lower firn from the meltwater, which will become ice layers.

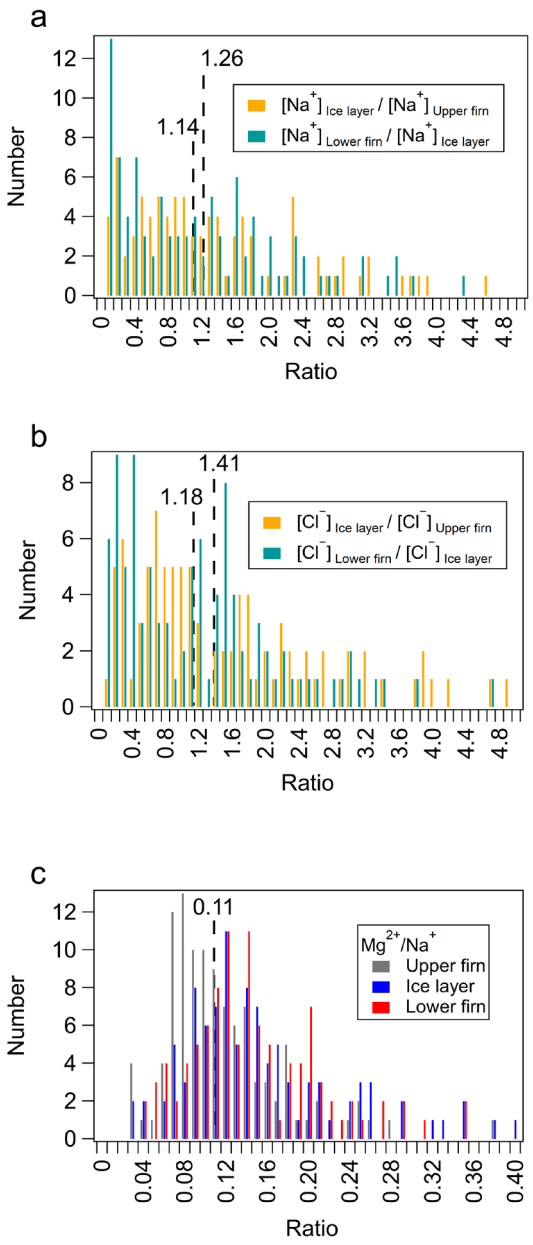

Figure 3-3 Ratios of ion concentrations in the ice layers and firn. (a) For Na^+ ratios. Not shown are the ratios exceeding 5.0, which comprise 16% of the cases for $[Na^+]_{\text{Ice layer / Upper firn}}$ and 10% of the cases for $[Na^+]_{\text{Lower firn / Ice layer}}$. For $[Na^+]_{\text{Ice layer / Upper firn}}$ and $[Na^+]_{\text{Lower firn / Ice layer}}$, the median and standard deviation are 1.26 ± 11.86 and 1.14 ± 13.47. (b) For Cl^- ratios. Not shown are the ratios exceeding 5.0, which comprise 13% of the cases for $[Cl^-]_{\text{Ice layer / Upper firn}}$ and 10% of the cases for $[Cl^-]_{\text{Lower firn / Ice layer}}$. For $[Cl^-]_{\text{Ice layer / Upper firn}}$ and $[Cl^-]_{\text{Lower firn / Ice layer}}$, the median and standard deviation are 1.41 ± 7.85 and 1.18 ± 5.90. (c) Mg^{2+}/Na^+ ratios. Not shown are Mg^{2+}/Na^+ ratios over 0.4. These comprise 0.9, 7.3, and 4.6% of the cases for the upper firn, the ice layer, and the lower firn, respectively.

3.3 Shape and chemical components of inclusions in the ice layers of the SIGMA-A ice core

3.3.1 Microscope observation and Raman results

Five ice layers dated 1955, 1981, 2006, 2012, and 2014 were chosen to examine the inclusions using microscope observations and Raman analyses (Table 2-2). All observed fields in these ice layers described in the Table 2-4 were examined and 513 inclusions were found. Of the 513, the most common shapes are particle-like (n=253) and rod-like (n=230), with the remaining 30 classified as columnar-like. Concerning this classification, if the inclusion is angular, it is classified as columnar. If not, it is then checked if the non-columnar inclusion has an aspect ratio (major-to-minor axes) exceeding 2:1, and if so, the inclusion is classified as rod-like. What remained were particle-like, an example of which is shown in Figure 3-4a. The particle-like inclusions occurred both in ice grains and on grain boundaries. The rod-like inclusions were found in grain boundaries and triple junctions (Figure 3-4b) and had diameters of about 10–100 μm. This type generally had the longest lengths of all inclusions. Almost all rod-like inclusions were detected in thick ice layers such as those from 2012 and 2006 (Figure 3-1b and Figure 3-2b). The columnar-like inclusions were found in ice grains (Figure 3-4c). Some of the particle- and columnar-like inclusions were greater than 30 μm in diameter.

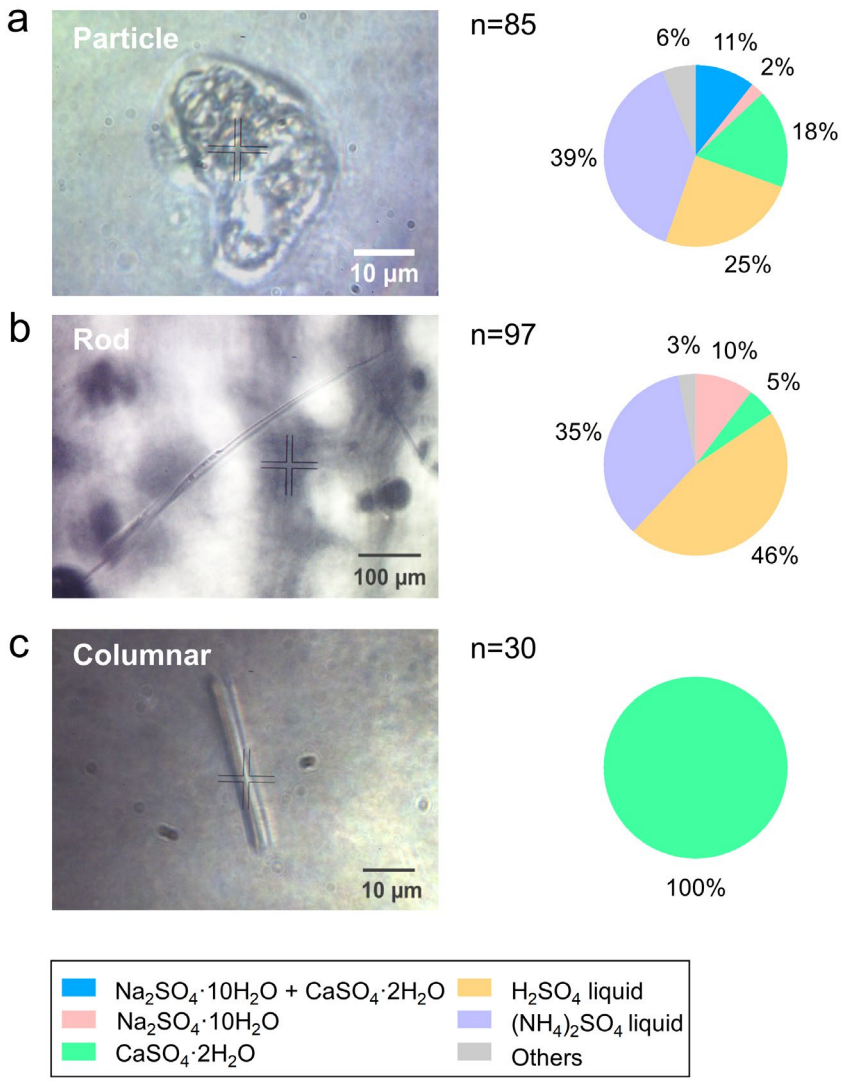

Figure 3-4 Microscope images and Raman spectroscopy analyses of the three types of inclusions. (a) Particle-like inclusion in an ice grain from the 2014 ice layer, with peaks at 990 and 1008 cm^{-1}. At right is the distribution of chemical compositions of 85 particle-like inclusions from Raman analyses from all ice layers. Colours, defined at bottom, are based on peaks at 982, 984, 990, 1008 cm^{-1}. 'Others' means peaks found at other wavenumbers. (b) Rod-like inclusion in a grain boundary from the 2006 ice layer, with a peak of 984 cm^{-1}. Right side is the same as that in (a) except for 97 rod-like inclusions. (c) Columnar-like inclusion in a grain interior from the 2006 ice layer, with a peak of 1008 cm^{-1}. Right side is the same as that in (a) except for 30 columnar-like inclusions.

The chemical forms of the inclusions are measured by Raman spectroscopy. In the spectra, peaks at 982, 984, 990, and 1008 cm^{-1} were investigated. The 982 and 984 cm^{-1} peaks have a broad half-width, suggesting liquid inclusions. In contrast, the 990 and 1008 cm^{-1} peaks are sharp, suggesting solid inclusions. Following Ohno et al. (2005), it is assumed the 990 cm^{-1} peak is $Na_2SO_4 \cdot 10H_2O$, and the 1008 cm^{-1} peak is $CaSO_4 \cdot 2H_2O$. The broad peaks at 984 cm^{-1} indicate SO_4^{2-} in a liquid phase (Sakurai et al., 2017). However, no prior reference was found for the broad 982 cm^{-1} peak, so a few tests were ran that identified the peak as SO_4^{2-} and NH_4^+ in a liquid phase.

To identify the Raman peak at 982 cm^{-1}, reference spectra were measured for some chemical mixtures at −30 °C. Figure 3-5 shows Raman spectra of frozen mixtures of H_2SO_4–Na_2SO_4, HCl–Na_2SO_4, and $(NH_4)_2SO_4$–H_2SO_4. In mixtures of H_2SO_4 –Na_2SO_4 (Figure 3-5a), the Raman spectra has a peak at 984 cm^{-1} when the molar ratio of H_2SO_4 : Na_2SO_4 exceeds 88 : 12, but has a peak at 990 cm^{-1} when this molar ratio is below 82 : 18. So, H_2SO_4 produces the 984 cm^{-1} peak even when some Na_2SO_4 is present. Similarly, in Figure 3-5b the Raman peak at 984 cm^{-1} indicates liquid when the molar ratio of HCl : Na_2SO_4 exceeds 62 : 38, whereas the peak at 990 cm^{-1} indicates solid when the molar ratio of HCl : Na_2SO_4 lies below 50 : 50. Thus, neither of these mixtures of acid and Na_2SO_4 produce a peak at 982 cm^{-1}. Finally, for mixtures of $(NH_4)_2SO_4$ and H_2SO_4, solid $(NH_4)_2SO_4$ has a Raman peak at 975 cm^{-1} (Sakurai et al., 2010b). This peak was found for the case of a 90:10 mixture in Figure 3-5c. With increasing concentration of H_2SO_4, the peak broadens to include the three peaks of 975, 982, and 984 cm^{-1}. Then, when the molar ratio of $(NH_4)_2SO_4$: H_2SO_4 is lower than 30:70, only the 984 cm^{-1} peak is clear. However, when the molar ratio of $(NH_4)_2SO_4$: H_2SO_4 is between 90:10 and 30:70, the 982 cm^{-1} peak is detected. Given that the major cations in the ice layers of the SIGMA-A ice core are Na^+ (4.07 μeq L^{-1}) and NH_4^+ (1.39 μeq L^{-1}) compared to Mg^{2+} (1.18 μeq L^{-1}) and Ca^{2+} (1.28 μeq L^{-1}), it will be assumed that the liquid 982 cm^{-1} peak indicates SO_4^{2-} and NH_4^+. The number of times each peak (982, 984, 990, and 1008 cm^{-1}) was detected in each ice layer is shown in Figure 3-6a.

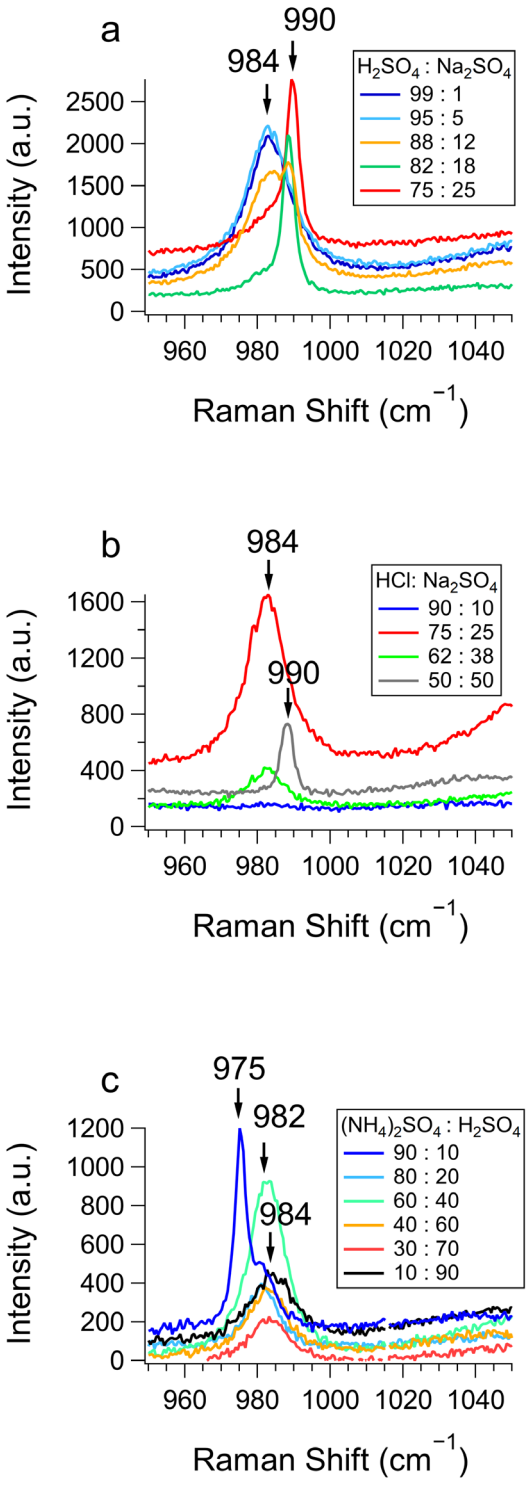

Figure 3-5 Reference spectra for frozen solution mixtures at 1 atm and −30°C. (a) Mixtures of H_2SO_4 and Na_2SO_4. (b) Mixtures of HCl and Na_2SO_4. (c) Mixtures of $(NH_4)_2SO_4$ and H_2SO_4. The legend of (a–c) shows the molar ratio of each mixture.

Among 513 inclusions, 209 showed Raman peaks, whereas 304 inclusions did not. Among 209 inclusions, 12 inclusions show the double peaks. Of the 221 peaks (Table 3-2), 96% (n = 213) show chemical compound at liquid $(NH_4)_2SO_4$, liquid H_2SO_4, solid $Na_2SO_4 \cdot 10H_2O$, and solid $CaSO_4 \cdot 2H_2O$. The breakdown of the 213 peaks is such that 31% have the liquid $(NH_4)_2SO_4$, 31% have the liquid H_2SO_4, 10% have the solid $Na_2SO_4 \cdot 10H_2O$, and 28% have the solid $CaSO_4 \cdot 2H_2O$ (Table 3-2).

The peaks depend on the inclusions shape -type as shown by the pie charts on right side of Figure 3-4. Among the particle-like type, individual inclusions had one or two compounds, distributed between all four compounds (Figure 3-4a, right). Nearly all of the rod-like inclusions are either liquid $(NH_4)_2SO_4$ or liquid H_2SO_4 (35% and 46% of cases in Figure 3-4b). On the other hand, all columnar-like inclusions are solid $CaSO_4 \cdot 2H_2O$ (gypsum) (Figure 3-4c). There are many inclusions with no Raman peaks, with 56% of them being the particle-like inclusions and the remaining 44% being the rod-like inclusions. The chemical composition of these inclusions is discussed next.

Table 3-2 The number of 982, 984, 990, 1008 (cm^{-1}) and other peaks detected from three types of inclusions. The peaks at 982, 984, 990, and 1008 (cm^{-1}) indicate liquid $(NH_4)_2SO_4$, liquid H_2SO_4, solid $Na_2SO_4 \cdot 10H_2O$, and solid $CaSO_4 \cdot 2H_2O$.

	982 (cm^{-1})	984 (cm^{-1})	990 (cm^{-1})	1008 (cm^{-1})	Other peaks	Total peaks	No peaks	Total measurements
Particle	33	21	11	24	5	94	170	264
Rod	34	45	10	5	3	97	134	231
Columnar	0	0	0	30	0	30	0	30
Total	67	66	21	59	8	221	304	525

3.3.2 Shape and elemental components of nonvolatile inclusions in ice layers

The microscope observation has the advantage of determining locations of inclusions in an ice layer (e.g., within ice grains, along grain boundaries, in triple junctions). However, the method cannot detect all the inclusions because bubbles in an ice layer make it difficult to locate every inclusion. In contrast, the sublimation–EDS method can measure the shapes and sizes of almost all inclusions formed in the ice layers.

The SEM measurements revealed 1230 nonvolatile inclusions in the three shape types through the 12 ice layers. Of these types, the particle-like inclusions occur in almost all ice layers and account for 94.4% (n = 1161) of the total inclusions (light and dark blue bars in Figure 3-6b). Almost all rod-like inclusions occur in the two thickest ice layers, and they account for 3.1% (n = 38) of the total inclusions (pink and red bars in Figure 3-6b). The columnar-like inclusions exist in both thin and thick ice layers, and account for only 2.5% (n = 31) of the total inclusions (light and dark green bars in Figure 3-6b).

The cross-sectional area S (μm^2) of an inclusion was measured by tracing the inclusions perimeter on a photomicrograph. For the particle-like inclusions, the radius r (μm) is then calculated as

$$r = \sqrt{\frac{S}{\pi}} \tag{1}$$

Then the grain diameter is defined as twice the radius. For rod-like and columnar-like inclusions, the grain length is defined as the major axis length. The grain diameter and length are referred as $D_{inclusion}$ (μm).

The two methods (microscope and SEM) similarly find the particle type to be relatively common and the rod type to be more common in thick ice layers. Moreover, both methods show columnar to be the least common type. The proportion of particle-like is much larger in the SEM (94.4 %) method than in the microscope method (50 %). The difference is likely due to the particle-like inclusions being generally smaller (see below) and more easily detected with the SEM method. In addition, the rod-like inclusions with small $D_{inclusion}$ (e.g., Figure 3-10, see '(X)') are difficult to distinguish from particle-like inclusions in the SEM method, so some rods may have been counted as particle type.

Almost all nonvolatile inclusions in the surface snow sample at the site are particle-like (Figure 3-6b), with an average grain diameter of 9.0 ± 8.7 μm. Also, nearly all inclusions in the surface snow are smaller than 30 μm in diameter, with 66% being smaller than 10 μm. These particle types and sizes are consistent with nonvolatile inclusions in dry snow and ice cores in Antarctica and Greenland analyzed previously with the sublimation method (Iizuka et al., 2012a, 2012b, 2013; Oyabu et al., 2014, 2015, 2020). Given that aerosols are generally smaller than 30 μm in diameter (e.g., Whitby 1978), it is concluded that the inclusions greater than 30 μm in diameter formed during the meltwater refreezing process. So, the inclusions are divided further into two size categories: smaller and larger than 30 μm in diameter. For particle-like inclusions, 22% are greater than 30 μm in diameter (dark blue bar in Figure 3-6b). For rod-like inclusions, this percentage is 87% (red bar in Figure 3-6b), whereas for columnar-like inclusions, the percentage is 61% (dark green bar in Fig. 3-6b). Thus, most rod-like and columnar-like inclusions are over 30 μm in diameter, and therefore likely formed by refreezing.

The elemental analyses of the nonvolatile inclusions in the surface snow sample and 12 ice-layer samples are shown in Figure. 3-6 c, d, e, and f. Mg is not discussed because its abundance is very small (5%). Additionally, Al is not discussed because it is mainly in dust (insoluble terrestrial materials), which has Si as the main component. As a result, the content of the inclusions is classified into 12 categories based on their constituent elements of Na, Ca, S, and Cl, which are associated with Na^+, Ca^{2+}, SO_4^{2-}, and Cl^- species. For example, inclusions containing all of Na, Ca, S, and Cl are classified as 'Na∩Ca∩S∩Cl'. Those with Na and S but without Ca nor Cl are classified as 'Na∩S'. Those with only S or only Cl are classified as 'only S or Cl'. Finally, 'Others' have neither S nor Cl. (Others mainly contain Si, suggesting silicate minerals.) In the surface snow sample, 36% of the inclusions are classified as 'Na∩S', and nearly all of the remaining are 'Others' (Figure 3-6d). Compared to the surface snow, inclusions in the ice layers contain much more 'Na∩Ca∩S∩Cl' (dark blue; 11%), 'Na∩S∩Cl' (dark red; 11%), and 'Na∩Cl' (dark green; 10%), and much less 'Na∩S' (light pink; 5%) (Figure 3-6e). These differences are pronounced in the larger inclusions (Figure 3-6f). So, the combination of 'Na∩Cl' with or without S and Ca is common in the inclusions, particularly those formed by refreezing.

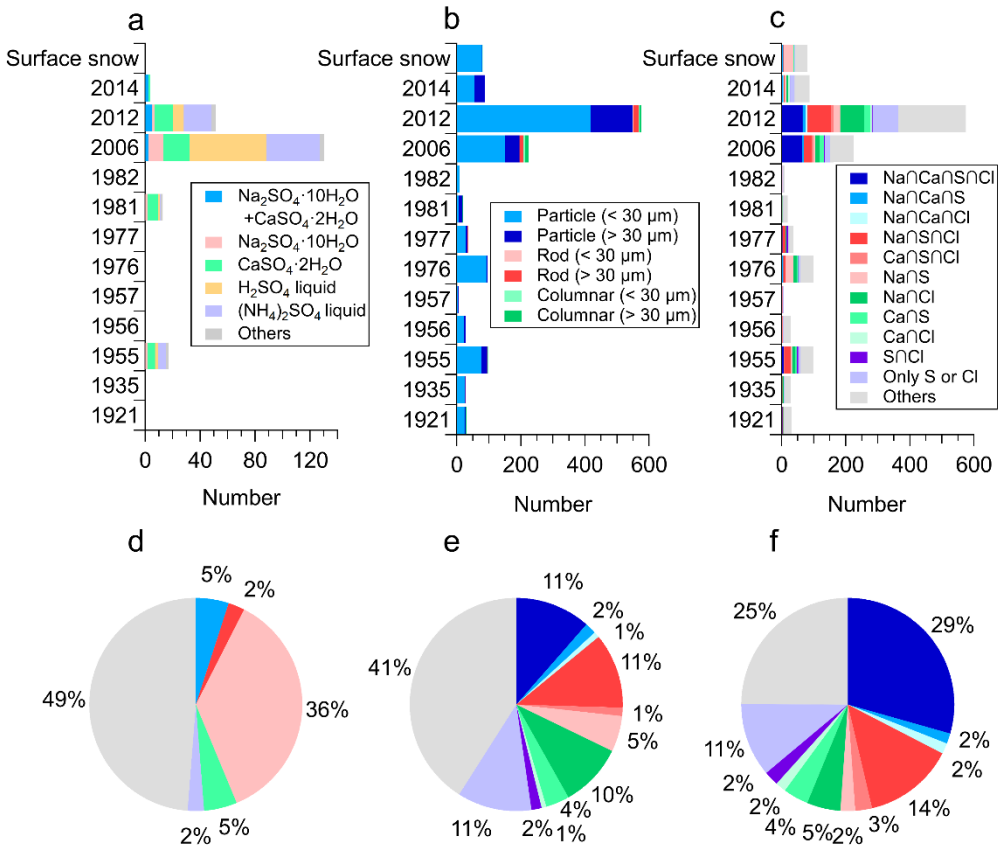

Figure 3-6 Depth profiles of composition and inclusion type, as well as the elemental compositions in the nonvolatile inclusions (a-c) and elemental compositions in the surface snow and ice layers (d-f). Analyses cover the surface snow and selected ice layers (Raman: 5 layers; SEM & EDS: 12 layers). (a) The number of times the chemical composition is detected by Raman analyses. (b) The number of each type of nonvolatile inclusion detected by SEM. (c) The number of times the element combinations are detected by EDS analyses in nonvolatile inclusions. (d) From 80 nonvolatile inclusions of the surface snow sample. The Colour code is the same as (c). (e) From 1230 nonvolatile inclusions of the 12 ice layers. (f) Same as (e) except restricted to 313 nonvolatile inclusions larger than 30 μm in diameter.

The most common signal in the particle type is 'Others' (grey; 42% in Figure 3-7a). Most of the 'Others' inclusions contain Si without Na, Ca, S, and Cl, suggesting that the particle-like inclusions mainly consist of mineral dust. The 'only S' inclusions may be NH_4^+ and SO_4^{2-} as liquid brine because Raman measurements showed the liquid 982 cm^{-1} peak, not the solid 975 cm^{-1} peak. In this case, liquid brine may exist at the ice temperature of −18.9 °C due to the eutectic temperature of $(NH_4)_2SO_4$ being −19.0 °C, or due to an ion balance of $SO_4^{2-} >> NH_4^+$ (Figure 3-5c).

In contrast, the 'Na∩Cl' with or without S and Ca inclusions are considered to be salt mixtures of NaCl, Na_2SO_4, and $CaSO_4$. The Na_2SO_4 and $CaSO_4$, having eutectic temperatures of −1.3 and −0.05 °C, are likely to exist as solid salts, whereas the NaCl, having a eutectic temperature of −21.3 °C, can exist as a liquid brine of Na^+ and Cl^- at −18.9 °C. Thus, by combining the Raman and EDS analyses, it is argued that the particle-like inclusions contain various solid salts of $Na_2SO_4 \cdot 10H_2O$ and $CaSO_4 \cdot 2H_2O$, as well as brines of Na^+, Cl^-, NH_4^+, and SO_4^{2-}.

The primary category for rod-like inclusions is 'Na∩Ca∩S∩Cl' (dark blue; 45% in Figure 3-7b). On the other hand, the Raman measurements show that the rod-like inclusions mostly have broad peaks of 982 and 984 cm^{-1} (35% and 46% in Figure 3-4b), as well as a high fraction of non-peak-detected inclusions. The broad 982 and 984 cm^{-1} peaks suggested that inclusions have NH_4^+ and SO_4^{2-} (Figure 3-5c), whereas the high fraction of non-peak-detected inclusions suggests an ionic compound of Na^+ and Cl^- which are Raman inactive. Sakurai (2010c) showed that mixtures of Na_2SO_4 and HCl have an extremely low eutectic temperature of −42.7 ºC (Na_2SO_4: 4.3 wt%, HCl: 2.1 wt%), which is colder than that of the Raman measurements (−30 ºC). Thus, a possible chemical form of the rod-like inclusions is a brine of SO_4^{2-}, Cl^-, Na^+, and NH_4^+.

For the columnar-like inclusions, the main elemental component is 'Ca∩S' (green; 55% in Figure 3-7c). Thus, the columnar-like inclusions probably consist of $CaSO_4$. Also, their shape is consistent with the crystal structure of gypsum ($CaSO_4 \cdot 2H_2O$), which is the prismatic class of the monoclinic system. These results suggest that the columnar-like inclusions contain impurities with the components of $CaSO_4$, which is consistent with the results from Raman analyses that indicated that the columnar-like inclusions contain solid gypsum salts ($CaSO_4 \cdot 2H_2O$).

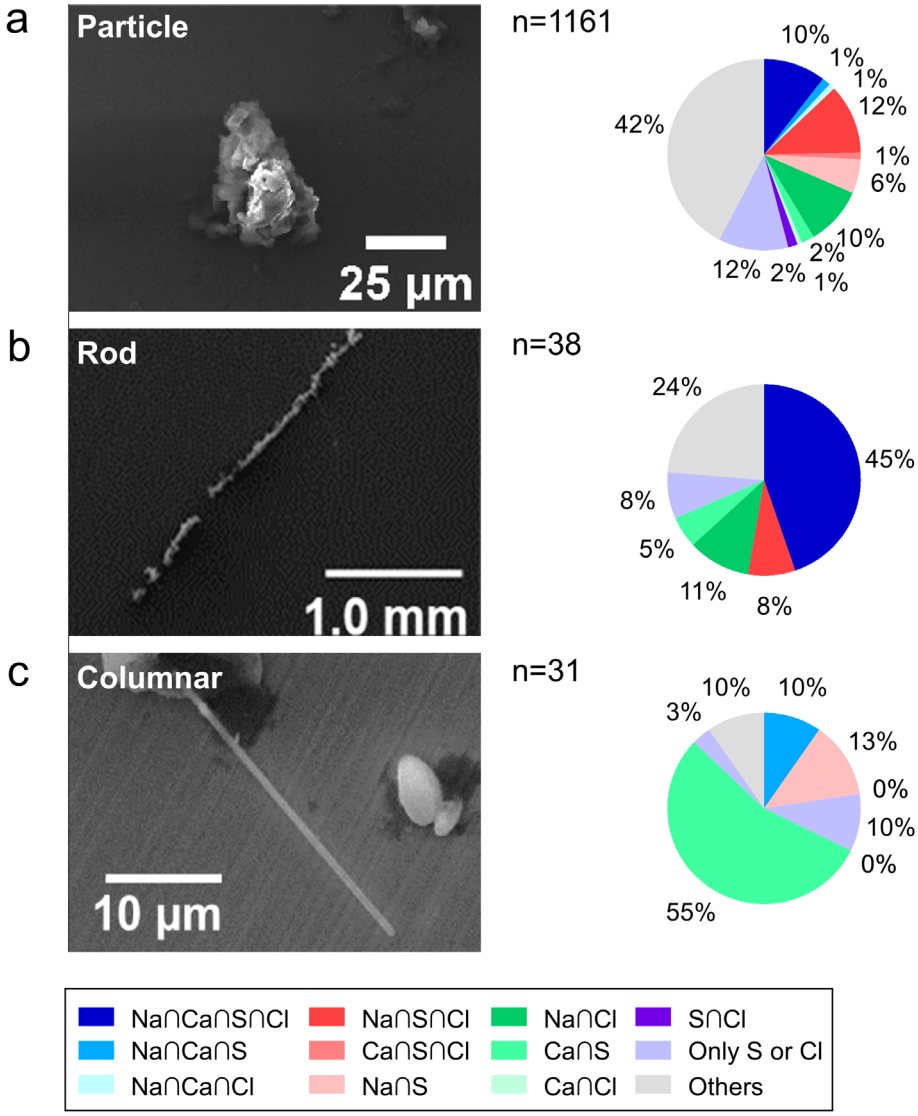

Figure 3-7 Microphotographs and elemental compositions by SEM-EDS analyses. (a) Particle-like inclusion from the 2012 ice layer and composition of 1161 particle-like inclusions from EDS analyses. (b) Rod-like inclusion from the 2012 ice layer and composition of 38 rod-like inclusions. (c) Columnar-like inclusion from the 2006 ice layer and composition of 31 columnar-like inclusions.

3.4 Chemical form and shape of inclusions in thick ice layers formed in 2012 and 2006 of the SIGMA-A ice core

The two thickest ice layers of 2012 and 2006 have many large rod-like inclusions (brine of SO_4^{2-}, Cl^-, Na^+, and NH_4^+). In this section, the chemical forms, shapes, and distributions of inclusions are examined in the thick ice layers.

3.4.1 The distribution of inclusions in the two thick ice layers

When water freezes, the heavier water stable isotopes fractionate toward the ice and the lighter water stable isotopes fractionate toward the water. As this phenomenon is repeated each time freezing proceeds, the water stable isotope ratios ($\delta^{18}O$, δD) are smaller in the last part to freeze (e.g., O'Neil, 1968). The refreezing processes of the thick ice layers formed in 2012 and 2006 are considered. The 2012 and 2006 ice layers are assumed to have been formed when the aquifer froze. Figure 3-8 shows ion concentrations and stable isotope ratios in the ice layer formed in 2012 with 10 mm resolution. In (a), the values of $\delta^{18}O$ and δD vary by 2.1 and 17‰, respectively. According to previous studies (e.g., O'Neil, 1968), these values are consistent with meltwater refreezing. $\delta^{18}O$ and δD have a correlation (Craig, 1961), and Dansgaard (1964) defined the deuterium excess (d-excess) as the following:

$$d - excess = \delta D - 8\,\delta^{18}O \qquad (2)$$

Lacelle (2011) suggests that the last ice to freeze is likely to have a higher d-excess value, such as that at depths around 4.370–4.390 m and 4.430–4.450 m, which is marked in light yellow in the depth profiles. Hence, the 2012 ice layer is possibly formed by at least three refreezing cycles.

Similar analyses for the 2006 ice layer are shown in Figure 3-9. (Inclusions above 6.071 m depth and below 6.191 m depth are not analyzed here due to the lack of water isotope data in those regions.) In (a), the values of $\delta^{18}O$ and δD fluctuate by 1.2 and 6.9‰, respectively. The slope of the liner regression between $\delta^{18}O$ and δD is 5.6, suggesting that the ice was formed by the refreezing of meltwater (e.g., Jouzel and Souchez, 1982; Souchez and Jouzel, 1984; Souchez and de Groote, 1985). It is considered the 6.101–6.126 m depths as the last region to freeze, due to the low $\delta^{18}O$ and high d-excess there, which are marked in light yellow in Figure 3-9. Hence, at least two refreezing cycles formed the 2006 ice layer.

Ion concentrations of all species are relatively high at the depths where refreezing was completed (Figures. 3-8a, 3-9a). For the 2012 ice layer (around 4.370–4.390 and 4.430–4.450 m

depths), each ion concentration is 1.1–1.8 times higher than that of other depths (Table 3-3). For the 2006 ice layer, each ion concentration except NH_4^+ (μeq L^{-1}) in the last region of refreezing (around 6.101– 6.126 m) is also 1.1–1.4 higher than other depths (Table 3-3). As ice rejects impurities upon freezing (e.g., Halde, 1980; Takenaka et al., 1996), ionic materials in the thick ice layers should be concentrated in the last ice to freeze.

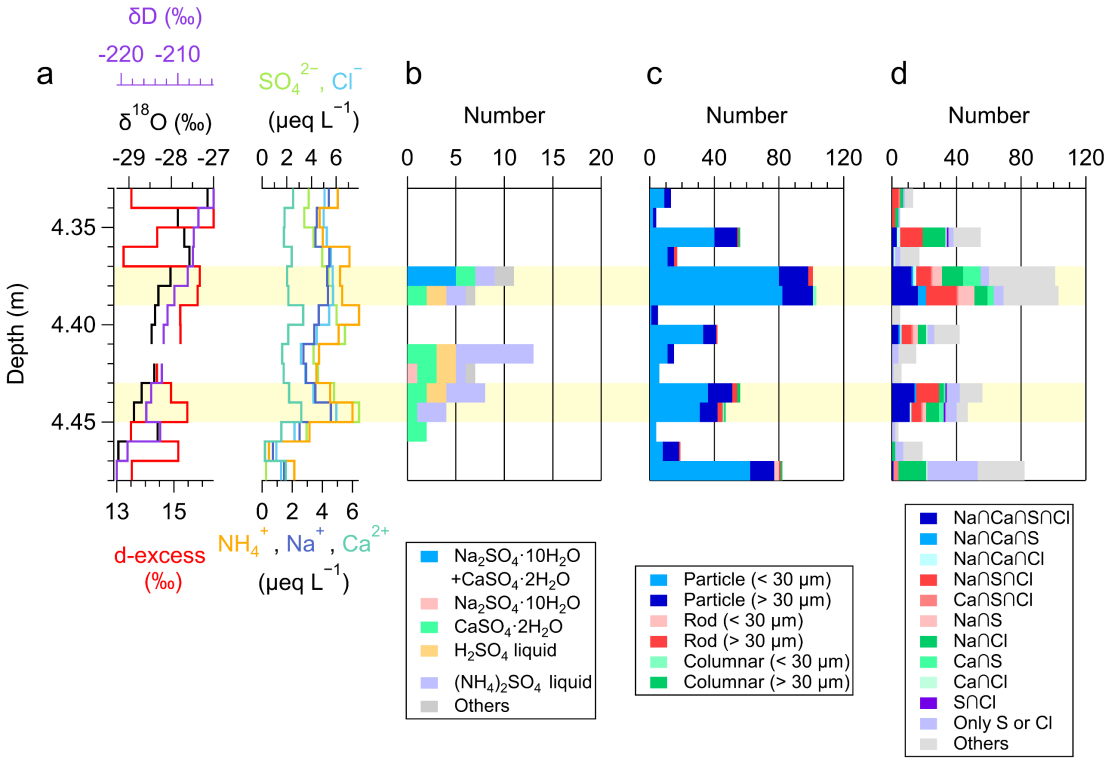

Figure 3-8 Depth profiles of the thick ice layer formed in 2012. (a) $\delta^{18}O$, δD, d-excess, and major ion species (SO_4^{2-}, Cl^-, NH_4^+, Na^+, Ca^{2+}). (b) The number of times the chemical compositions are detected by Raman analyses. (c) The number of inclusions of various types. (d) The number of times elements are detected by SEM analyses. Light yellow bands are levels that likely froze last.

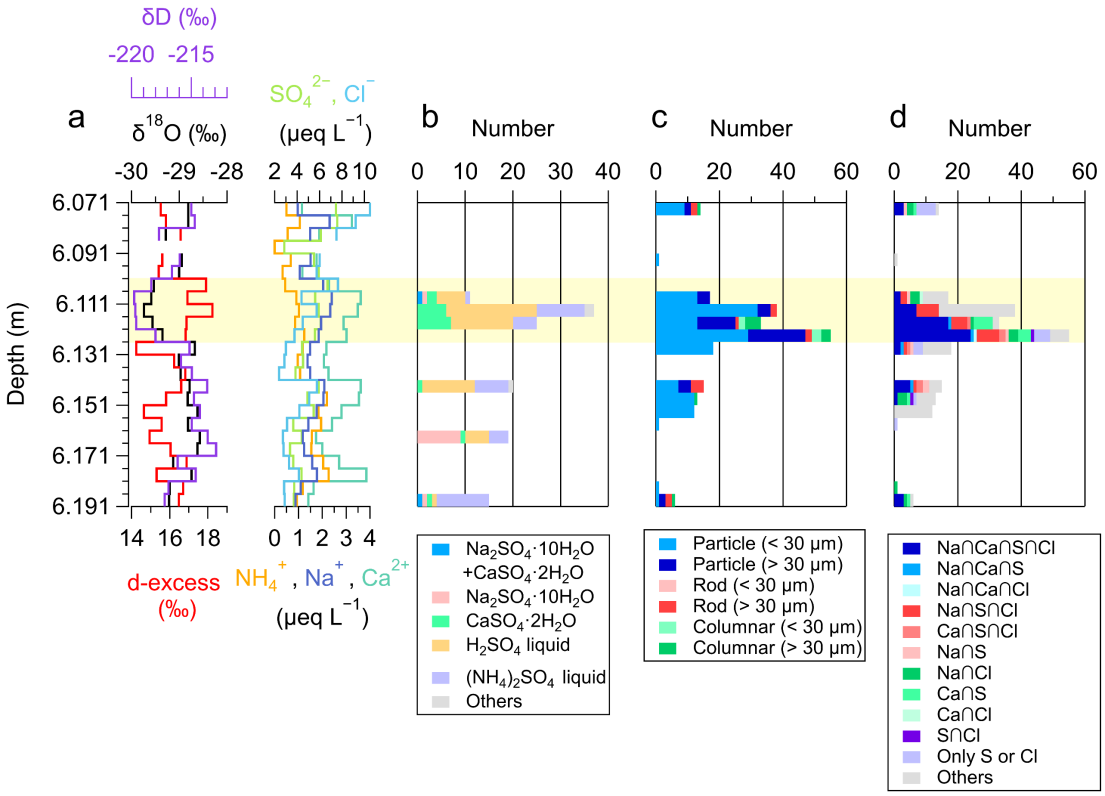

Figure 3-9 Same as Figure 3-8, except from the ice layer formed in 2006.

Table 3-3 The average of major ion concentrations (μeq L^{-1}) in the thick ice layers of 2012 and 2006.

Depth (m)	2012 ice layer			2006 ice layer	
	4.370–4.390 m[1)]	4.430–4.450 m[1)]	Rest of layer	6.101–6.126 m[1)]	Rest of layer
Cl^-	5.73	5.08	3.88	5.21	4.68
SO_4^{2-}	5.54	6.84	3.80	5.99	4.82
Na^+	4.33	4.04	3.05	2.11	1.48
NH_4^+	3.54	3.06	2.37	0.90	1.26
Mg^{2+}	1.63	1.99	1.20	2.88	2.27
Ca^{2+}	1.70	2.19	1.56	3.06	2.30
Mg^{2+}/Na^+	0.19	0.25	0.19	0.69	0.77

1) Last regions to freeze.

3.4.2 Inclusions in the two thick ice layers

The number and size of inclusions in the last region to freeze gives clues to their formation mechanism. To show an example of the spatial distribution of inclusions in the last region of the 2012 ice layer (4.370–4.390 m), Figure S1 is presented. For all inclusions in the entire 2012 ice layer, the SEM measurements give the number n and average diameter φ of 574 and 36 ± 99 μm. Considering just the last two regions to freeze (4.370–4.390 m and 4.430–4.450 m), the n and φ are 311 and 34 ± 115 μm. For the entire 2006 ice layer, these values are 224 and 37 ± 78 μm. At the last region of refreezing in the 2006 layer (6.101–6.126 m), the values are 143 and 32 ± 45 μm. Table 3-4 shows the average diameter (μm) and areas (μm^2) of three types of inclusions in the last region of refreezing in the 2012 and 2006 ice layers. Because of long length, the average diameters and areas of the rod-like inclusions are much larger than those of the particle-like and columnar-like types. For the last refreezing of 2012 and 2006 ice layers, the large rod-like inclusions are abundant (red bar in Figs. 3-8c and 3-9c; red frame on box in Figure S1). In the 2012 ice layer, 64% of the total rod-like inclusions over 100 μm in diameter occur (n=7) in the last ice to freeze (4.370–4.390 m and 4.430–4.450 m). In the 2006 ice layer, 45% (only 5) of total rod-like inclusions over 100 μm in diameter occur in the last ice to freeze (6.101–6.126 m).

Figures 3-10 show the photomicrographs of the last region of refreezing in the 2012 and 2006 ice layers. The arrows in the micrographs (Figures. 3-10a and 3-10b) show inclusions observed in the ice grains or grain boundaries. The rod-like inclusions are found along grain boundaries (e.g., Figures. 3-10a X and Y, 3-10b Z), mostly in the last regions of refreezing. In the 2012 ice layer, the largest ones are about 150 μm long and 7.8 μm wide (Figure 3-10a Y), and for the 2006 ice layer, they are about 500 μm long and 15.8 μm wide (Figure 3-10b Z). As such, they are much wider than the other filaments in ice cores that never experience melting (e.g., Baker et al., 2003). The columnar-like inclusions instead are found within the ice grain (e.g., Figure 3-10a arrow 4 and 3-10b arrow 6), whereas the particle-like inclusions (e.g., Figure 3-10a arrow 1 and 3-10b arrow 7) are found both on the grain boundary and within the ice grain.

With regard to the inclusion compositions, the Raman measurements (see section 3.3) indicate that particle-like types have a brine of NH_4^+ and SO_4^{2-} (orange and red arrows in Figures 3-10a and 3-10b) as well as salts of $Na_2SO_4 \cdot 10H_2O$ (s) and $CaSO_4 \cdot 2H_2O$ (s) (green arrow in Figure 3-10a). The columnar-like types have salts of $CaSO_4 \cdot 2H_2O$ (s) (blue arrows in Figures 3-10a and 3-10b). Additionally, the rod-like types have a brine of NH_4^+ and SO_4^{2-} (orange and red arrows in

Figures 3-10a and 3-10b). However, in the 2012 ice layer, 65% of the Raman measurements of rod-like inclusions in 4.370–4.390 m, one of the last regions to freeze, show no significant peaks (60% for the section 4.430–4.450 m). Similarly, in the 2006 ice layer, 55% of the rod-like inclusions in the last region of refreezing show no significant peaks. These rod-like inclusions are marked by white arrows in Figs 3-10a and b. The lack of peaks is consistent with the rod-like inclusions containing Cl^- and Na^+ as described in section 3.3.

Table 3-4 Average of diameters (μm) and areas (μm^2) of inclusions in the last stage of refreezing in the 2012 and 2006 ice layers, according to the SEM analysis.

		2012 ice layer	2006 ice layer
Particle	diameter	21	25
	area	871	1189
Rod	diameter	472	192
	area	33032	2159
Columnar	diameter	29	44
	area	96	116

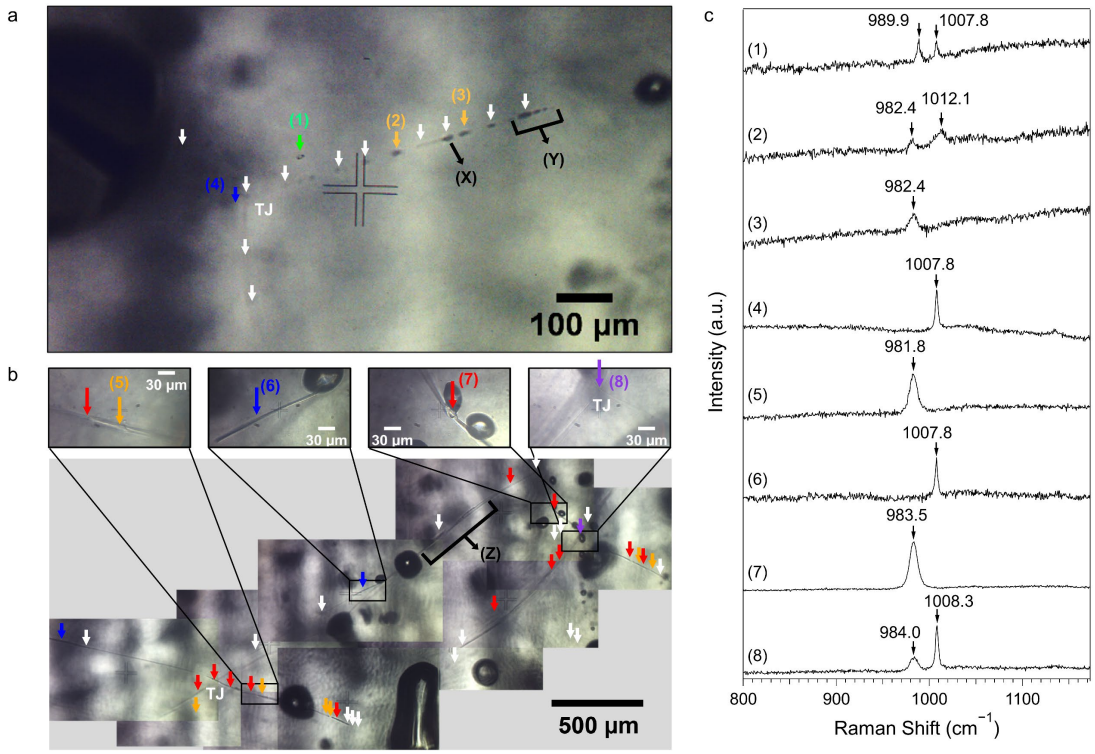

Figure 3-10 Photomicrographs and Raman spectra of inclusions. (a, b) Photomicrographs of regions within 4.370–4.380 m (last region to freeze) in the 2012 ice layer (a) and 6.116–6.121 m (last region to freeze) in the 2006 ice layer (b). The left edge is shallower depth, right edge deeper. 'TJ' indicates a triple junction. Green arrow is a particle-like inclusion of double salts of $Na_2SO_4{\cdot}10H_2O$ and $CaSO_4{\cdot}2H_2O$ within an ice grain. Orange arrows are liquid particle- and rod-like inclusions of $(NH_4)_2SO_4$ in grain boundaries. Red arrows: similar to orange arrows except H_2SO_4. Blue arrows are columnar-like inclusions of $CaSO_4{\cdot}2H_2O$ in the ice grain. The purple arrow is a particle-like inclusion of H_2SO_4 and $CaSO_4{\cdot}2H_2O$ in the triple junction. White arrows mark particle- and rod-like inclusions at grain boundaries or ice grains that have no Raman peaks detected. The black lines show a smaller rod-like inclusion (X) and larger rod-like inclusions (Y and Z). (c) Raman spectra of inclusions marked in (a) and (b).

In considering how an inclusions composition relates to its size, the relationship between the atomic fractions of Na, S, Cl, and Ca v.s. inclusions cross-sectional area was examined. The sum of four fractions equals 1. For the inclusions in the last stage of refreezing, the fractions of Ca in Figure 3-11 decrease significantly as the inclusion areas increase. Similarly, the fractions of S decrease gradually as the inclusion areas increase in the 2012 ice layer (4.370–4.390 m) and 2006 ice layer. The fraction of Na also decreases gradually, reaching about 0.4 in the largest areas. For the 2012 ice layer (4.430–4.450 m), the fraction of Cl instead increases to about 0.5 as the areas increase (Figure 3-11b). In contrast, in the 2012 ice layer (4.370–4.390 m) and 2006 ice layer, the fraction of Cl has no significant change. However, the fraction of Cl is probably the same as Na, since the fractions of S and Ca decrease to 0 as the inclusion areas increase. Given that the area of the rod-like inclusions tends to be large, these results suggest that large rod-like inclusions in the last region of refreezing consist mainly of Na and Cl elements, with relatively little S and Ca. As described above, the rod-like inclusions show no significant Raman peaks, consistent with a large amount of Na^+ and Cl^- (brine) in the rod-like inclusions. In contrast, S and Ca increase as the areas decrease.

In summary, the smaller columnar-and particle-like inclusions of solid $Na_2SO_4 \cdot 10H_2O$ and $CaSO_4 \cdot 2H_2O$ form within the ice grains. Particle-like inclusions of brines with Na^+, Cl^-, NH_4^+, and SO_4^{2-} form in grain boundaries. And, in the case that the meltwater has sufficient concentration of impurity, large rod-like inclusions of brines with mainly Na^+ and Cl^- form in grain boundaries.

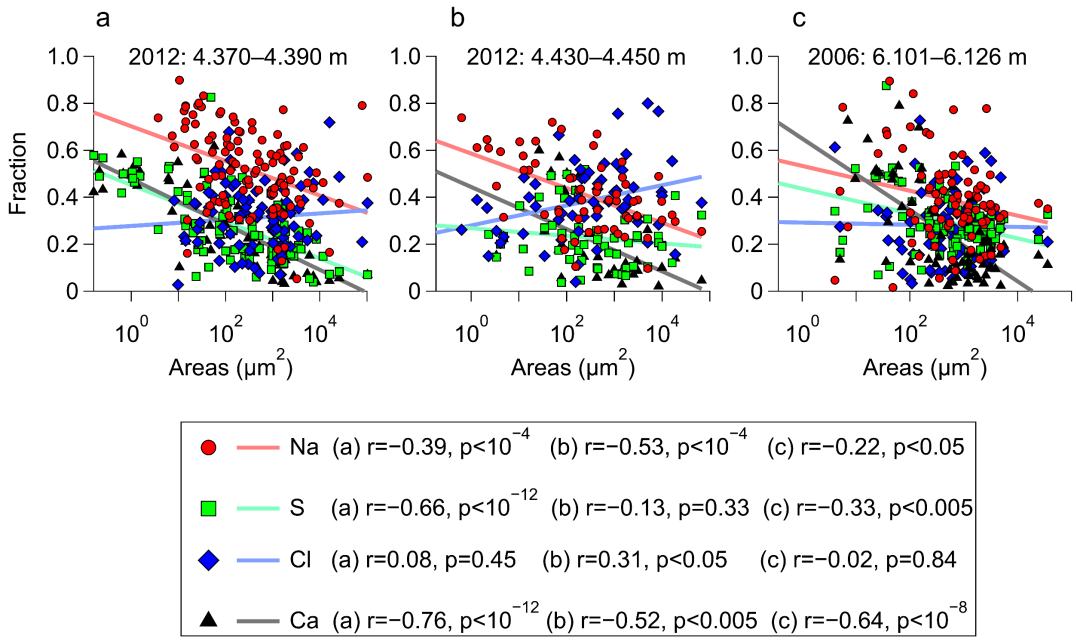

Figure 3-11 The fractions of Na (red), S (green), Cl (blue), and Ca (black) of a given inclusion and the inclusion area (μm^2) for inclusions formed in the last region of refreezing. Also shown are the liner regression of the data for each element. Each of correlation coefficient (r) and p-value are in the box. Since inclusions without Na, S, Ca, and Cl have mainly Si, we consider them as insoluble inclusions and do not plot them here.

4 The characteristics of inclusions in ice layers of SE-Dome II ice core

4.1 Ice core chronology and ice layers of SE-Dome II ice core

Figure 4-1 shows the time horizons in the SE-Dome II ice core determined from melt events, the tritium peak, and volcanic events. Extensive melt features are found in a range from 16.652 m to 17.356 m including two ice layers of 11 mm and 6 mm in thickness as well as two LPI of 130 mm and 530 mm in thickness (Figure 4-1a). Based on the annual accumulation rate from the SE-Dome I ice core (1.02 ± 0.21 m yr^{-1}; Furukawa et al., 2017), the melt event detected in the range from 16.652 m to 17.356 m is probably due to an extreme melting event in 2012 (Nghiem et al., 2012; 'ME2012' in Figure 4-1a). In the deeper core section, an ice layer with 30 mm in thickness is observed at 167.024–167.054 m depth. This is the only thick ice layer below 150 m depth and probably corresponds to the melting event in 1889 the widely found in Greenland ice cores (e.g., Neff et al., 2014; 'ME1889' in Figure 4-1a).

The time horizon is also determined by the tritium peak originating from the H-bomb test. A sharp tritium peak was found at 84.920−85.469 m depth ('TU1963' in Figure. 4-1b), which accounted for the H-bomb test in 1963 (Clausen and Hammer, 1988). Figure 4-1b shows the depth profile of electrical conductivity. The baseline increases to about 80 m and then shows no change to the bottom of the ice core. The electrical conductivity peaks indicate the depths with high acid concentration, implying volcanic events or high emission of anthropogenic substances. The three highest peaks (> 35 μS m^{-1}) were found at 80.225 m, 143.070 m, and 236.220 m depth. Following volcanic chronologies of the NEEM ice core and the Humboldt ice core in central Greenland (e.g., Sigl et al., 2013), colossal eruptions such as Katmai (Volcanic Explosivity Index (VEI) > 6) in 1912 and Tambora (VEI > 7) in 1816 are preserved obviously in the Greenland ice core. Hence, the two highest peaks at 143.070 m and 236.220 m depth provide time horizons corresponding to 1912 ('KTM1912' in Figure 4-1b) and 1816 ('TMB1816' in Figure 4-1b). Since the high peak at 80.225 m depth is recorded after the tritium peak in 1963, it is interpreted as the high anthropogenic substances such as SO_4^{2-} during the 1970s (Fischer et al., 1998). In summary, five-time horizons were detected, corresponding to 2012, 1963, 1912, 1889, and 1816 in the whole SE-Dome II ice core.

Figure 4-1c and Figure 4-2 shows the depth profile of H_2O_2 concentrations. The average concentration is 71.0 ± 58.5 μg kg^{-1}. The minimal and maximal H_2O_2 peaks were counted to estimate annual layers. These annual layers are consistent with the five-time horizons (2012, 1963, 1912, 1889, and 1816) (light blue lines in Figure 4-1), validating its accuracy. Thus, the ice-core time scale established here with an accuracy of less than a year provides an important basis for precise reconstruction of the histories of climate and aerosols for the industrial period (221 years, from 1799 to 2020).

Surface melting and high amount of impurities may decrease the H_2O_2 concentrations in snowpack (Anklin et al., 1998). Thus, extreme melting such as in 2012 and high impurity content by volcanic eruptions near Greenland may affect the H_2O_2 records in the SE-Dome II core, providing excellent opportunities for age validation, as follows. Around 13.021 m depth corresponding to the autumn of 2014, the H_2O_2 concentration is low due to the high dust flux from the eruption of Mt. Bardarbunga in Iceland in the autumn of 2014 (Figure 4-2(a), and 'BDB2014' in Figure 4-3a; Amino et al., 2021). The collapsed H_2O_2 peak at around 16.770 m is due to the extreme melt event in 2012 (Figure 4-2(b)). At 31.266 m depth, the H_2O_2 peak is low, which is probably due to the high dust concentration in the summer of 2003 (Figure 4-2(c); Amino et al., 2021). The collapsed peak of 217.170 m was probably caused by the high amounts of impurities in 1836 caused by the eruption of Mt. Coseguina in Nicaragua (Figure 4-2(d) and 'CSG1836' in Figure 4-3a). As a consequence, these event layers are fully compatible with those from H_2O_2 counting, supporting the robustness and reliability of our annual layer counting method. While time scales in other ice cores often have errors, for example, one of which is estimated to be 1–10% (Meese et al., 1997), our time scale found in the SE-Dome II ice core is highly precise with a half-year accuracy.

The bulk density is 423 kg m^{-3} at the top section in range of 1.27–1.76 m depth and increases with depth as plotted in Figure 4-1a. At about 88 m, the close-off density of 830 kg m^{-3} is reached. Deeper than the close-off depth, the bulk density still increases with bubble compression and finally reaches 900 kg m^{-3}. Figure 4-1a also shows the profile of high-resolution density. As with the bulk density, the high-resolution density increases with depth and reaches a close-off density at the depth of 88.9 m. In the deeper part of the ice core, the high-resolution density converges to 917 kg m^{-3} with much less variability than the bulk density. The high-resolution density profile shows high peaks that correspond to visually observed ice layers and

LPI, as shown in Figure 4-1a. The high-resolution density profile of the SE-Dome II ice core is similar to that of the SE-Dome I ice core (Iizuka et al., 2017) as expected from their proximity. For example, the close-off density is reached at 86.8 m depth in the SE-Dome I ice core, while 88.9 m in the SE-Dome II ice core.

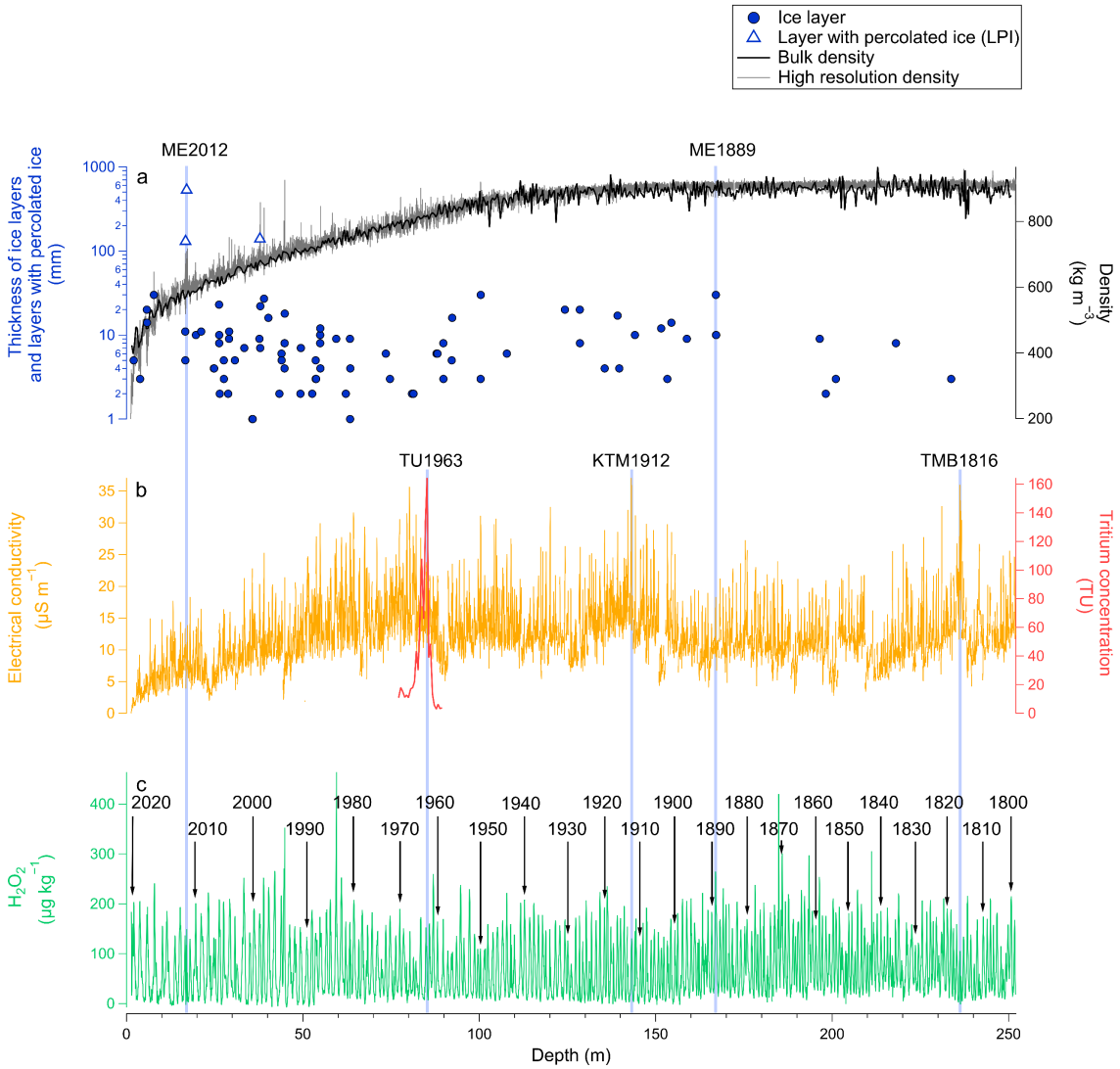

Figure 4-1 Depth profiles of (a) bulk density (kg m^{-3}), high-resolution density (kg m^{-3}) and thickness of ice layers and the layer with percolated ice (LPI) (mm), (b) electrical conductivity (μS m^{-1}) and Tritium concentration (TU) from 76.831 m to 89.750 m in depth, and (c) H_2O_2 concentration (μg kg^{-1}). 'ME2012', 'ME1889', 'TU1963', 'KTM1912', and 'TMB1816' indicates the melting events in 2012 and 1889, the tritium peak in 1963, and the eruption events in 1912 and 1816.

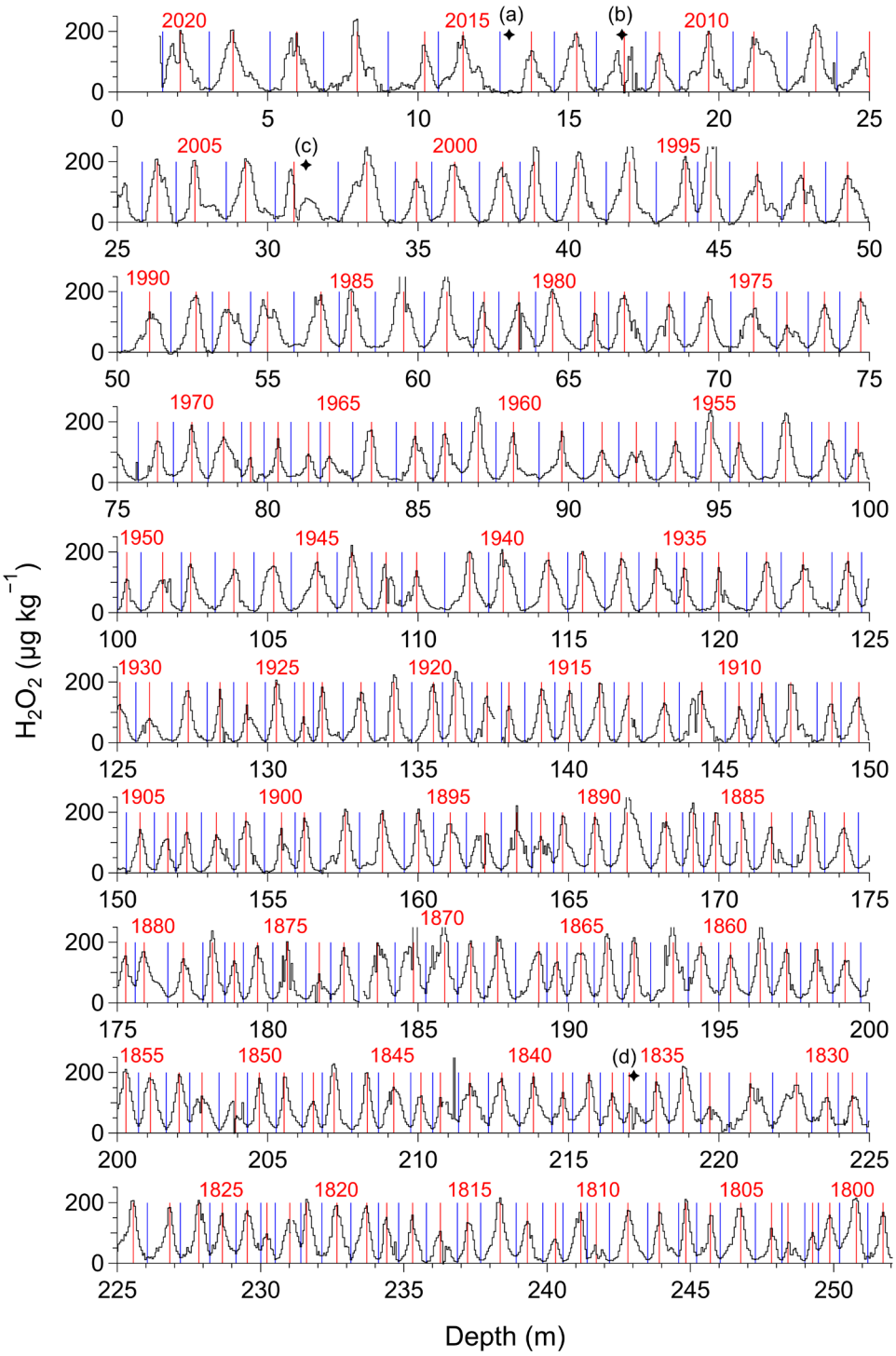

Figure 4-2 Depth profiles of H_2O_2 concentrations. The red and blue lines show the mid-summer and mid-winter each year. Low H_2O_2 concentrations are detected due to (a) the high dust flux from the eruption of Mt. Bardarbunga in Iceland in the autumn of 2014 (Amino et al. 2021), (b) the extreme melt event in 2012, (c) high dust concentration in 2003 (Amino et al., 2021), (d) the eruption of Mt. Coseguina in Nicaragua in 1835.

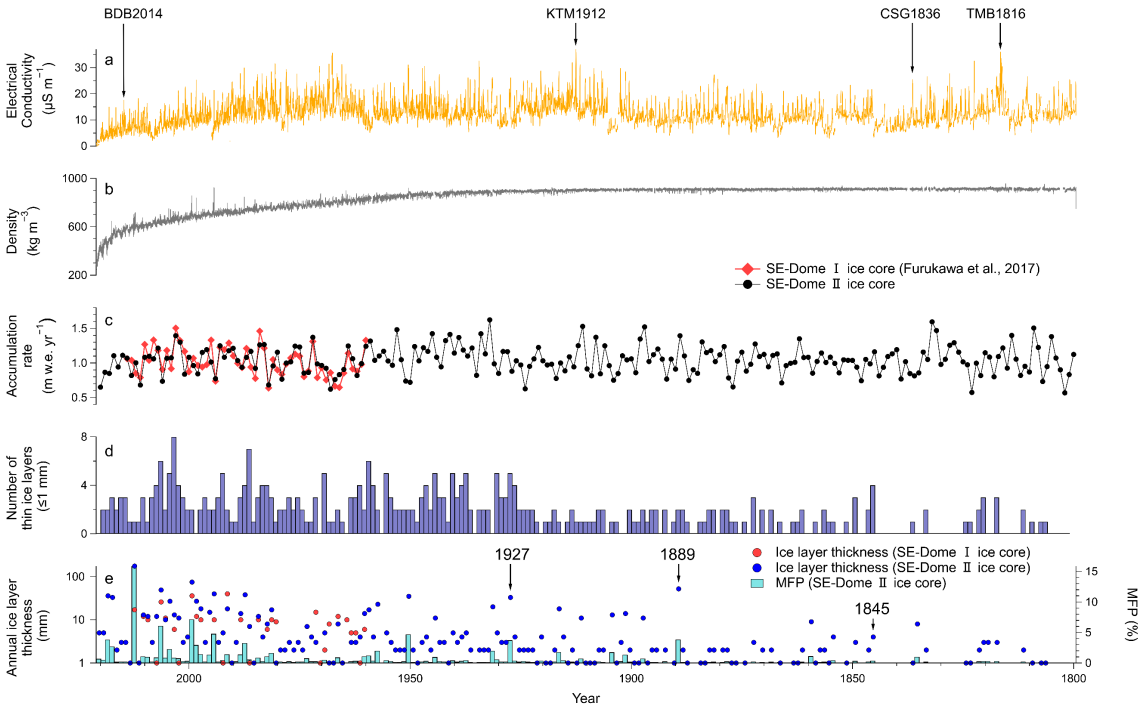

Figure 4-3 Time series of proxies in the SE-Dome II ice core. (a) Electrical conductivity (μS m^{-1}), (b) high-resolution density (kg m^{-3}), (c) accumulation rate reconstructed from the SE-Dome II ice core and the SE-Dome I ice core (m w.e. yr^{-1}) (Furukawa et al., 2017), (d) the number of thin ice layers of 1 mm or less in thickness per year, and (e) ice layer thickness and melt feature percentage (MFP) per year during 1800–2020 and ice layer thickness per year in the SE-Dome I ice core (Iizuka et al., 2017). 'BDB2014', 'KTM1912', 'CSG1836' and 'TMB1816' indicate the eruption events in 2014, 1912, 1836 and 1816.

Each annual layer thickness of the ice core is converted into the original thickness at the time of accumulation by correcting for the thinning due to ice flow, with the Nye model (Paterson, 2006) and the estimated ice sheet thickness of 1000 m (Figure 4-4). The Nye model is sufficient for the thinning correction because the SE-Dome II ice core (250 m) only covers the top quarter of the total ice sheet thickness. Then, the water equivalent accumulation rate during 1800–2020 from the SE-Dome II ice core was calculated using the annual average of high-resolution density (Figure 4-3c). The result indicates that the largest and smallest annual accumulation rates of 1.62 and 0.57 m w.e. yr^{-1} occurred in 1932 and 1802, respectively. The average of annual accumulation rate during 1800–2020 is 1.04 ± 0.20 m w.e. yr^{-1} (Table 4-1). The SE-Dome II annual accumulation rates during 1960–2014 well agree with that of the SE-Dome I ice core with the SEIS2016 age scale (1.02 ± 0.21 m yr^{-1} during 1960–2014; Furukawa et al., 2017; Figure 4-3c), supporting the robustness of our result. According to the nonparametric Mann–Kendall test for monotonic trends (Mann, 1945; Kendall, 1975), the annual accumulation rate during the past 221 years shows no significant temporal trend (Figure 4-5a). According to the precipitation rates based on the compiled data of Greenland ice cores (Mernild et al., 2015), the precipitation rates also show no significant trend during 1890–2000 in northern Greenland. In contrast, in southwestern Greenland, the increase in precipitation rate during 1890–2000 is observed (Mernild et al., 2015). These indicate that there are differences in the trends of the accumulation rates between the western and eastern regions of Greenland, even within the same southern regions.

The day of winter and summer solstice (December 21st and June 21st) was tied to H_2O_2 minimal and maximal, respectively. Between the day of winter and summer solstice we use linear interpolation to determine time scale. Based on the modeled monthly atmospheric H_2O_2 concentration (Figure. 2-5), H_2O_2 variations are similar to sinusoidal waves in 221 years (Figure. 4-2), indicating that there is little difference among seasonal accumulation rates. Then, a year was divided into four seasons: spring (March–May), summer (June–August), autumn (September–November), and winter (December of the last year to February). The seasons were divided into March 1, June 1, September 1, and December 1 as the seasonal boundaries. The seasonal accumulation rates thus reconstructed with the high-resolution density during 1800–2020 are 0.27 ± 0.07 m, 0.26 ± 0.06 m, 0.25 ± 0.07 m, and 0.26 ± 0.06 m for spring, summer, autumn, and winter, respectively, which show no difference between the seasons as expected from the previous study with a seasonal time scaling with ~2 months error (Furukawa et al., 2017; Table 4-1 and Figure

4-5). The accumulation rates maxima are 0.50 m (spring in 2003), 0.41 m (summer in 1831), 0.44 m (autumn in 1831), and 0.46 m (winter in 2003), while the minima are 0.12 m (spring in 1802), 0.12 m (summer in 2020), 0.09 m (autumn in 2020), and 0.14 m (winter in 1811). The highest accumulation rate in the spring of 2003 was due to an extreme snowfall event in the southeastern of Greenland in April 2003 (Nghiem et al., 2005). There are no significant long-term trends in all seasons during 1800–2020. Comparing the seasonal accumulation rates of the SE-Dome II and SE-Dome I ice cores (Furukawa et al., 2017), the correlation coefficients for summer, autumn, and winter are statistically significant (Table 4-1). For spring, the average accumulation rates are consistent between the two ice cores despite no significant correlation. Thus, we consider that the assumption of equal seasonal intervals in this study is appropriate, given that the seasonal accumulation rates are generally consistent with the previous study in the SE-Dome I ice core with a seasonal time scaling with ~2 months error using a different method, $\delta^{18}O$ record (Furukawa et al., 2017). Hence, it is concluded that proxies with seasonal time-scale can be obtained from the SE-Dome II ice core.

Then, the accumulation rates of the SE-Dome II ice core and the precipitation rate from ERA5 (Figure 4-5) were compared. The ERA5 precipitation rate during 1950–2020 has an average of 0.96 ± 0.19 m yr^{-1}. Figure 4-6 shows the relationship between the annual accumulation rate from the SE-Dome II ice core and the precipitation rate data from ERA5 during 1950–2020. The ERA5 precipitation rate is consistent with the accumulation rates of the SE-Dome II ice core within the error. Notably, the correlation coefficient is significant in 1950–2020 ($r = 0.61$; Fig. 4-6 and Table 4-1). The slopes of regression lines are 0.61 (Fig. 4-6), indicating that the ERA5 reanalysis data has a little underestimation compared to the accumulation rates of the SE-Dome II ice core. Nevertheless, the ERA5 precipitation rate is also consistent with the accumulation rates of the SE-Dome II ice core within the error range.

For the seasonal accumulation, the correlations are statistically significant for winter, spring and autumn between the accumulation rate from the SE-Dome II ice core and the precipitation rate from ERA5 during 1950–2020 (Figure 4-5b, d, e, and Table 4-1). However, for the summer accumulation, there are no significant relationships (Figure 4-5c and Table 4-1). In summer, the accumulation rate reconstructed from the SE-Dome II ice core is 0.23 ± 0.05 m w.e. yr^{-1}, which is twice larger than that of ERA5, 0.15 ± 0.05 m yr^{-1}. This discrepancy was also found in the SE-Dome I ice core, probably due to the underestimation of precipitation amount during

summer by ERA-interim data (Furukawa et al., 2017). In contrast, the disagreement between the accumulation rate from the SE-Dome I ice core and the precipitation rate by ERA-interim data during winter (Furukawa et al., 2017) was not observed in this study, supporting the improvement in the ERA5 reanalysis data (Hersbach et al., 2020). Although the reanalysis data have improved, there is still an underestimation during summer in the ERA5 data. This underestimation during summer in the ERA5 (Zhang et al., 2022) could be explained by the seasonal difference in Tasiilaq, located on the coast of the SE-Dome site, assimilated to the ERA5 analysis, given that the precipitation in summer in Tasiilaq is lower than that in winter (Balascio et al., 2013). The ice core results suggest the need to re-evaluate the ERA5 data, as there are few reliable accumulation data for reanalysis in Greenland.

The accumulation rate has reconstructed by various models such as regional climate models (RCMs) and general circulation models (GCMs) (Fettweis et al., 2020). Fettweis et al (2020) aimed to improve on these uncertainties by intercomparing different types of these models, which are forced by the same ERA-Interim reanalysis forcing field. However, the discrepancies among the modeled snow accumulation rates are large, particularly in the southeast accumulation zone with large discrepancies (2.0 m yr^{-1}). In this study, *in situ* accumulation rates for 221 years are reconstructed, which is based on half-year accuracy time-scale with seasonal level.

As mentioned above, the extreme snowfall event happened in April 2003 in southeastern Greenland (Nghiem et al., 2005). In the periods with ERA5 reanalysis data, a higher annual accumulation rate than that in 2003 was only found in 1953 (1.48 m w.e. yr^{-1}). In contrast, higher annual accumulation rates than that in 2003 are found in 1945 (1.42 m w.e. yr^{-1}), 1941 (1.41 m w.e. yr^{-1}), 1934 (1.42 m w.e. yr^{-1}), 1932 (1.62 m w.e. yr^{-1}), 1911 (1.53 m w.e. yr^{-1}), 1897 (1.52 m w.e. yr^{-1}), 1832 (1.60 m w.e. yr^{-1}), 1831 (1.47 m w.e. yr^{-1}), 1814 (1.40 m w.e. yr^{-1}), and 1809 (1.50 m w.e. yr^{-1}), which are observed when ERA5 is not available. In these years except 1945, 1941, 1897, 1831, and 1814, the highest season of accumulation rate is spring. The extreme snowfall in April 2003 in southeastern Greenland was due to large and frequent storms caused by the blocking pattern of relatively high pressure over the Norwegian Sea and relatively low pressure over southeastern Greenland (Box et al., 2005; Hanna et al., 2006). Our result suggests that such a blocking pattern in spring was likely to occur eight times. Although there are high accumulation rates described above, the annual accumulation rate shows no significant temporal

trend during 1800–2020. This result indicates that the annual accumulation rate in the SE-Dome site is constant regardless of temperature warming.

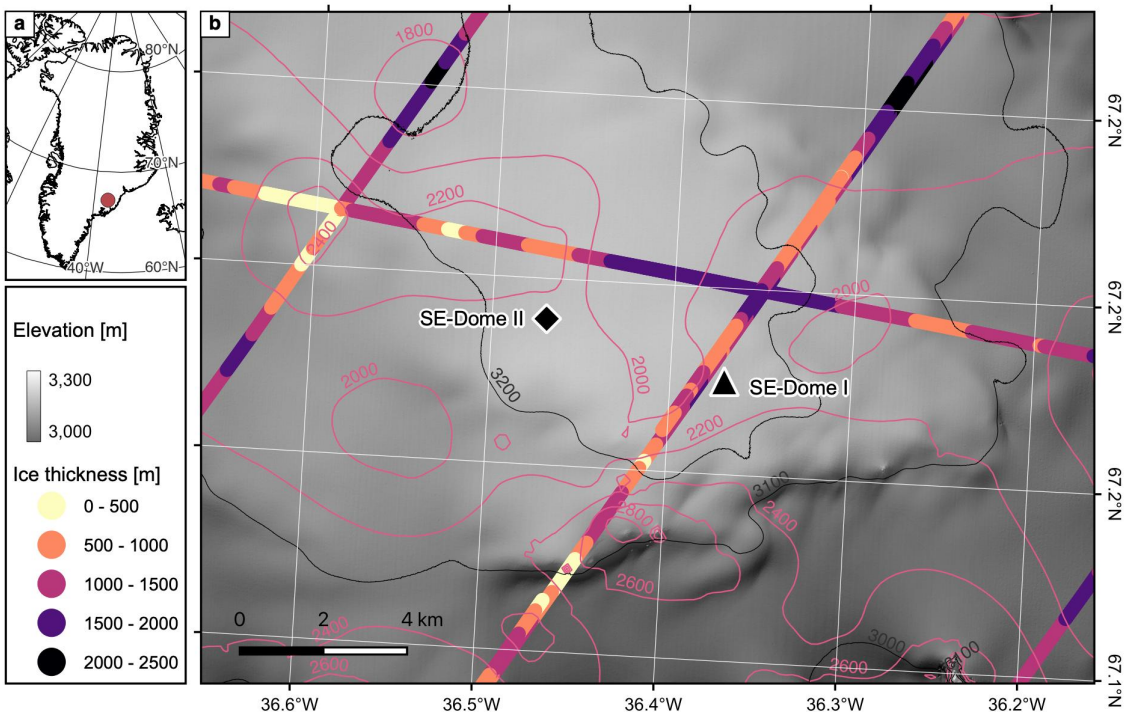

Figure 4-4 The map of SE-Dome site (Minowa, personal communication). **(a)** The location of the SE-Dome drilling site in Greenland (red circle). **(b)** The drilling site of SE-Dome I ice core (triangle, Iizuka et al., 2016) and SE-Dome II ice core (rhombus, Iizuka et al., 2021). Black and magenta solid lines indicate the surface and the bed elevations of the Greenland Ice Sheet, respectively. The contour intervals are 200 m. The ice surface elevation is based on ArcticDEM v3 (Porter et al., 2018). The bedrock topography is based on BedMachine v3 (Morlighem et al., 2017). The colored line indicates the ice thickness of the ice sheet obtained by airborne radar survey (IceBridge MCoRDS L2 Ice Thickness v1, Paden et al., 2010).

Table 4-1 The annual and seasonal accumulation rate (m w.e. yr^{-1}) from SE-Dome I core during 1960–2014 and SE-Dome II ice core during 1800–2020, and precipitation rate (m yr^{-1}) from ERA5 during 1950–2020, and the correlation coefficients of their comparisons.

	Spring (MAM)	Summer (JJA)	Autumn (SON)	Winter (DJF)	Annual
Precipitation rate from ERA5 (m yr^{-1})	0.23 ± 0.09	0.15 ± 0.05	0.27 ± 0.10	0.32 ± 0.11	0.96 ± 0.19
Accumulation rate from SE-Dome I ice core (m w.e. yr^{-1})	0.25 ± 0.07	0.25 ± 0.09	0.27 ± 0.09	0.25 ± 0.07	1.02 ± 0.21
Accumulation rate from SE-Dome Ⅱ ice core (m w.e. yr^{-1})	0.27 ± 0.07	0.26 ± 0.06	0.25 ± 0.07	0.26 ± 0.06	1.04 ± 0.20
Correlation between ERA5 and SE-Dome Ⅱ	0.66 (p<0.001)	0.18 (ns)	0.43 (p<0.001)	0.63 (p<0.001)	0.61 (p<0.001)
Correlation between SE-Dome Ⅰ and SE-Dome Ⅱ	0.18 (ns)	0.53 (p<0.001)	0.50 (p<0.001)	0.48 (p<0.001)	0.73 (p<0.001)

ns: not significant

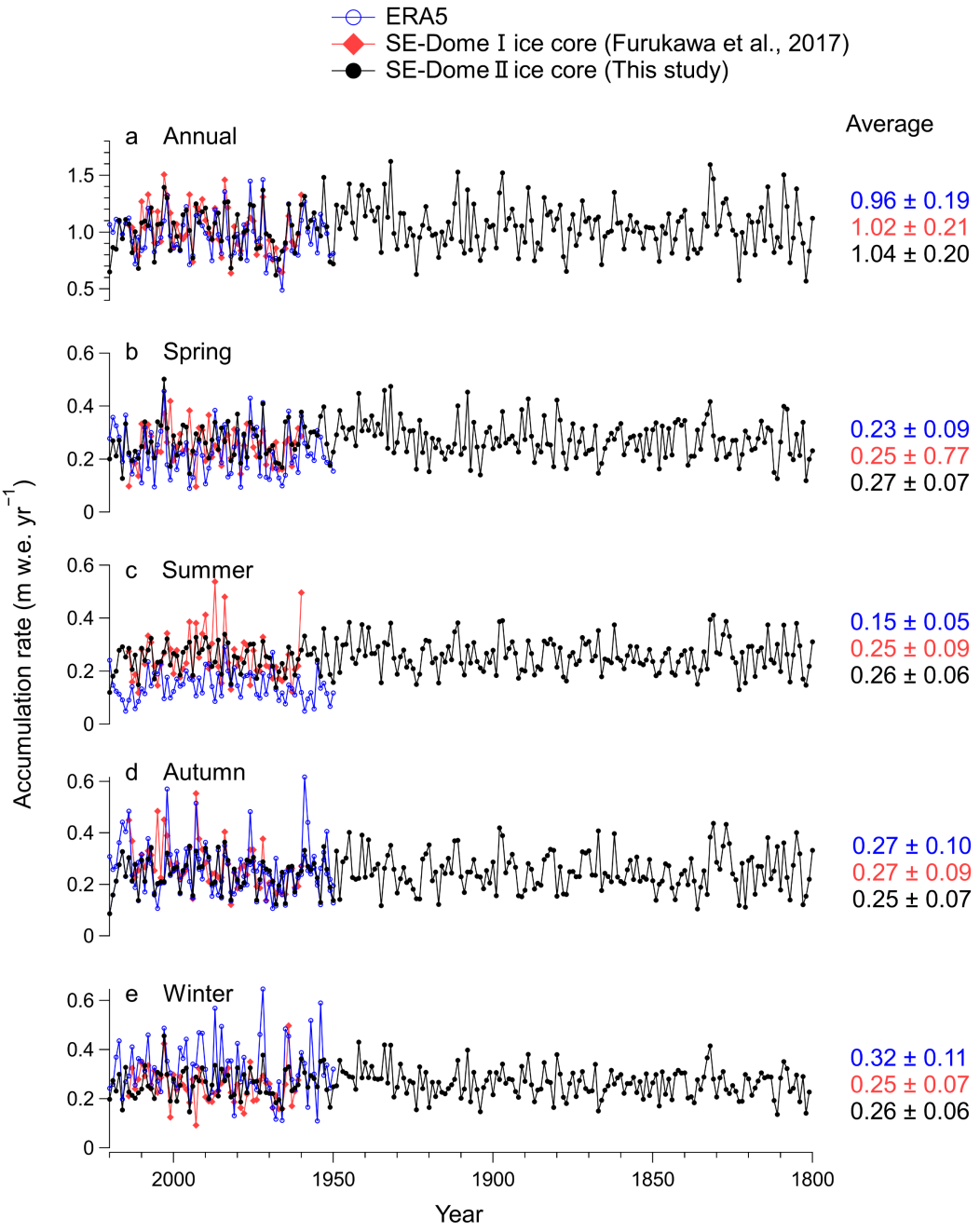

Figure 4-5 The accumulation rate reconstructed from the SE-Dome II ice core (black) during 1800–2020 and the precipitation rare from ERA5 (blue) during 1950–2020. (a) annual accumulation rate. (b-e) Same as (a) but for spring, summer, autumn, and winter, respectively. The red lines are the annual and seasonal accumulation rate of the SE-Dome I ice core during 1960–2014 (Furukawa et al., 2017).

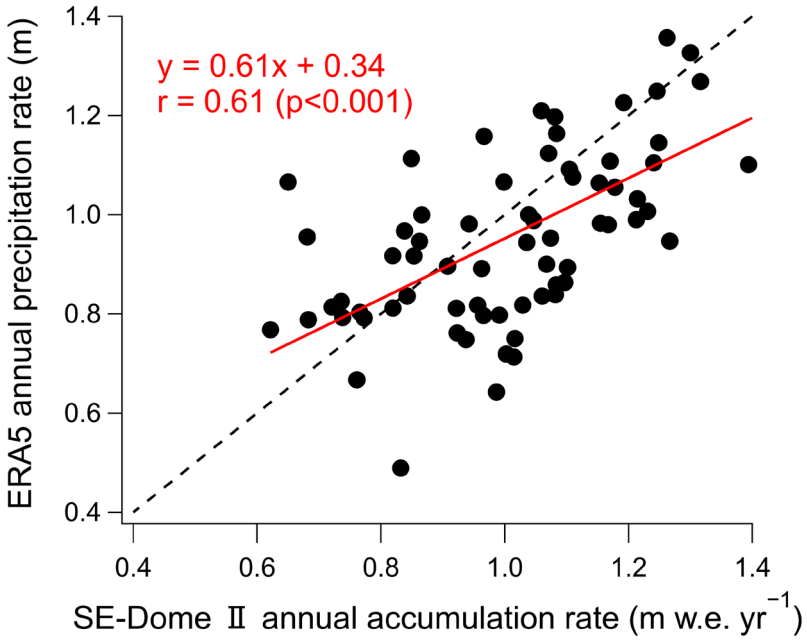

Figure 4-6 The relationship between the annual accumulation rate from the SE-Dome II ice core and the precipitation rate from ERA5 during 1950–2020.

86 ice layers and three LPI were observed in the SE-Dome II ice core (Figure. 4-1a). The average thickness is 8.37 ± 6.96 mm for ice layers, which has increased since 1995 (32 ice layers with an average of 9.31 ± 7.56 mm). The LPI were only observed since 1999, at 16.693–16.823 m (130 mm in thickness) and 16.826–17.356 m (530 mm in thickness) in 2012, and at 37.784–37.922 m (138 mm in thickness) in 1999.

As mentioned in section 2.3.1, the ice layer is originated from the refrozen aquifer (Figure 4-7a) and the LPI is originated from refrozen meltwater during percolation without forming an aquifer (Figure 4-7b). The ice layer thickness is a proxy for the amount of refrozen meltwater (Trusel et al., 2018). In the case of LPI, the amount of refrozen meltwater was estimated as follows. The positive anomaly in high-resolution density for the LPI relative to the neighboring depths should reflect the amount of percolated ice. I calculated the residuals of the density of the LPI and the ice layer relative to those of the 1-m average around the LPI and the ice layer. It is assumed that the 1-m average density represents layers without ice. Then the ratio of the density residual of the LPI to that of the ice layer was obtained. This ratio enables us to convert the length of the LPI to the equivalent length of the average ice layer. By this estimation, these ice-layer equivalent thicknesses are 31.20 mm and 127.20 mm for 2012, and 72.25 mm for 1999. The ice layers greater than 1 mm in thickness are 89 layers with an average thickness of 10 mm including the thickness equivalents of the LPI.

The number of thin ice layers less than 1 mm is 355 during 1800–2020, which has increased since 1920 (259 layers; Figure 4-3d). These thin layers are typically observed in the snowpack as crusts (e.g., Fegyveresi et al., 2018; Weinhart et al., 2021). Crusts commonly show high density but can be formed in different environmental conditions: strong solar radiation, high temperature, strong wind, low relative humidity, and eventually accumulation, etc. Weinhart et al (2021) suggest that there is a positive correlation (R^2=0.89) between the logarithmic accumulation rate and crust numbers per annual layer in the surface snow of both Antarctica and Greenland. However, in this study, the annual number of thin ice layers and accumulation rate at the SE-Dome site do not show their proposed relation (r = 0.13, p =0.06). After 1920, the number of thin ice layers is higher in warm periods during the 1940s–1950s and recent decades than in cold periods during the 1960s–1970s. Therefore, it is suggested that these layers were originally formed on warm days in summer by minor surface melting rather than by other mechanisms such

as the strong winds (Figure 4-7c). In the following, the thin ice layers are defined as ice layers with 1 mm in thickness.

Figure 4-3e and Figure 4-8 shows the ice layer thickness per year during 1800–2020 including the thickness equivalents of the LPI and thin ice layers. The average annual ice layer thickness is 5.74 ± 14.95 mm. The annual ice layer thickness increased in warm periods during the 1940s–1950s, decreased in cold periods during the 1960s–1970, then has increased since 1995 (the average thickness of 21.51 ± 35.13 mm; Figure 4-3e and Figure 4-8). Figure 4-3e and Figure 4-8 also shows the average thickness in the SE-Dome I ice core (Iizuka et al., 2017). The number of annual ice layers in the SE-Dome I ice core is 33 with an average thickness of 5.64 ± 8.64 m during 1960–2015. Similar to the SE-Dome II ice core, the annual ice layer thickness in the SE-Dome I ice core has increased in warm periods, whereas decreased in cold periods. Figure 4-8 also shows the annual ice layer thickness of ice layers in the SIGAMA-A ice core. The variations of the SE-Dome I ice core and the SE-Dome II ice core show the same trend, being consistent with the annual ice layer thickness of the SIGMA-A ice core. The melt feature percentage (MFP) profile of the SE-Dome II ice core is also described in Figure 4-3e. The MFP of the SE-Dome II ice core has increased during the warm periods of 1940s–1950s and recent decades, while has decreased during cool periods of 1960s–1970s. These variation shows the same trends, being consistent with the MFP of the SIGMA-A ice core (Fig. 3-1b).

The relationship between the thickness of the ice layers and the summer temperature by ERA 5 data at the SE-Dome site were investigated. ERA5 had been quality-assured from 1979 to the present, and recently the period 1958–1978 was also quality-assured. Then, the threshold temperature T_T (°C) was changed from –8.0 °C to 0 °C at an 0.5 °C interval and obtained the correlation coefficients with the thickness of the ice layer during three periods: 1950–2020, 1958–2020, and 1979–2020 (Figure 4-9). Figure 4-9 also shows the relationships between annual ice layer thickness and PDH at the T_T of –4.5°C with the best correlation coefficients (r = 0.68, p < 0.001; Fig. 4-9a, r = 0.69, p < 0.001; Fig. 4-9b, and r = 0.80, p < 0.001; Fig. 4-9c). The period during 1979–2020 shows the best correlation. Nevertheless, all three periods show significant positive correlation coefficients. The threshold value could be attributed to a bias in the ERA5 temperature. Despite the uncertainty in threshold value, these results suggest that the interannual variability of ice layer thickness is consistent with that of and summer mean temperature at the

SE-Dome site. In other words, the ice layer thickness can be a proxy for the summer mean temperature.

High MFPs were found in 1927 and 1889 when the ERA5 data is not available (Figure 4-3e). During most summers, the surface melting has seldom occurred in the highland dry snow regions in the Greenland ice sheet. However, in 1889, the widespread melting that extended inland happened because of unusual warming and reduced albedo by black carbon deposited by a forest fire (Keegan et al., 2014). The ice layers formed by the 1889 melt event are also detected in other ice cores: for example, summit, NEEM, ACT-3, and D4 ice cores (Keegan et al., 2014). As described in Chylek et al (2006), the period during 1920–1930 is strongly warming decade. The seasonal time scale and ice layer detection suggests that the summer in 1927 was exceptionally warm in the strongly warming decade. An ice layer in 1927 is also observed in the ACT-3 ice core (Das et al., 2009), suggesting the 1927 surface melting event was extensive over the inland (at least in southern and southeastern) Greenland. In Greenland, the Little Ice Age ended up in the last half of the 19th century (Kaufman et al., 2009). The frequency of ice layers had increased since 1845, suggesting the Little Ice Age may ended up in 1845 in the SE-Dome region.

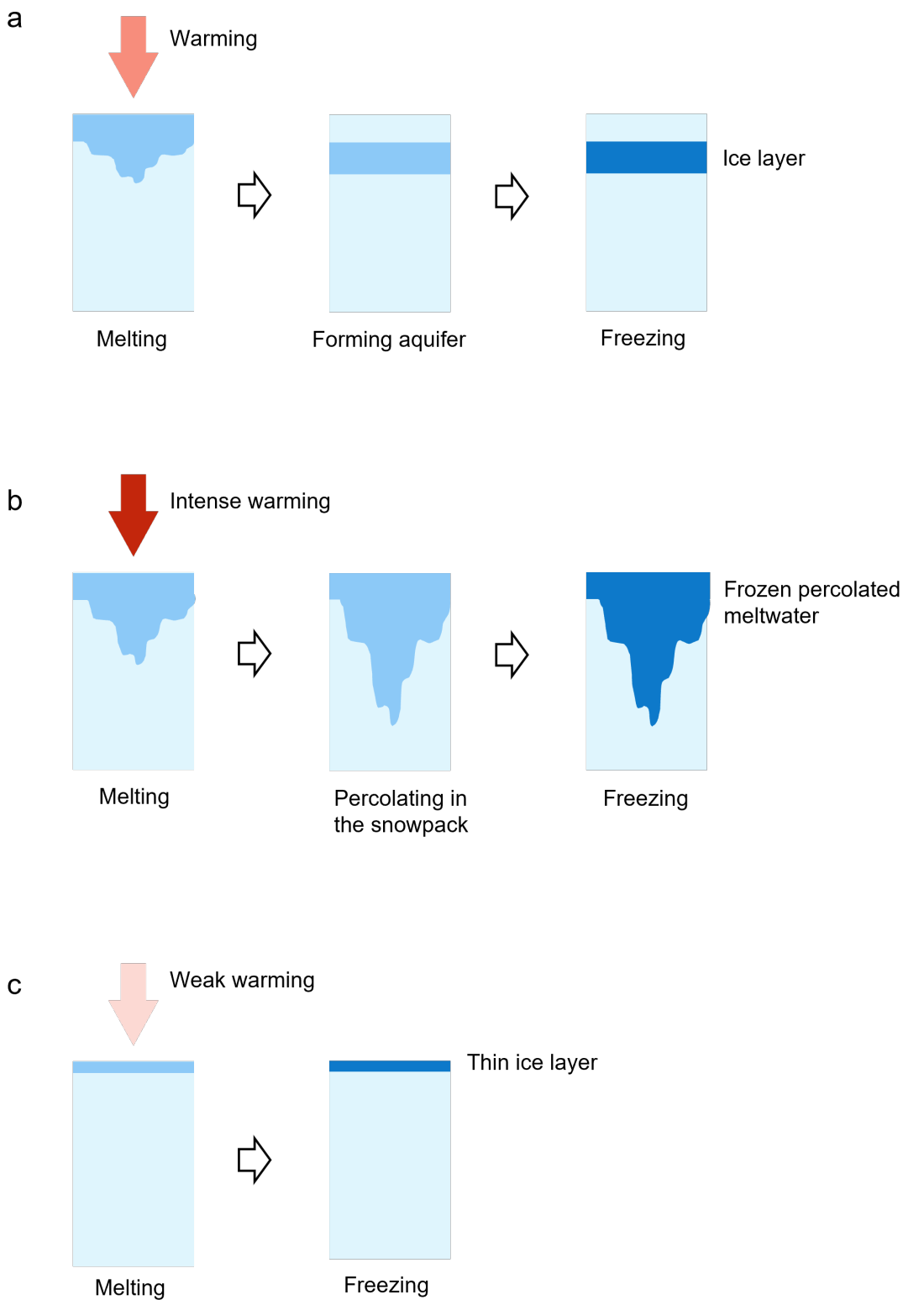

Figure 4-7 Proposed forming processes of (a) the ice layer, (b) the LPI, and (c) the thin ice layer.

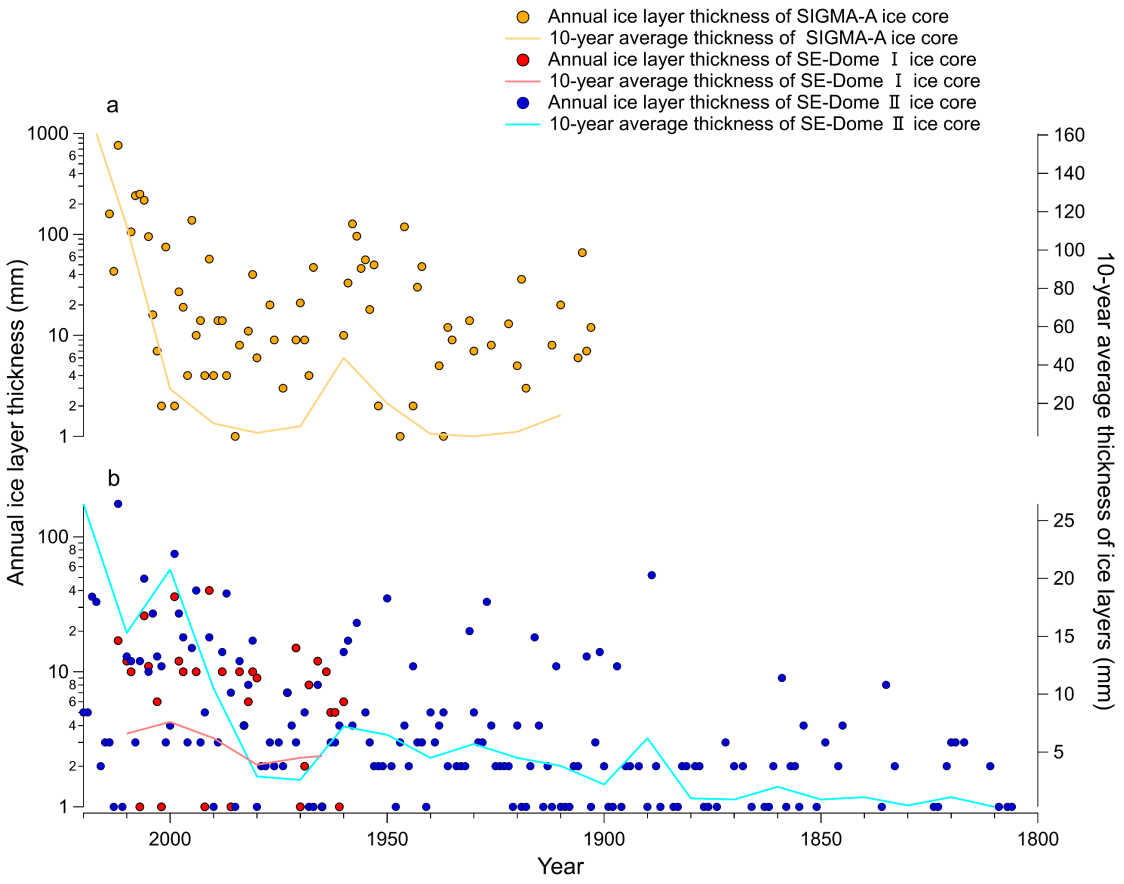

Figure 4-8 Annual ice layer thickness (mm) and 10-year average thickness of ice layers (mm). (a) The SIGMA-A ice core. (b) The SE-Dome I ice core and the SE-Dome II ice core.

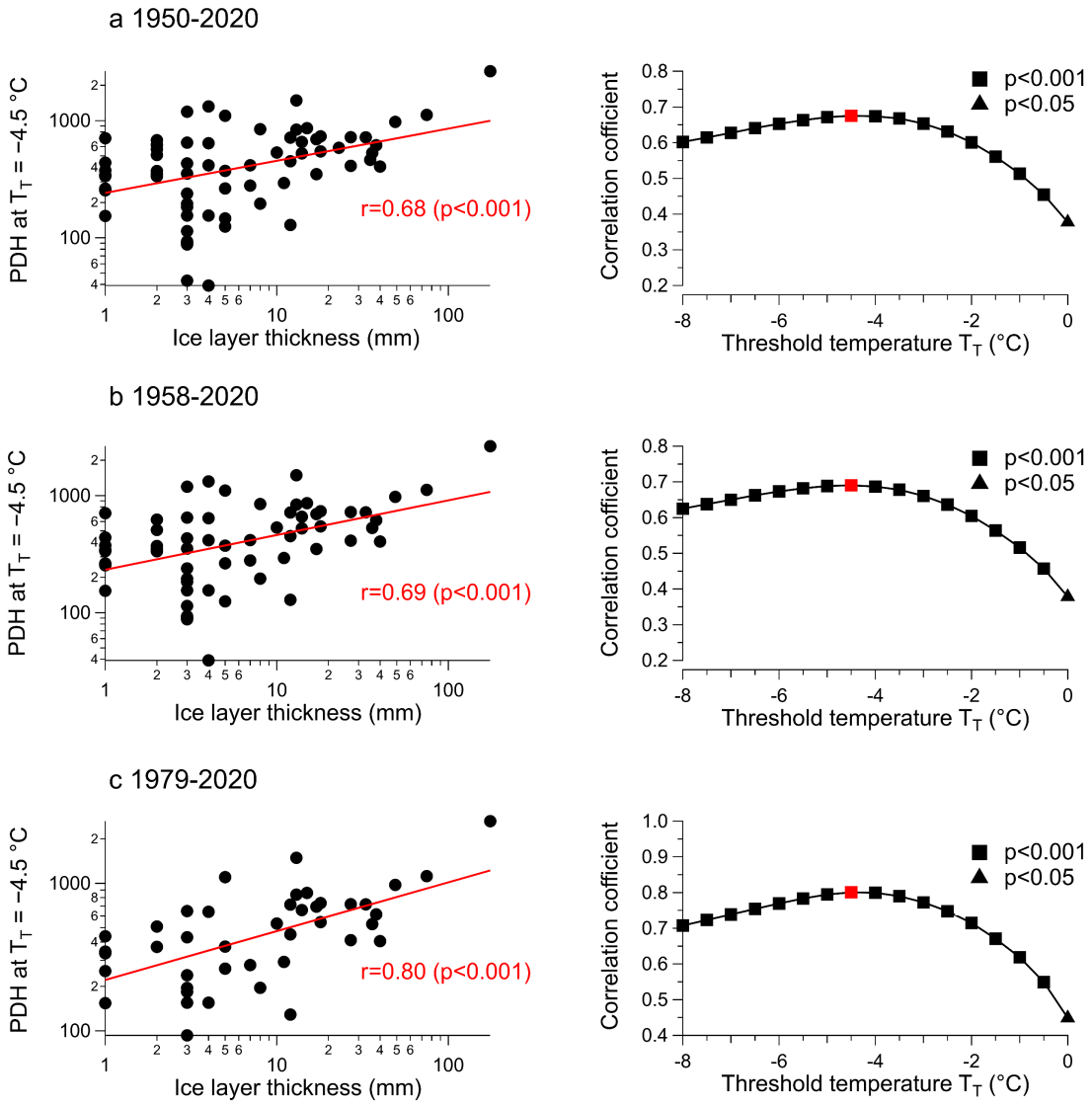

Figure 4-9 Scatter plot of the ice layer thickness and positive degree hour sum (PDH) with $T_T = -4.5$ °C (left) and the correlation coefficient between ice layer thickness and PDH (°C h) given by threshold temperature (T_T, °C) (right). (a) 1950–2020, (b) 1958–2020, (c) 1979–2020. Both ice layer thickness and PDH are presented by logarithmic scale.

4.2 Ion concentration of the SE-Dome II ice core

Figure 4-10 shows the ion concentrations of the SE-Dome II ice core: total ion concentration (μeq L^{-1}), H^+ concentration (total anion concentration minus total cation concentration) (μeq L^{-1}), major cation (Na^+, Ca^{2+}, NH_4^+) concentrations (μeq L^{-1}), major anion (Cl^-, NO_3^-, SO_4^{2-}) concentrations (μeq L^{-1}). Ion concentration profiles in Figure 4-10 are averaged over 10-year periods in Table 4-2. The average concentration of the entire SE-Dome II ice core is approximately one-fifth lower than that of the SIGMA-A ice core. The main ion species are NO_3^- and SO_4^{2-} in the SE-Dome II ice core (Table 4-2). In the table, SO_4^{2-} has high concentrations during 1950–1980s (average of 1.32 μeq L^{-1}; Table 4-2), a period when the emission of anthropogenic SO_4^{2-} was at a maximum (Fischer et al., 1998). The maximum concentration of Ca^{2+} is observed in 2003 (14.2 μeq L^{-1}), and the 10-year average has a high concentration during 2011–2020 (0.52 μeq L^{-1}; Table 4-2). The Ca^{2+} peak in 2003 was also observed in the SE-Dome I ice core (Amino et al., 2021). The dust emissions at the coastal region have been increasing due to a decreasing seasonal snow-cover area arising from coastal Greenland warming after 2000 (Saros et al., 2019; Amino et al., 2021). Thus, Ca^{2+} concentrations have increased in recent years. Na^+ and Cl^- concentrations have also increased since 2001 (average of 0.59 μeq L^{-1} and 0.66 μeq L^{-1}; Table 4-2), suggesting a high impurity contribution from sea salt in the north Atlantic (Curtis et al., 2018). For the NH_4^+ concentration, the 10-year average has a high concentration during 1931–1940. The high NH_4^+ concentration in this period is probably due to the deforestation in North America and Siberia in the early 1900s and also detected as a biomass peak during 1920–1940 in the Canadian ice core (Zennaro et al., 2014; Fischer et al., 2015).

For the ice layers (Table 4-2), the total ion concentration (3.29 μeq L^{-1}) is higher than in the entire SE-Dome II ice core (5.60 μeq L^{-1}). This suggests that ion concentrates during the refreezing process (e.g., Iizuka et al., 2002). H^+ concentration is also high in the ice layers, suggesting the acid deposits in the aquifer and concentrates in the ice layers during the refreezing process. Focused on the Mg^{2+}/Na^+ ratio, which is used as the proxy of melting, Mg^{2+}/Na^+ is 0.14 for the entire core and 0.20 for the ice layers (Table 4-2). The high Mg^{2+}/Na^+ ratio in the ice layer is likely due to the inflow of meltwater (e.g., Iizuka et al., 2002). In 2012 when extreme surface melting happened, about 70 cm of ice layers and layers with percolated ice was detected in the SE-Dome II ice core (section 4.1). Based on the seasonal time scale of the SE-Dome II ice core,

these melt features correspond to the winter to the summer in 2012. Thus, these melt features were formed by a large amount of meltwater that percolated and refrozen in the firn of the winter. Mg^{2+}/Na^{+} (0.14) in the average of melt features in 2012 is lower than the average value of ice layers but higher than the sea salt ratio (0.11), suggesting the meltwater flows in. On the other hand, SO_4^{2-} concentration in the 1950 ice layer (3.32 μeq L^{-1}; Table 4-2) is 3.5 times or twice higher than that in the entire ice core or the 2012 ice layer, which is probably due to the high anthropogenic sulfate in 1950. According to the SE-Dome II time scale, the 1950 ice layer corresponds to the spring. The Mg^{2+}/Na^{+} of the 1950 ice layer is 0.49, which is higher than the average of all ice layers and the 2012 ice layer. This suggests that the ice layer in 1950 was formed by initial meltwater refreezing without flowing out.

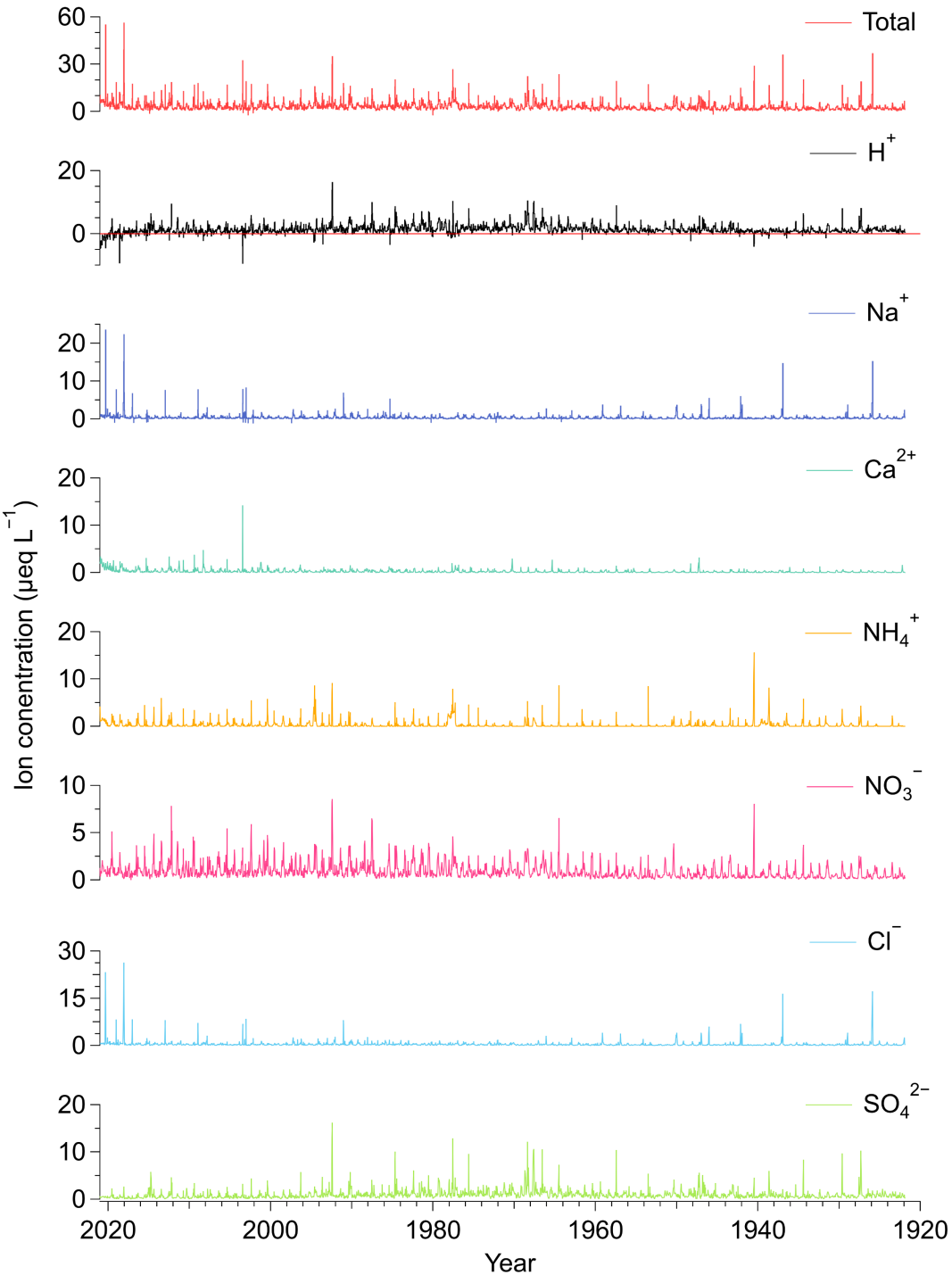

Figure 4-10 Ion concentration (μeq L^{-1}) of the SE-Dome II ice core from 1921 to 2020. Each concentration is total ion, H^+, Na^+, Ca^{2+}, NH_4^+, NO_3^-, Cl^-, and SO_4^{2-} concentration.

Table 4-2 The average of major ion concentrations (μeq L^{-1}) in the entire SE-Dome II ice core and ice layers (IL) during 1921–2020, and the 2012 ice layer (2012 IL) and the 1950 ice layer (1950 IL).

	Cl^-	SO_4^{2-}	NO_3^-	Na^+	NH_4^+	Mg^{2+}	Ca^{2+}	H^+	Mg^{2+}/Na^+	Total
2011–2020	0.82	0.59	1.05	0.72	0.41	0.03	0.52	0.68	0.07	4.22
2001–2010	0.46	0.58	1.04	0.43	0.30	0.02	0.39	0.93	0.10	3.23
1991–2000	0.47	0.89	1.25	0.40	0.44	0.02	0.29	1.44	0.12	3.78
1981–1990	0.43	1.13	1.19	0.36	0.22	0.01	0.25	1.90	0.10	3.61
1971–1980	0.39	1.33	1.01	0.30	0.43	0.01	0.22	1.77	0.12	3.69
1961–1970	0.32	1.56	1.01	0.25	0.23	0.01	0.21	2.19	0.19	3.59
1951–1960	0.29	0.91	0.63	0.26	0.10	0.01	0.13	1.33	0.15	2.34
1941–1950	0.43	1.01	0.59	0.38	0.21	0.02	0.16	1.26	0.19	2.82
1931–1940	0.32	0.75	0.55	0.28	0.45	0.02	0.11	0.77	0.17	2.48
1921–1930	0.48	0.88	0.49	0.41	0.17	0.03	0.12	1.12	0.18	2.58
Core average	0.45	0.95	0.90	0.39	0.31	0.02	0.25	1.33	0.14	3.29
IL average	0.45	1.34	2.30	0.24	0.93	0.06	0.47	2.47	0.20	5.62
2012 IL	0.74	1.64	2.65	0.43	1.20	0.06	1.07	1.83	0.14	7.58
1950 IL	0.54	3.32	3.16	0.11	1.97	0.06	0.58	4.31	0.49	9.74

4.3 Shape and chemical components of inclusions in the ice layers of the SE-Dome II ice core

4.3.1 Microscope observation and Raman results

Inclusion measurements in ice layers of the SIGMA-A ice core showed that the inclusions greater than 30 μm in diameter are formed by refreezing meltwater (section 3.3). The larger rod-like inclusions are formed at the last region to freeze with a large amount of meltwater of Na^+ and Cl^-. This section describes the characteristics of the inclusions in the ice layers of the SE-Dome II ice core and discusses the differences from the inclusions in the ice layers of the SIGMA-A ice core.

Table 4-3 shows the results from microscope observation and Raman analyses with the 2012 ice layer of the SE-Dome II ice core. 12 inclusions were detected, which were classified into three types, similar to the inclusions in the SIGMA-A ice layer. Eight were particle-like, three were rod-like, and one was columnar-like (Table 4-3). Almost all measurement of the 12 inclusions showed no Raman peaks, and only one measurement detected $CaSO_4 \cdot 2H_2O$ in rod-like inclusion.

Table 4-3 The number of 982, 984, 990, 1008 (cm^{-1}) and other peaks detected from three types of inclusions in the 2012 ice layer of the SE-Dome II ice core. The peaks at 982, 984, 990, and 1008 (cm^{-1}) indicate liquid $(NH_4)_2SO_4$, liquid H_2SO_4, solid $Na_2SO_4 \cdot 10H_2O$, and solid $CaSO_4 \cdot 2H_2O$.

	982 (cm^{-1})	984 (cm^{-1})	990 (cm^{-1})	1008 (cm^{-1})	Other peaks	Total peaks	No peaks	Total measurements
Particle	0	0	0	0	0	0	8	8
Rod	0	0	0	1	0	1	2	3
Columnar	0	0	0	0	0	0	1	1
Total	0	0	0	1	0	1	11	12

4.3.2 Shape and elemental components of nonvolatile inclusions in ice layers

The detected nonvolatile inclusions in the 2012 and 1950 ice layers extracted by the sublimation were 205, and were classified into three types: particle-like (176 inclusions with an average of 9.4 μm in diameter), rod-like (19 inclusions with an average of 105.6 μm in diameter), and columnar-like (10 inclusions with an average of 28.5 μm in diameter) (Figure 4-11). For particle-like inclusions, 8% are greater than 30 μm in diameter (dark blue bar in Fig. 4-11). For rod-like inclusions, this percentage is 53% (red bar in Fig. 4-11), whereas, for columnar-like inclusions, the percentage is 20% (dark green bar in Fig. 4-11). Inclusions greater than 30 μm in diameter in the ice layers were detected in both the SIGMA-A ice core and the SE- Dome II ice core. Most rod-like inclusions are over 30 μm in diameter, and the average diameter tended to be four times greater than that of other inclusions.

The elemental analyses of the nonvolatile inclusions in the ice-layer samples are shown in Fig. 4-11. Inclusions were classified into 12 categories based on their constituent elements of Na, Ca, S, and Cl, which are associated with Na^+, Ca^{2+}, SO_4^{2-}, and Cl^- species (see section 3.3.2). For the particle-like inclusions, 31% are classified as 'Others' (grey; in Fig. 4-12a), 24% are as 'only S or Cl' (light purple; in Fig. 4-12a), and 22% are 'Na∩Ca∩S' (blue; in Fig. 4-12a). For the rod-like inclusions, 32% are classified as 'Na∩Ca∩S∩Cl' (dark blue; in Fig. 4-12b), 26% are as 'only S or Cl' (light purple; in Fig. 4-12b), and 21% are 'Na∩Ca∩S' (blue; in Fig. 4-12b). For the columnar-like inclusions, 30% are classified as 'Na∩Ca∩S' (blue; in Fig. 4-12c), 30% are as 'only S or Cl' (light purple; in Fig. 4-12c), and 20% are 'Ca∩S∩Cl' (pink; in Fig. 4-12c).

4.4 Chemical form and shape of inclusions in the ice layers formed in 2012 and 1950 of the SE-Dome II ice core

As described in section 3.3, particle-like inclusions in ice grains and grain boundaries contain solid salts of $Na_2SO_4 \cdot 10H_2O$ and $CaSO_4 \cdot 2H_2O$, as well as brine with NH_4^+ and SO_4^{2-}. Rod-like inclusions in grain boundaries contain brine with SO_4^{2-}, Cl^-, Na^+, and NH_4^+. Columnar-like inclusions within ice grains consist of $CaSO_4 \cdot 2H_2O$ (gypsum). Based on the above, in this section, the chemical compositions of the inclusions in the 2012 and the 1950 ice layers of the SE-Dome II ice core are considered. Fig. 4-12c shows 60% of the columnar-like inclusions contain both Ca and S. In the ice layers of the SIGMA-A ice core, the columnar-like inclusions contain solid gypsum salts ($CaSO_4 \cdot 2H_2O$). Thus, the columnar-like inclusions in the SE-Dome II ice core probably consist of solid $CaSO_4$. The most common signal in the particle type is 'Others' (grey; 31% in Fig. 4-12a). Most of the 'Others' inclusions contain Si without Na, Ca, S, and Cl, suggesting that the particle-like inclusions mainly consist of mineral dust (see section 3.3). According to the SIGMA-A results, the 'only S' inclusions may be NH_4^+ and SO_4^{2-} as liquid brine. In contrast, the 'Na∩Ca∩S' inclusions are considered to be salt mixtures of Na_2SO_4, and $CaSO_4$. Thus, the particle-like inclusions contain various solid salts of Na_2SO_4 and $CaSO_4$, as well as brines of NH_4^+ and SO_4^{2-}. As described above, the main elemental combinations of the rod-like inclusions in the ice layers of the SE-Dome II core are 'Na∩Ca∩S∩Cl' (32%), 'only S or Cl' (26%), and 'Na∩Ca∩S' (21%). The rod-like inclusions classified as 'only S or Cl' can be further divided into 'Only S' (16%) and 'only Cl' (10%). The rod-like inclusions are most likely to be derived from Na^+, Ca^{2+}, SO_4^{2-}, and Cl^-, which are detected as Na, S, Ca, and Cl by EDS analysis, respectively. If Na^+ and Ca^{2+} concentrations are higher than SO_4^{2-}, the salts are formed. However, the meltwater that forms ice layers contains much SO_4^{2-} (1.34 μeq L^{-1}) with a few Cl^- (0.45 μeq L^{-1}), Na^+ (0.24 μeq L^{-1}), and Ca^{2+} (0.47 μeq L^{-1}). In addition, a possible chemical form of the rod-like inclusions in the SIGMA-A ice core is a brine of SO_4^{2-}, Cl^-, Na^+, and NH_4^+. Thus, it is considered that the rod-like inclusions in the SE-Dome II ice core contain Na^+, Ca^{2+}, SO_4^{2-}, NH_4^+, and Cl^-.

The rod-like inclusions in the SIGMA-A ice core contain mainly 'Na∩Ca∩S∩Cl' (45%), 'Na∩Cl' (11%), and 'Na∩S∩Cl' (8%) (section 3.3). Thus, 64% of the rod-like inclusions in the SIGMA-A ice core contain both Na and Cl. In contrast, the rod-like inclusions in the SE-Dome II

ice core contain ‘Na∩Ca∩S∩Cl’ (32%), ‘Na∩Ca∩S’ (21%), and ‘Only S’ (16%), suggesting that 69% of rod-like inclusions contain S. These results suggest that the rod-like inclusions of the SIGMA-A ice core contain much more Na and Cl, whereas those of the SE-Dome II ice core contain much more S.

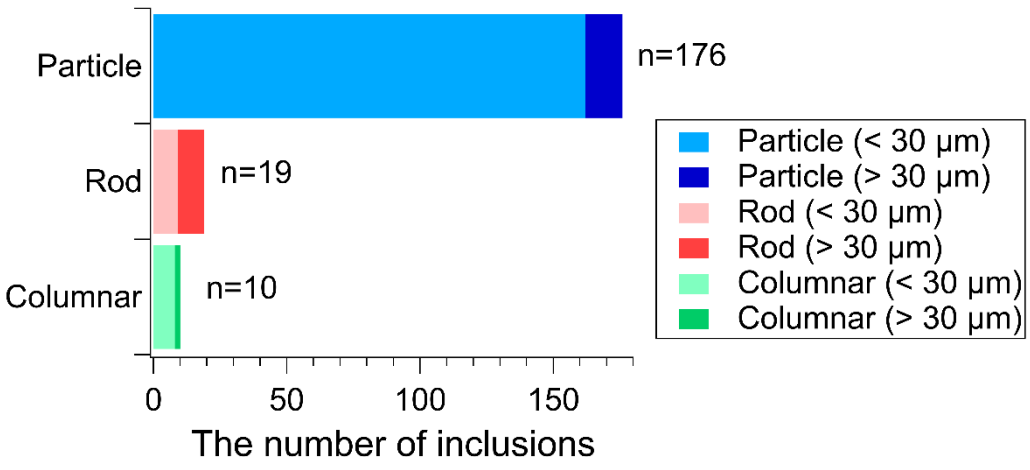

Figure 4-11. The number of each type of nonvolatile inclusion from the 2012 and 1950 ice layers of the SE-Dome II ice core detected by SEM.

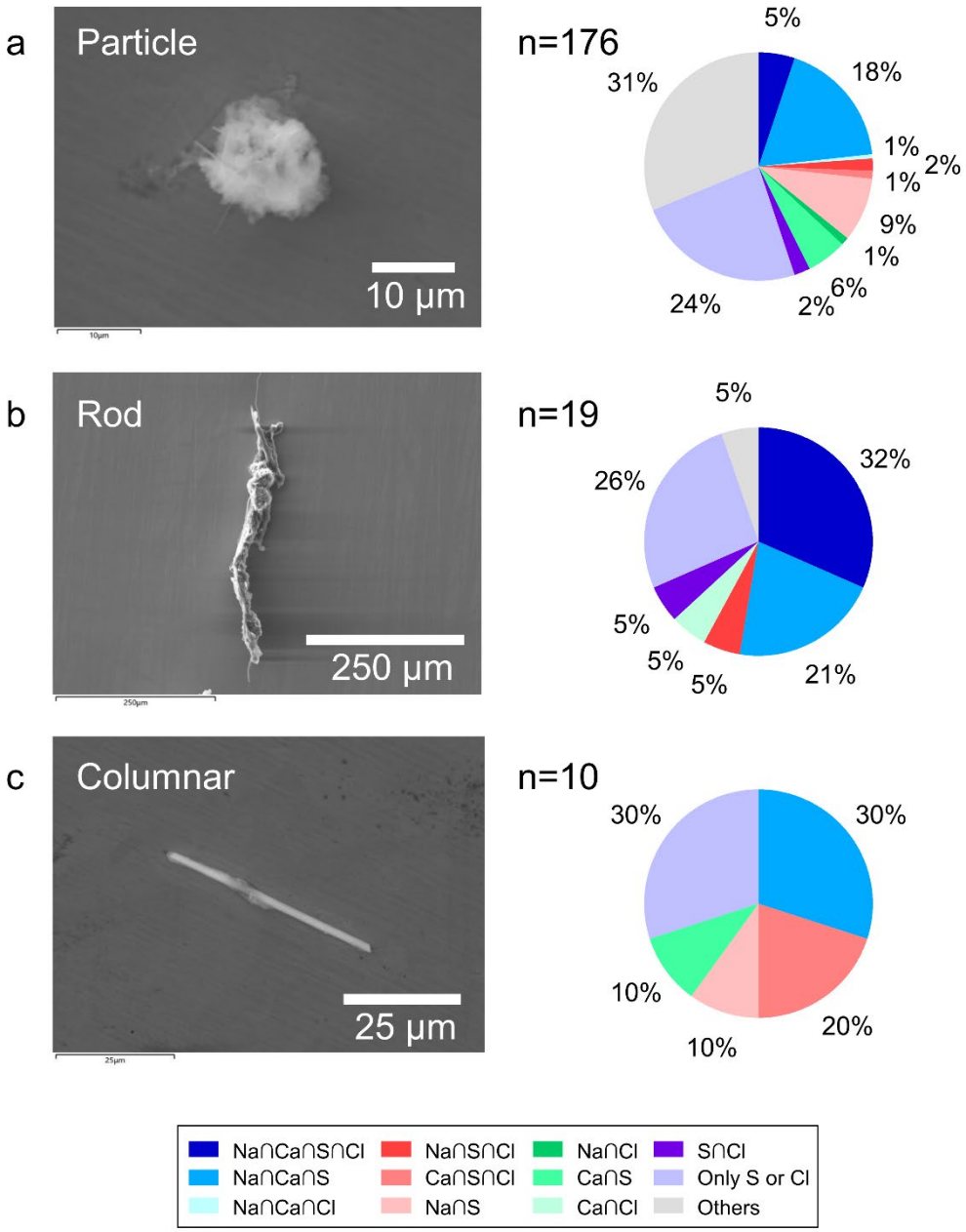

Figure 4-12 Microphotograph of inclusions and elemental compositions by SEM-EDS analyses. (a) Particle-like inclusion from the 1950 ice layer and composition of 176 particle-like inclusions from EDS analyses. (b) Rod-like inclusion from the 1950 ice layer and composition of 19 rod-like inclusions. (c) Columnar-like inclusion from the 2012 ice layer and composition of 10 columnar-like inclusions.

5 Proposed formation mechanism of inclusions and a new proxy for the amount of chemical deposition and melting

5.1 Formation mechanism of inclusions during the refreezing processes

In the ice layers of the SIGMA-A ice core and the SE-Dome II ice core, the inclusions of three different types were commonly detected. However, differences in the chemical compositions of rod-like inclusions were observed. In Figure 5-1, a formation mechanism of inclusions during refreezing processes is proposed. Previous studies (e.g., Halde, 1980; Takenaka et al., 1996; Bartels-Rausch et al., 2014) suggest that ionic materials in water concentrate in the liquid phase during freezing as ice rejects impurities upon freezing, with a tendency to collect in the triple junctions in the last region of freezing. In contrast, in this study, columnar- and particle-like inclusions of solid $Na_2SO_4 \cdot 10H_2O$ and $CaSO_4 \cdot 2H_2O$ are detected within the ice grains. The Na_2SO_4 and $CaSO_4$, having eutectic temperatures of −1.3 and −0.05 °C, are likely to exist as solid salts. Thus, columnar- and particle-like inclusions of solid $Na_2SO_4 \cdot 10H_2O$ and $CaSO_4 \cdot 2H_2O$ are considered to form first, within the ice grains (Figure 5-1 (a), (b)). As freezing progresses, particle-like inclusions of brines with Na^+, Cl^-, NH_4^+, and SO_4^{2-} form in grain boundaries (Figure 5-1 (c)). Then the brine is more concentrated and preserved as rod-like inclusions along the resulting grain boundary. If sufficient amount of impurity exists in the meltwater, large rod-like inclusions of brines form at grain boundaries (Figure 5-1 (d)). In considering the ice grains that form the ice layers, the grain boundaries are planar whereas the triple junctions are linear. Rod-like inclusions are detected as a linear shape, indicating that they are formed at the triple junctions.

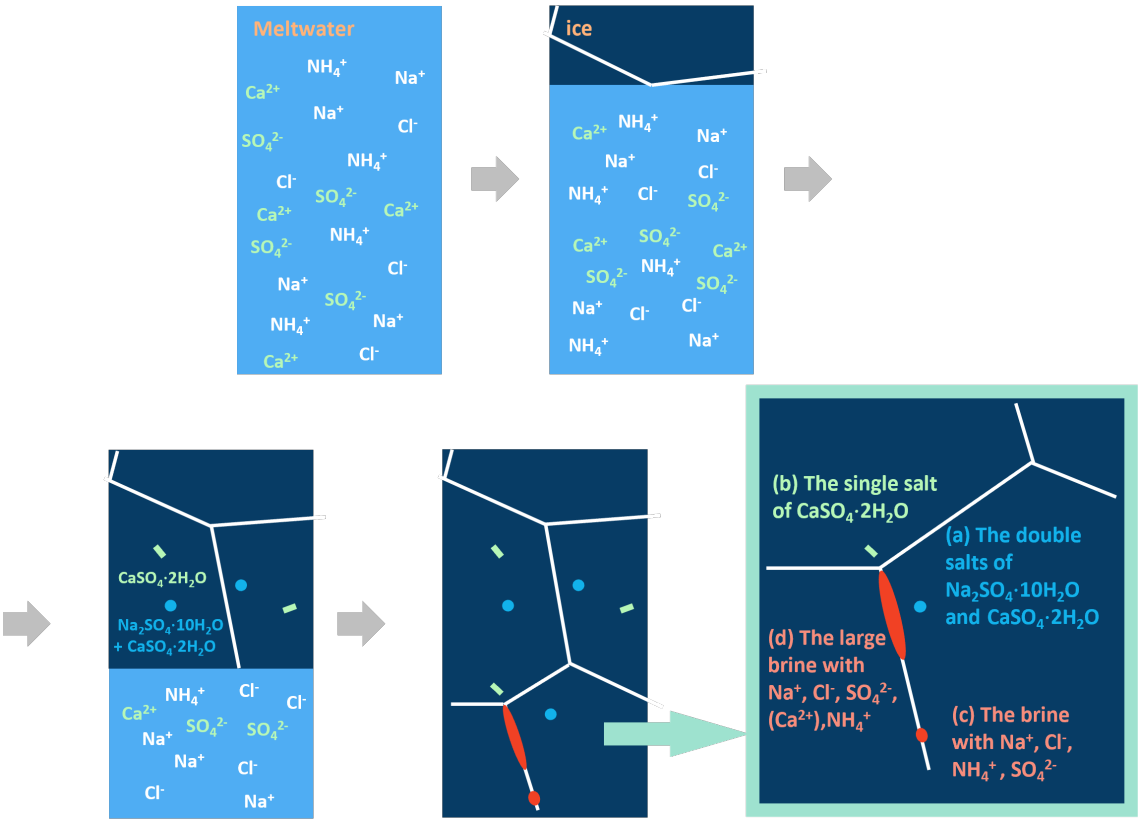

Figure 5-1 Proposed formation mechanism of inclusions in the ice layers. The sequence of inclusion formation is summarized in the last (green-framed) drawing. White lines are grain boundaries or triple junctions.

5.2 The rod-like inclusions as a new proxy for the amount of chemical deposition and melting

The rod-like inclusions greater than 100 μm in diameter were detected in the 2012 and 2006 ice layers of the SIGMA-A ice core, and in the 2012 and 1950 ice layers of the SE-Dome II ice core. However, the chemical compositions of rod-like inclusions are different in the two ice cores. The 64% of rod-like inclusions in the SIGMA-A ice core contain both Na and Cl. In contrast, the 69% of rod-like inclusions in the SE-Dome II ice core contain S. The difference in the chemical compositions of rod-like inclusions is considered due to the ionic species and ion balance of the meltwater that forms the ice layer. Then, the ion ratios of Na^+, Ca^{2+}, SO_4^{2-}, and Cl^- in the ice layers formed in 2012 and 2006 of the SIGMA-A ice core, and that in the ice layers formed in 2012 and 1950 of the SE-Dome II ice core, were calculated (Figure 5-2). Figure 5-2 also shows the mole ratios of the four elements Na, S, Cl, and Ca detected by EDS analyses in all inclusions greater than 100 μm in diameter, mainly rod-like inclusions. In the SIGMA-A ice core (Figure 5-2a, b), the total proportions of Na^+ and Cl^- in the ice layer are almost half (55.6% in the 2012 ice layer and 46.1% in the 2006 ice layer), and the total proportions of Na and Cl in the rod-like inclusions are high (89.5% in the 2012 ice layer and 58.1% in the 2006 ice layer). In the SE-Dome II ice core (Figure 5-2c, d), the proportions of SO_4^{2-} are highest in both ice layers (43.6% in the 2012 ice layer and 73.0% in the 1950 ice layer), and the proportions of S are also high in the rod-like inclusions (31.3% in the 2012 ice layer and 67.6% in the 1950 ice layer). The total proportions of Ca^{2+} and SO_4^{2-} are 44.4% in the 2012 ice layer of the SIGMA-A ice core, 54.0% in the 2006 ice layer of the SIGMA-A ice core, 69.9% in the 2012 ice layer of the SE-Dome II ice core, and 85.7% in the 2006 ice layer of the SE-Dome II ice core. The total proportions of Ca and S in the rod-like inclusions are 10.4% in the 2012 ice layer of the SIGMA- A ice core, 41.9% in the 2006 ice layer of the SIGMA-A ice core, 52.9% in the 2012 ice layer of the SE-Dome II ice core, and 79.8% in the 1950 ice layer of the SE-Dome II ice core. These results suggest that the proportions of Ca and S in the rod-like inclusion are less than those of Ca^{2+} and SO_4^{2-} in the ice layers. However, each proportion of Ca and S in the rod-like inclusions of the ice layer reflects each proportion of Ca^{2+} and SO_4^{2-} in the ice layer. The decrease of Ca and S is due to that the gypsum ($CaSO_4 \cdot 2H_2O$) is firstly formed in ice grains and less Ca and S remain in the rod-like inclusions (see section 5.1). Regardless of this distribution, however, the molar ratios of rod-like inclusions in both SIGMA-A ice core and SE-Dome II ice core reflect the ionic ratios of the ice layers. In other words, the chemical composition of the rod-like inclusions reflects the chemical

composition of the meltwater that forms the ice layers.

Na^+ and Cl^- originate from sea salt, peaking in winter to early spring (e.g., Kuramoto et al., 2011). Compared ionic ratios of ice layers from the SIGMA-A ice core to those from the SE-Dome II ice core, the ice layers of the SIGMA-A ice core contain much more Na^+ and Cl^-. Since the SIGMA-A site is located to be closer to the coast and at a lower elevation than SE-Dome site, high contribution of sea salt to the total ion concentrations is excepted. It indicates that the chemical composition of rod-like inclusions in ice layers reflects the relative amount of inclusions depositing to the drilling site.

In the SIGMA-A ice core, the 2012 ice layer has a higher Na^+ and Cl^- ratio (55.6%) than that in the 2006 ice layer (46.1%). The annual layer thickness in 2012 is 0.60 m while the ice layer thickness in 2012 is 0.76 m, indicating that the ice layer thickness exceeds the annual layer thickness (Table 5). In contrast, in 2006, the annual layer thickness was 0.39 m and the ice layer thickness was 0.20 m, and thus the ice layer thickness did not exceed the annual layer thickness (Table 5). These results suggest that the amount of melting is larger in 2012 than in 2006. Since the 2012 ice layer include the layer corresponding to winter, the 2012 ice layer has a higher Na^+ and Cl^- than those in 2006. Thus, the chemical composition of rod-like inclusions reflects differences in ion ratios due to the amount of melting.

In the SE-Dome II ice core, each ice layer thickness does not exceed the annual layer thickness in common (Table 5). However, the ratio of SO_4^{2-} in the 1950 ice layer (73.0%) is higher than that in the 2012 ice layer (43.6%). This is probably due to that 1950 corresponds to a period when more anthropogenic sulfate deposits on the ice sheet than in 2012, as discussed in Section 4.2. Therefore, the chemical composition of the rod-like inclusions may reflect the ionic ratios at the time the ice layer is formed.

In summary, the chemical composition of rod-like inclusions in the ice layer reflects the difference in ionic ratios depending on the location of ice core drilling, the amount of melting, and the age when the ice layer is formed. In other words, the chemical composition of rod-like inclusions in the ice layer reflects differences the amount of deposition of chemical substances and the amount of melting (Figure 5-3). The rod-like inclusion is a new proxy for the chemical composition of the meltwater that forms the ice layer.

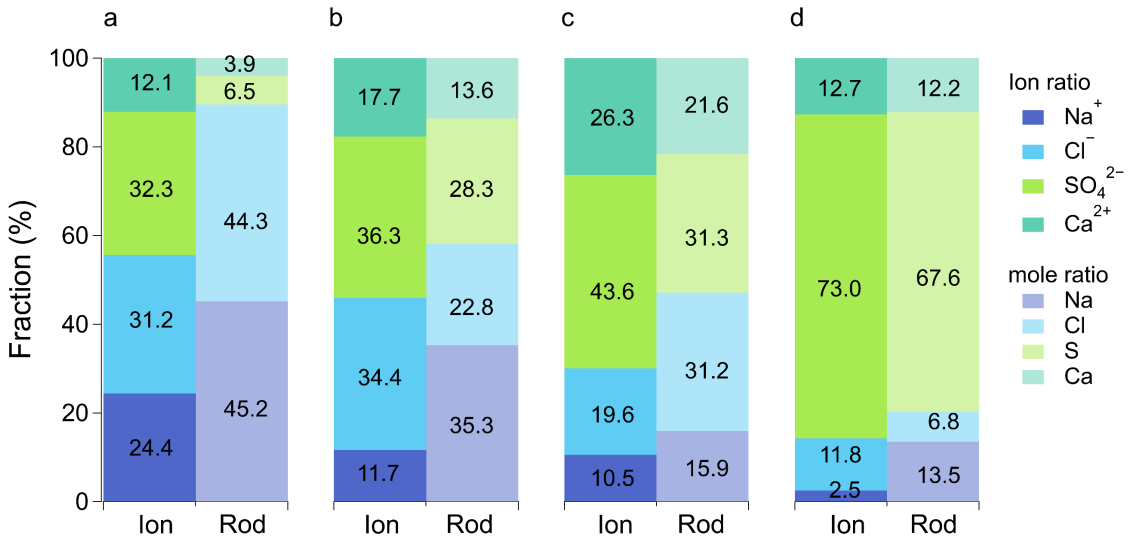

Figure 5-2 The comparison between the ion ratio in the ice layer and mole ratio of element composition in the rod-like inclusion. (a) The 2012 ice layer of the SIGMA-A ice core. (b) The 2006 ice layer of the SIGMA-A ice core. (c) The 2012 ice layer of the SE-Dome II ice core. (d) The 1950 ice layer of the SE-Dome II ice core.

Table 5 The annual layer thickness (m) and ice layer thickness (m) of the SIGMA-A ice core and the SE-Dome II ice core.

	SIGMA-A ice core		SE-Dome II ice core	
Year	2012	2006	2012	1950
Annual layer thickness (m)	0.60	0.39	0.99	0.67
Ice layer thickness (m)	0.76	0.20	0.17	0.33

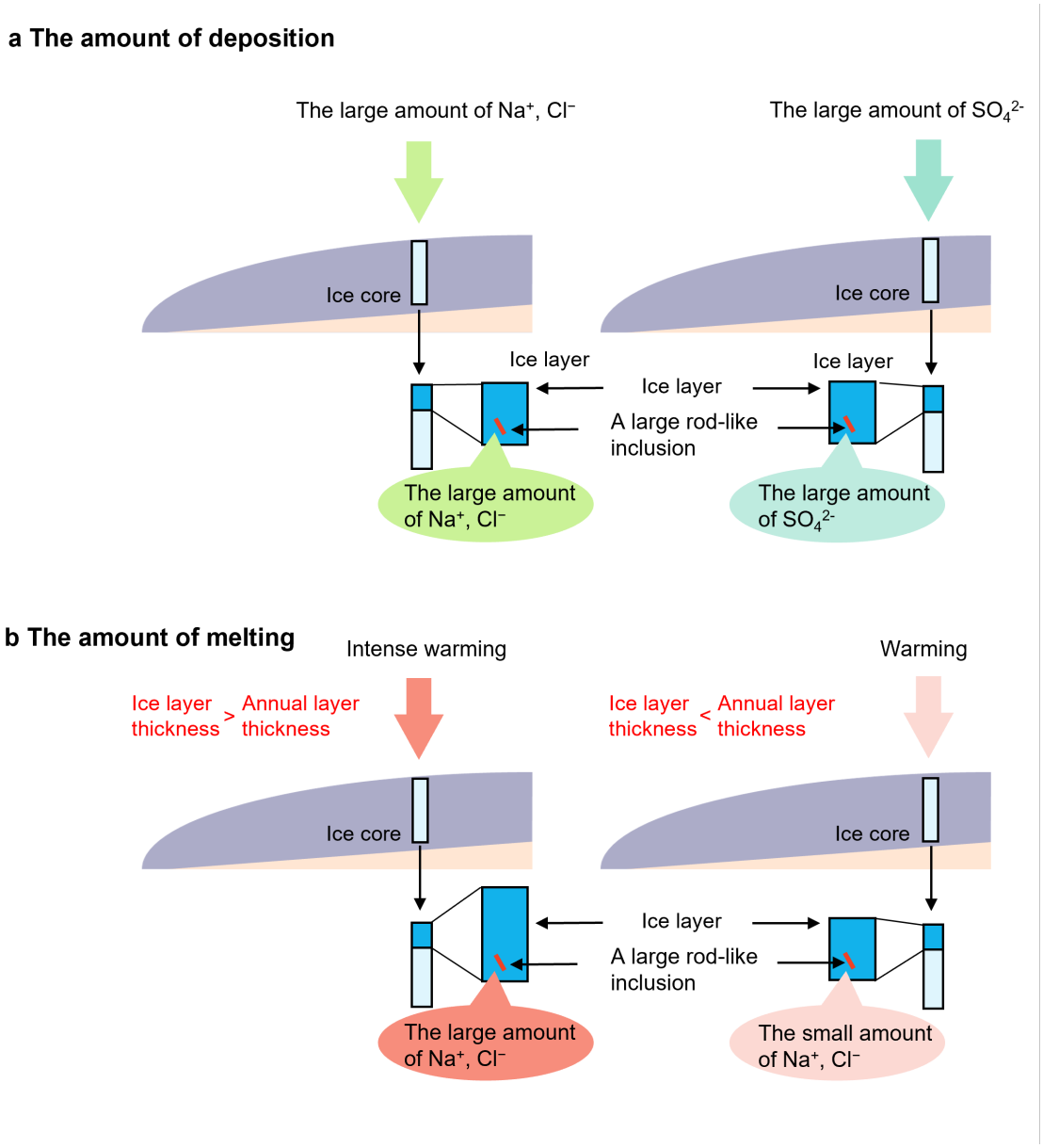

Figure 5-3 The factors of the chemical compositions in a rod-like inclusion as a new proxy. (a) The amount of deposition. (b) The amount of melting.

In the Greenland ice sheet, not only shallow cores such as the SIGMA-A ice core and the SE-Dome II ice core, which are 10–100 m order in long, but also deep cores, which are several thousand meters long, have been drilled. The NEEM ice core, for example, is about 2500 m in depth and dates back to the last interglacial (about 130,000 years ago) (NEEM project members, 2013). The Last Interglacial is estimated to have been warmer than today (Schüpbach et al., 2018), and surface melting may have occurred in the Greenland ice sheet at that time. However, air bubbles inside the ice at the deeper part of the ice core change to hydrate clathrate. Then, it is difficult to detect the ice layers formed 130,000 years ago by visual observation, and thus the surface melting history has not been reconstructed.

As an application of this study, if a rod-like inclusion is detected in the ice at a depth corresponding to the Last Interglacial, it can provide an indication that a melting event occurred at that depth. Furthermore, the ionic ratio in the meltwater can be reconstructed by investigating the chemical composition of the rod-like inclusion. The rod-like inclusion may be a proxy such as the amount of chemical deposition and melting.

The number and thickness of ice layers in the SIGMA-A ice core and the SE-Dome II ice core have increased with recent warming. It is estimated that the Earth's surface temperature will increase in the future (IPCC AR6, 2021), leading to an environment that facilitates the formation of thicker ice layers. This implies that rod-like inclusion will likely increase in expand regions and at more ages, making rod-like inclusions an important proxy in environmental reconstructions with future ice cores.

6 Summary

This chapter summarizes the main results of this study. With the SIGMA-A ice core drilled in northwestern Greenland and the SE-Dome II ice core in southeastern Greenland, the melting histories were reconstructed by the number and thickness of ice layers. Using a combination of microscopy and spectroscopy, the size, shape, location, and chemical compositions of inclusions in ice layers were investigated. This study clarified the time series of the number and thickness of ice layers in different regions of Greenland. In addition, this study found unique inclusions in ice layers formed by melting and refreezing processes and proposed a new proxy that indicates melting and ion balances in the meltwater.

There are 243 observed ice layers greater than 1 mm in thickness with an average thickness of 14 mm in the SIGMA-A ice core and 89 ice layers greater than 1 mm in thickness with an average thickness of 10 mm in the SE-Dome II ice core. The number and the thickness of ice layers in both ice cores have dramatically increased since 1995 as Arctic warming. A significant positive correlation is found between ice layer thickness of the SE-Dome II ice core and summer air temperature at the SE-Dome site extracted from the ERA5 reanalysis data from 1950 to 2020. Exceptionally thick ice layers in 1889 and 1927 were found, indicating extensive melt events in the period when the reanalysis data do not cover. The extreme melting event on the inland Greenland ice sheet in 1889 is widely observed in the precious ice core studies. The thick ice layer in 1927 occurred during the warming in the 1920s. The frequency of ice layers had increased since 1845, suggesting the Little Ice Age may ended up in 1845 in the SE-Dome region. These results suggest that the thickness of ice layers may provide the warm summer temperatures.

The size, shape, location, and chemical composition of inclusions were examined in ice layers formed by melt-refreezing in the SIGMA-A ice core and the SE-Dome II ice core. In the ice layers, three types of inclusions were commonly identified: 1) Particle-like inclusions in ice grains and grain boundaries that contain solid salts of $Na_2SO_4 \cdot 10H_2O$ and $CaSO_4 \cdot 2H_2O$, as well as brine with NH_4^+ and SO_4^{2-}. 2) Columnar-like inclusions within ice grains that consist of $CaSO_4 \cdot 2H_2O$ (gypsum). 3) Rod-like inclusions in the triple junctions that contain brine with SO_4^{2-}, Cl^-, Na^+, Ca^{2+} or NH_4^+. The inclusions over 30 μm in diameter were formed by melt-refreezing. Rod-like inclusions are larger than other inclusions, and up to about 1 mm in diameter. From the location and eutectic temperature of each inclusion, the processes are proposed as the following sequence. 1) First, the smaller columnar- and particle-like inclusions of solid $Na_2SO_4 \cdot 10H_2O$ and

$CaSO_4 \cdot 2H_2O$ form within the ice grains. 2) Then, particle-like inclusions of brines with SO_4^{2-}, Cl^-, Na^+, and NH_4^+ form in grain boundaries. And finally, in the case that the meltwater has sufficient impurity, then 3), large rod-like inclusions of brines form in the triple junction as the final product.

In the ice layers of the SIGMA-A ice core and the SE-Dome II ice core, large rod-like inclusions with 100–1000 μm order in diameter were commonly detected. However, the chemical composition of rod-like inclusions is different between the two ice cores. The rod-like inclusions of the SIGMA-A ice core contain much more Na and Cl, whereas those of the SE-Dome II ice core contain much more S. Then, the differences in the composition of rod-like inclusions are found to be due to the differences in ionic species and ion balance of the meltwater that forms the ice layer. Compared ionic ratios of ice layers and mole ratios of rod-like inclusions, the chemical composition of rod-like inclusions in the ice layer reflects differences in ionic ratios depending on the amount of chemical deposition and the amount of melting. The large rod-like inclusions are suggested to be a proxy that the ice was formed by meltwater refreezing. Furthermore, the ionic ratio in the meltwater can be reconstructed by investigating the chemical composition of the rod-like inclusions. Such a proxy may help identify past warm climates in deeper ice cores in Greenland. In addition, rod-like inclusions will likely increase in expand regions and at more ages, making rod-like inclusions an important proxy in environmental reconstructions with future ice cores.

7 Acknowledgement

I would like to express my deepest appreciation to Dr. Yoshinori Iizuka, Associate Professor of the Institute of Low Temperature Science (ILTS), Hokkaido University, for providing me with continuous guidance and encouragement throughout my master and doctoral courses, and the opportunity for joining SE-Dome II ice core drilling project in 2021.

I gratefully acknowledge Dr. Tsutomu Watanabe, professor of ILTS, Dr. Shin Sugiyama, professor of ILTS, Dr. Hideaki Motoyama, professor of National Institute of Polar Research (NIPR), who are the vice-examiners of this thesis for valuable comments.

I am extremely grateful to Dr. Sumito Matoba, Assistant professor of ILTS, for supporting me in the field activities, and for helpful advice and comments throughout my master and doctoral courses. I also grateful to Dr. Masahiro Minowa, Assistant professor of ILTS, for supporting in the field activities and providing ice sheet thickness data, and Mr. Tetsuhide Yamasaki for his great support throughout the field activities. I also thank to all members of the SE-Dome II ice core project and the SIGMA-A ice core project.

I also would like to cordially thank Dr. Akira Hori, Associate Professor of KITAMI Institute of Technology, for kindly providing the high-resolution density data of the SE-Dome II ice core. I also would like to thank Dr. Koji Fujita, Professor of Nagoya University, for providing the ERA5 reanalysis data and valuable comments. I am deeply grateful Professor Ryu Uemura of the Nagoya University for his helpful advice and comments. I wish to thank to Dr. Motohiro Hirabayashi of NIPR for providing tritium data. I am grateful to Professor Shuji Fujita of NIPR, Professor Kenji Kawamura of NIPR for their helpful advice and comments. I express my cordial thanks to Dr. Sakiko Ishino, Assistant Professor of the Institute of Nature and Environmental Technology, Kanazawa University, for teaching me the H_2O_2 measurements and providing me with valuable comments. I would like to thank to Shohei Hattori, Associate Professor of Nanjing University for his helpful comments. I also would like to thank Mr. Yutaka Kurosaki for providing the initial data of the SIGMA-A ice core.

I would like to thank Mr. Takeshi Saito of ILTS for supporting ice core processing in the cold room, and Ms. Ayako Kakugo of ILTS for helping me in my research life. Many thanks to all members of the Glacier and Ice sheet Research Group of ILTS. I am very grateful to Ms. Mutsumi Iizuka and Mr. Ken Kondo for their big support throughout my research and daily life.

Finally, I would like to express my appreciation to my family and friends.

8 References

Abbott, P. M., & Davies, S. M. (2012). Volcanism and the Greenland ice-cores: the tephra record. *Earth-Science Reviews*, 115(3), 173–191.

Aizawa, T., Ishii, M., Oshima, N., Yukimoto, S., & Hasumi, H. (2021). Arctic warming and associated sea ice reduction in the early 20th century induced by natural forcings in MRI-ESM2.0 climate simulations and multimodel analyses. *Geophysical Research Letters*, 48, e2020GL092336. https://doi.org/10.1029/2020GL092336

Aizawa, T., Oshima, N., & Yukimoto, S. (2022). Contributions of anthropogenic aerosol forcing and multidecadal internal variability to mid-20th century Arctic cooling CMIP6/DAMIP multimodel analysis. *Geophysical Research Letters*, 49, e2021GL097093. https://doi.org/10.1029/2021GL097093

Alley, R. B., Mayewski, P. A., Sowers, T., Stuiver, M., Taylor, K. C., Clark, P. U. (1997). Holocene climatic instability: A prominent, widespread event 8200 yr ago. *Geology*, 25(6), 483–486.

AMAP (2017). Snow, Water, Ice and Permafrost in the Arctic (SWIPA) 2017. Arctic Monitoring and Assessment Programme (AMAP), Oslo, Norway. xiv + 269 pp.

Amino, T., Iizuka, Y., Matoba, S., Shimada, R., Oshima, N., Suzuki, T., Ando, T., Aoki, T., & Fujita, K. (2021). Annual and seasonal dust fluxes during 1960-2014 from a southeastern dome in Greenland. *Polar Science*, 100599. doi:10.1016/j.polar.2020.100599

Anklin, M., Bales, R.C., Mosley-Thompson, E., & Steffen, K. (1998). Annual accumulation at two sites in northwest Greenland during recent centuries. *Journal of Geophysical Research: Atmospheres*, 103(D22), 28775–28783. https://doi.org/10.1029/98JD02718

Aoki, T., Matoba, S., Uetake, J., Takeuchi, N., & Motoyama, H. (2014). Field activities of the 'snow impurity and glacial microbe effects on abrupt warming in the Arctic' (SIGMA) project in Greenland in 2011–2013. *Bulletin of Glaciological Research*, 32, 3–20. doi:10.5331/bgr.32.3

Ashmore, D.W., Mair, D.W.F., & Burgess, D.O. (2019). Meltwater percolation, impermeable layer formation and runoff buffering on Devon Ice Cap, Canada. *Journal of Glaciology*, 66(255), 61–73. doi:10.1017/jog.2019.80

Avak, S. E., Trachsel, J. C., Edebeli, J., Brütsch, S., Bartels-Rausch, T., Schneebeli, M., et al. (2019). Melt-induced fractionation of major ions and trace elements in an Alpine snowpack. *Journal of Geophysical Research: Earth Surface*, 124, 1647– 1657. https://doi.org/10.1029/2019JF005026

Baker, I., Cullen, D., & Iliescu, D. (2003). The microstructural location of impurities in ice. *Canadian Journal of Physics*, 81(1-2), 1–9. doi:10.1139/p03-030

Balascio, N. L., D'Andrea, W. J., Bradley, R. S., & Perren, B. B. (2013). Biogeochemical evidence for hydrologic changes during the Holocene in a lake sediment record from southeast Greenland. *The Holocene*, *23*(10), 1428–1439.

Bales, R.C., Sommerfeld, R.A., & Kebler, D.G. (1990). Ionic tracer movement through a Wyoming snowpack. *Atmospheric Environment, Part A: General Topics*, 24(11), 2749–2758. doi:10.1016/0960-1686(90)90162-G

Bales, R. C., Guo, Q., Shen, D., McConnell, J. R., Du, G., Burkhart, J. F., Spikes, V. B., Hanna, E., & Cappelen, J. (2009). Annual accumulation for Greenland updated using ice core data developed during 2000 – 2006 and analysis of daily coastal meteorological data, *Journal of Geophysical Research*, 114, D06116, doi:10.1029/2008JD011208

Bartels-Rausch, T., Jacobi, H.W., Kahan, T. F., Thomas, J. L., Thomson, E. S., Abbatt, J. P. D., et al. (2014). A review of air–ice chemical and physical interactions (AICI): liquids, quasi-liquids, and solids in snow, *Atmospheric Chemistry and Physics*, 14, 1587–1633. https://doi.org/10.5194/acp-14-1587-2014

Beer, J., Finkel, R.C., Bonani, G.,Gäggeler, H., Görlach, U., Jacob, P., et al. (1991). Seasonal variations in the concentrations of 10Be, Cl^-, NO_3^-, SO_4^{2-}, H_2O_2, ^{210}Pb, ^3H mineral dust and $d^{18}O$ in Greenland snow. *Atmosphere Environment*, 25 (5–6), 899–904.

Benson, C.S. (1962). Stratigraphic studies in the snow and firn of the Greenland Ice Sheet. Research Report 70, Snow, Ice and Permafrost Research Establishment.

Bourne, A. J., Cook, E., Abbott, P. M., Seierstad, I. K., Steffensen, J. P., Svensson, A., et al. (2015). A tephra lattice for Greenland and a reconstruction of volcanic events spanning 25–45 ka b2k. *Quaternary Science Reviews*, 118, 122–141.

Box, J.E., Yang, L., Rogers, J., Bromwich, D., Bai, L.S., Steffen, K., et al. (2005). Extreme Precipitation Events over Greenland: Consequences to Ice Sheet Mass Balance. American Meteorological Society: San Diego, CA, 8th International Conference on Polar Meteorology and Oceanography, 9–13 January 2005, paper 5·2.

Brimblecombe, P., Tranter, M., Abrahams, P.W., Blackwood, I., Davies, T.D. & Vincent, C.E. (1985). Relocation and preferential elution of acidic solute through the snowpack of a small, remote, high-altitude Scottish catchment. *Annals of Glaciology*, 7, 141–147.

Buchardt, S. L., Clausen, H. B., Vinther, B. M., & Dahl-Jensen, D. (2012). Investigating the past and recent δ18O-accumulation relationship seen in Greenland ice cores. *Climate of the Past*, 8(6), 2053–2059. https://doi.org/10.5194/cp-8-2053-2012

Burgess, E. W., Forster, R. R., Box, J. E., Mosley-Thompson, E., Bromwich, D. H., Bales, R. C., & Smith, L. C. (2010). A spatially calibrated model of annual accumulation rate on the Greenland Ice Sheet (1958–2007). *Journal of Geophysical Research: Earth Surface*, 115, F02004. doi:10.1029/2009JF001293

Chylek, P., Dubey, M. K., & Lesins, G. (2006). Greenland warming of 1920–1930 and 1995–2005, *Geophysical Research Letters*, 33, L11707. doi:10.1029/2006GL026510

Clausen, H. B., & Hammer, C. U. (1988). The Laki and Tambora eruptions as revealed in Greenland ice cores from 11 locations. *Annals of Glaciology*, 10,16–22.

Clausen, H. B., Hammer, C. U., Hvidberg, C. S., DahlJensen, D., Steffensen, J. P., Kipfstuhl, J., & Legrand, M. (1997). A comparison of the volcanic records over the past 4000 years from the Greenland Ice Core Project and Dye 3 Greenland ice cores. *Journal of Geophysical Research: Oceans*, 102(C12), 26707-26723.

Cook, E., Portnyagin, M., Ponomareva, V., Bazanova, L., Svensson, A., & Garbe-Schönberg, D. (2018). First identification of cryptotephra from the Kamchatka Peninsula in a Greenland ice core: Implications of a widespread marker deposit that links Greenland to the Pacific northwest. *Quaternary Science Reviews*, 181, 200–206.

Cragin, J.H., Hewitt, A. D., & Colbeck, S. C. (1993). Elution of ions from melting snow. Army Cold Regions Research and Engineering Laboratory. *CRREL Report*, 93–8.

Craig, H. (1961). Isotopic variation in meteoric waters. *Science*, 133 (3465), 1702–1703. doi: 10.1126/science.133.3465.1702

Culberg, R., Schroeder, D.M., & Chu, W. (2021). Extreme melt season ice layers reduce firn permeability across Greenland. *Nature Communications*, 12, 1–9. doi:10.1038/s41467-021-22656-5

Cullen, D., & Baker, I. (2001). Observation of impurities in ice. *Microscopy Research Technique*, 55, 198–207. doi:10.1002/jemt.10000

Curtis, C. J., Kaiser, J., Marca, A., Anderson, N. J., Simpson, G., Jones, V., & Whiteford, E. (2018). Spatial variations in snowpack chemistry, isotopic composition of NO_3^- and nitrogen deposition from the ice sheet margin to the coast of western Greenland. *Biogeosciences*, 15, 529–550. https://doi.org/10.5194/bg-15-529-2018, 2018

Dansgaard, W. (1964). Stable isotopes in precipitation. *Tellus*, 16(4), 436–468. doi:10.3402/tellusa.v16i4.8993

Dansgaard, W., Clausen, H. B., Gunderstrup, N., Hammer, C. U., Johnsen, S. J., Krristindottir, P. M., & Reeh, N. (1982) A new Greenland deep ice core. *Science*, 218, 1273–1277.

Dansgaard, W., White, J. W. C., & Johnsen, S. J. (1989). The abrupt termination of the Younger Dryas climate event. *Nature*, 339, 532–534.

Dahl-Jensen, D., Gundestrup, N., Miller, H., Watanabe, O., Johnsen, S., Steffensen, J., et al. (2002). The NorthGRIP deep drilling programme. *Annals of Glaciology, 35*, 1–4. doi:10.3189/172756402781817275

Das, S.B., et al. (2009). Greenland ACT Ice Cores Melt Layer Stratigraphy. IGBP PAGES/World Data Center for Paleoclimatology Data Contribution Series # 2009-058.
NOAA/NCDC Paleoclimatology Program, Boulder CO, USA.

Davidson, C.I., Jaffrezo, J.L. Mosher, B.W., Dibb, J.E., Borys, R.D., Bodhaine, R.A., et al. (1993). Chemical constituents in the air and snow at Dye3 Greenland-I. Seasonal variations *Atmospheric Environment*, 27A (17/18), 2709–2722.

Davies, T.D., Vincent, C.E., & Brimblecombe, P. (1982). Preferential elution of strong acids from a Norwegian ice cap. *Nature*, 300, 161–163. doi:10.1038/300161a0

Davis, R.E., Petersen, C.E., & Bales, R.C. (1995). Ion flux through a shallow snowpack: effects of initial conditions and melt sequences. *IAHS Publications-Series of Proceedings and Reports-Intern Association Hydrological Sciences*, 228, 115–128.

de la Peña, S., Howat, I. M., Nienow, P. W., van den Broeke, M. R., Mosley-Thompson, E., Price, S. F., et al. (2015). Changes in the firn structure of the western Greenland Ice Sheet caused by recent warming, *The Cryosphere*, 9, 1203–1211. https://doi.org/10.5194/tc-9-1203-2015, 2015

Enderlin, E. M., Howat, I. M. Jeong, S., Noh, M.-J., vanAngelen, J.H., & van den Broeke, M.R. (2014). An improved mass budget for the Greenland ice sheet. *Geophysical Research Letters*, 41, 866–872. doi:10.1002/2013GL059010

Eichler, A., Schwikowski, M., & Gäggelerm H.W. (2001). Meltwater-induced relocation of chemical species in Alpine firn. *Tellus Series B: Chemical and Physical Meteorology*, 53(2), 192–203. doi:10.1034/j.1600-0889. 2001.d01-15.x

Fettweis, X., Hofer, S., Krebs-Kanzow, U., Amory, C., Aoki, T., Berends, C. J., et al. (2020). GrSMBMIP: intercomparison of the modelled 1980–2012 surface mass balance over the Greenland Ice Sheet, *The Cryosphere*, 14, 3935–3958. https://doi.org/10.5194/tc-14-3935-2020

Fegyveresi, J. M., Alley, R. B., Muto, A., Orsi, A. J., & Spencer, M. K. (2018). Surface formation, preservation, and history of low-porosity crusts at the WAIS Divide site, West Antarctica. *The Cryosphere*, 12, 325–341. Doi:10.5194/tc-12-325-2018

Fisher, D.A., & Koerner, R.M. (1986). On the special rheological properties of ancient microparticle-laden Northern Hemisphere ice as derived from bore-hole and core measurements. *Journal of Glaciology*, 32 (112), 501–510. doi:10.3189/S0022143000012211

Fischer, H., Wagenbach, D., & Kipfstuhl, J. (1998). Sulfate and nitrate firn concentrations on the Greenland ice sheet: 2. Temporal anthropogenic deposition changes. *Journal of Geophysical Research*, 103(D17), 21935–21942. doi:10.1029/98JD01886

Fischer, H., Schüpbach, S., Gfeller, G., Bigler, M., Röthlisberger, R., Erhardt, T., et al. (2015). Millennial changes in North American wildfire and soil activity over the last glacial cycle. *Nature Geoscience*, 8, 723– 727. https://doi.org/10.1038/ngeo2495

Frey, M. M., Bales, R. C., & McConnell, J. R. (2006). Climate sensitivity of the century-scale hydrogen peroxide (H_2O_2) record preserved in 23 ice cores from West Antarctica. *Journal of Geophysical Research Atmospheres*, 111(21). https://doi.org/10.1029/2005JD006816

Fuhrer, K., Neftel, A. Anklin, M., Staffelbach, T., Legrand, M. (1996). High-resolution ammonium ice core record covering a complete glacial-interglacial cycle. *Journal of Geophysical Research*, 101 (D12),4147–4164.

Fujita, S., Hirabayashi, M., Goto-Azuma, K., Dallmayr, R., Satow, K., Zheng, J., & Dahl-Jensen, D. (2014). Densification of layered firn of the ice sheet at NEEM, Greenland. *Journal of Glaciology*, 60(223), 905–921. doi: http://dx.doi.org/10.3189/2014JoG14J006

Fujita, S., Goto-Azuma, K., Hirabayashi, M., Hori, A., Iizuka, Y., Motizuki, Y., Motoyama, H., & Takahashi, K. (2016). Densification of layered firn in the ice sheet at Dome Fuji, *Antarctica, Journal of Glaciology*, 1–21. doi:10.1017/jog.2016.16

Fujita, K., Matoba, S., Iizuka, Y., Takeuchi, N., Tsushima, A., Kurosaki, Y., & Aoki, T. (2021). Physically based summer temperature reconstruction from melt layers in ice cores. *Earth and Space Science*, 8, e2020EA001590. https://doi.org/10.1029/2020EA001590

Fukazawa, H., Sugiyama, K., Mae, S., Narita, H., & Hondoh, T. (1998). Acid ions at triple junction of Antarctic ice observed by Raman scattering. *Geophysical Research Letters*, 25(15), 2845–2848. doi:10.1029/98GL02178

Furukawa, R., Uemura, R., Fujita, K., Sjolte, J., Yoshimura, K., Matoba, S., & Iizuka, Y. (2017). Seasonal-scale dating of a shallow ice core from Greenland using oxygen isotope matching between data and simulation. *Journal of Geophysical Research: Atmospheres*, 122, 10,873– 10,887. https://doi.org/10.1002/2017JD026716

Gfeller, G., Fischer, H., Bigler, M., Schüpbach, S., Leuenberger, D., & Mini, O. (2014). Representativeness and seasonality of major ion records derived from NEEM firn cores. *The Cryosphere*, 8(5), 1855–1870. https://doi.org/10.5194/tc-8-1855-2014

Graeter, K. A., Osterberg, E. C., Ferris, D. G., Hawley, R. L., Marshall, H. P., Lewis, G., et al. (2018). Ice core records of West Greenland melt and climate forcing. *Geophysical Research Letters*, 45, 3164– 3172. https://doi.org/10.1002/2017GL076641

Halde, R. (1980). Concentration of impurities by progressive freezing. *Water Research*, 14(6), 575–580. doi:10.1016/0043-1354(80)90115-3

Hall, D. K., Comiso, J. C., Digirolamo, N. E., Shuman, C. A., Box, J. E., & Koenig, L. S. (2013). Variability in the surface temperature and melt extent of the Greenland ice sheet from MODIS. *Geophysical Research Letters*, 40(10), 2114–2120. https://doi.org/10.1002/grl.50240

Hammer, C. U. (1980). Acidity of polar ice cores in relation to absolute dating, past volcanism, and radio-echoes, *Journal of glaciology*, 25, 359–372.

Hanna, E., McConnell, J., Das, S., Cappelen, J., & Stephens, A. (2006). Observed and modeled Greenland ice sheet snow accumulation, 1958–2003, and links with regional climate forcing. *Journal of Climate*, *19*(3), 344–358.

Hansson, M.E., & Saltzman, E. S. (1993). The first Greenland ice core record of methanesulfonate and sulfate over a full glacial cycle. *Geophysical Research Letters*, 20, 1163–1166, doi.org/10.1029/93GL00910

Hansson, M. & Holmén, K. (2001). High latitude biospheric activity during the last glacial cycle revealed by ammonium variations in Greenland ice cores. *Geophysical Research Letters* 28, 22, 4239–4242. doi: 10.1029/2000GL01231

Hattori, S., Iizuka, Y., Alexander, B., Ishino, S., Fujita, K., Zhai, S., et al. (2021). Isotopic evidence for acidity-driven enhancement of sulfate formation after SO2 emission control. *Science Advances*, 7(19). doi: 10.1126/sciadv.abd4610

Herron, M.M., Herron, S.L., & Langway, C.C. Jr. (1981). Climatic signal of ice melt features in southern Greenland. *Nature*, 293(5831), 389–391. doi:10.1038/293389a0

Hersbach, H., Bell, B., Berrisford, P., Hirahara, S., Horányi, A., Muñoz-Sabater, J., et al. (2020). The ERA5 global reanalysis. *Quarterly Journal of the Royal Meteorological Society* 146:1999-2049. https://doi.org/10.1002/qj.3803

Hirose, S., Aoki, T., Niwano, M., Matoba, S., Tanikawa T., Yamaguchi, S., & Yamasaki, T. (2021). Surface energy balance observed at the SIGMA-A site on the northwest Greenland ice sheet. *Seppyo*, 83(2), 143-154.

Hori, A., Tayuki, K., Narita, H., Hondoh, T., Fujita, S., Kameda, T., et al. (1999). A detailed density profile of the Dome Fuji (Antarctica) shallow ice core by X-ray transmission method. *Annals of Glaciology*, 29, 211–214.

Hutterli, M. A., McConnell, J. R., Bales, R. C. & Stewart, R. W. (2003). Sensitivity of hydrogen peroxide (H_2O_2) andformaldehyde (HCHO) preservation in snow to changing environmental conditions: Implications for ice core records. *Journal of Geophysical Research*,108(D1), 4023. doi:10.1029/2002JD002528

Iizuka, Y., Igarashi, M., Kamiyama, K., Motoyama, H., & Watanabe, O. (2002). Ratios of Mg^{2+}/Na^{+} in snowpack and an ice core at Austfonna ice cap, Svalbard, as an indicator of seasonal melting. *Journal of Glaciology*, 48(162), 452–460. doi:10.3189/172756502781831304

Iizuka, Y., Miyake, T., Hirabayashi, M., Suzuki, T., Matoba, S., Motoyama, H., et al. (2009). Constituent elements of insoluble and non-volatile particles during the Last Glacial Maximum exhibited in the Dome Fuji (Antarctica) ice core. *Journal of Glaciology,* 55(191), 552-562. doi:10.3189/002214309788816696

Iizuka, Y., Tsuchimoto, A., Hoshina, Y., Sakurai, T., Hansson, M., Karlin, T., et al. (2012a). The rates of sea salt sulfatization in the atmosphere and surface snow of inland Antarctica. *Journal of Geophysical Research*, 117, D04308. doi:10.1029/2011JD016378

Iizuka, Y., Uemura, R., Motoyama, H., Suzuki, T., Miyake, T., Hirabayashi M., & Hondoh, T. (2012b). Sulphate-climate coupling over the past 300,000 years in inland Antarctica. *Nature*, 490(7418), 81– 84. doi:10.1038/nature11359

Iizuka, Y., Delmonte, B., Oyabu, I., Karlin, T., Maggi, V., Albani, S., Fukui, M., Hondoh, T., & Hansson, M. (2013). Sulphate and chloride aerosols during Holocene and last glacial periods preserved in the Talos Dome Ice Core, a peripheral region of Antarctica. *Tellus. Series B, Chemical and physical meteorology*, 65(1), 20197. doi:10.3402/tellusb.v65i0.20197

Iizuka, Y., Matoba, S., Yamasaki, T., Oyabu, I., Kadota, M., & Aoki, T. (2016). Glaciological and meteorological observations at the SE-Dome site, southeastern Greenland Ice Sheet. *Bulletin of Glaciological Research*, 34,1–10. https://doi.org/10.5331/bgr.15R03

Iizuka, Y., Miyamoto, A., Hori, A., Matoba, S., Furukawa, R., Saito, T., Fujita, S., Hirabayashi, M., Yamaguchi, S., Fujita, K., & Takeuchi, N. (2017). A firn densification process in the high accumulation dome of southeastern Greenland, *Arctic, Antarctic, and Alpine Research*, 49(1), 13–27. DOI: http://dx.doi.org/10.1657/AAAR0016-034

Iizuka, Y., Uemura, R., Fujita, K., Hattori, S., Seki, O., Miyamoto, C., et al. (2018). A 60 year record of atmospheric aerosol depositions preserved in a high-accumulation dome ice core, Southeast Greenland. *Journal of Geophysical Research: Atmospheres*, 123, 574– 589. https://doi.org/10.1002/2017JD026733

Iizuka, Y., Matoba, S., Minowa, M., Yamasaki, T., Kawakami, K., Kakugo, A., et al. (2021). Ice Core Drilling and Related Observations at SE-Dome site, southeastern Greenland Ice Sheet, *Bulletin of Glaciological Research*, 39, 1–12.

IPCC AR6 (2021). *Climate Change 2021: The Physical Science Basis. Contribution of Working Group I to the Sixth Assessment Report of the Intergovernmental Panel on Climate Change* [Masson-Delmotte, V., P. Zhai, A. Pirani, S.L. Connors, C. Péan, S. Berger, N. Caud, Y. Chen, L. Goldfarb, M.I. Gomis, M. Huang, K. Leitzell, E. Lonnoy, J.B.R. Matthews, T.K. Maycock, T. Waterfield, O. Yelekçi, R. Yu, and B. Zhou (eds.)]. Cambridge University Press, Cambridge, United Kingdom and New York, NY, USA, In press, doi:10.1017/9781009157896.

Johannessen, O.M., Bengtsson, L., Miles, M.W., Kuzmina, S.I., Semenov, V.A., Alekseev, G.V., et al. (2004). Arctic climate change: observed and modelled temperature and sea-ice variability. *Tellus A*, 56: 328-341. https://doi.org/10.1111/j.1600-0870.2004.00060.x

Johnsen, S. J., Dahl-Jensen, D., Dansgaard, W., & Gundestrup, N. (1995). Greenland palaeotemperatures derived from GRIP bore hole temperature and ice core isotope profiles, *Tellus B: Chemical and Physical Meteorology*, 47:5, 624–629. DOI: 10.3402/tellusb.v47i5.16077

Jouzel, J., & Souchez, R. A. (1982). Melting–Refreezing at the Glacier Sole and the Isotopic Composition of the Ice. *Journal of Glaciology*, 28(98), 35–42. doi:10.3189/S0022143000011771

Kameda, T., Narita, H., Shoji, H., Nishio, F., Fujii, Y., & Watanabe, O. (1995). Melt features in ice cores from site j, southern Greenland: Some implications for summer climate since ad 1550. *Annals of Glaciology*, 21, 51– 58. https://doi.org/10.3189/S0260305500015597

Kameda, T. & Takahashi, S. (2014). Glaciology. Kokon-shoin, Japan.

Kamiyama, K., Ageta, Y., & Fujii, Y. (1989). Atmospheric and depositional environments traced from unique chemical compositions of the snow over an inland high plateau, Antarctica, *Journal of Geophysical Research*, 94, D15, 18515–18519.

Kang, S., Huang, J., & Xu, Y. (2008). Changes in ionic concentrations and δ18O in the snowpack of Zhadang glacier, Nyainqentanglha mountain, southern Tibetan Plateau. *Annals of Glaciology*, 49, 127–134. https://doi.org/10.3189/172756408787814708

Keegan, K. M., Albert, M. R., McConnel, J. R., & Baker, I. (2014). Climate change and forest fires synergistically drive widespread melt events of the Greenland Ice Sheet. *PNAS*, 111(22), 7964–7967.

Kendall, M.G. (1975) *Rank Correlation Measures*. London: Charles Griffin

Khalzan, P., Sakai, A., & Fujita, K. (2022) Mass Balance of Four Mongolian Glaciers: In-situ Measurements, LongTerm Reconstruction and Sensitivity Analysis. *Frontier. Earth Science*. 9:785306. doi: 10.3389/feart.2021.785306

Krabill, W. Hanna, E., Huybrechts, P., Abdalati, W., Cappelen, J., Csatho, B., et al. (2004). Greenland ice sheet: increased coastal thinning. *Geophysical Research Letters*, 31 (24). https://doi.org/10.1029/2004GL021533

Karlsson, N., Razik, S., Hörhold, M., Winter, A., Steinhage, D., Binder, T., & Eisen, O. (2020). Surface accumulation in Northern Central Greenland during the last 300 years. *Annals of Glaciology, 61*(81), 214-224. doi:10.1017/aog.2020.30

Kaufman, D. S., Schneider, D. P., McKay, N. P., Ammann, C. M., Bradley, R. S.,Briffa, K. R., et al. (2009). Recent warming reverses long-term Arctic cooling. *Science*, 325, 1236–123.

Koerner, R. M. (1977). Devon Island ice cap: core stratigraphy and paleoclimate. *Science*, 196(4285), 15–18. doi:10.1126/science.196.4285.15

Koerner, R. M., & Fisher, D. A. (1990). A record of Holocene summer climate from a Canadian high - Arctic ice core. *Nature*, 343(6259), 630–631. https://doi.org/10.1038/343630a0

Kuramoto, T., Goto-Azuma, K., Hirabayashi, M., Miyake, T., Motoyama, H., Dahl-Jensen, D., & Steffensen, J. P. (2011). Seasonal variations of snow chemistry at NEEM, Greenland. *Annals of Glaciology*, 52 (58), 193e199.

Kurosaki, Y., Matoba, S., Iizuka, Y., Niwano, M., Tanikawa, T., Ando, T., et al. (2020). Reconstruction of sea ice concentration in northern Baffin Bay using deuterium excess in a coastal icecore from the northwestern Greenland Ice Sheet. *Journal of Geophysical Research: Atmospheres*, 125, e2019JD031668. doi:10.1029/2019JD031668

Lacelle, D. (2011). On the $\delta^{18}O$, δD and D-excess relations in meteoric precipitation and during equilibrium freezing: theoretical approach and field examples. *Permafrost and Periglacial Processes*, 22, 13–25. doi:10.1002/ppp.712

Langway, C. C. Jr (1967). Stratigraphic analysis of a deep ice core from Greenland. *CRREL Res. Rep*. 77.

Lazrus, A. L., Kok, G. L., Gitlin, S. N., Lind, J. A., & Mclaren, S. E. (1985). Automated fluorimetric method for hydrogen peroxide in atmospheric precipitation, *Analytical Chemistry*, 57, 917-922. doi:10.1021/ac00281a031

Lee, J., Nez, V. E., Feng, X., Kirchner, J. W., Osterhuber, R., & Renshaw, C. E. (2008). A study of solute redistribution and transport in seasonal snowpack using natural and artificial tracers. *Journal of Hydrology*, 243–254. https://doi.org/10.1016/j.jhydrol.2008.05.004

Legrand, M., & Mayewski, P. (1997). Glaciochemistry of polar ice cores: A review, *Reviews of Geophysics*, 35, 3, 219– 243. DOI: 10.1029/96RG03527.

Li, Z., Edwards, R., Mosley-Thompson, E., Wang, F., Dong, Z., You, X., et al. (2006). Seasonal variability of ionic concentrations in surface snow and elution processes in snow–firn packs at the PGPI site on Ürümqi glacier No. 1, eastern Tien Shan, China. *Annals of Glaciology*, 43, 250–256. https://doi.org/10.3189/172756406781812069

MacFerrin, M., Machguth, H., van As, D., Charalampidis, C., Steven, C. M., Heilig, A., et al. (2019). Rapid expansion of Greenlands low -permeability ice slabs. *Nature*, 573(7774), 403–407. doi:10.1038/s41586-019-1550-3

Machguth, H., MacFerrin, M., van As, D., Box, J. E., Charalampidis, C., Colgan, W., et al. (2016). Greenland meltwater storage in firn limited by near-surface ice formation. *Nature Climate Change*, 6(4), 390–393. doi:10.1038/nclimate2899

Mann, H.B. (1945). Non-parametric tests against trend. *Econometrica*, 13, 245–259. doi:10.2307/1907187

Matoba, S., Niwano, M., Tanikawa, T., Iizuka, Y., Yamasaki, T., Kurosaki, Y., et al. (2018). Field activities at the SIGMA-A site, northwestern Greenland Ice Sheet, 2017. *Bulletin of Glaciological Research*, 36, 15– 22. doi:10.5331/bgr.18r01

Mayewski, P. A. (1993). Greenland ice core 'signal'' characteristics: an expanded view of climate change.' Journal of Geophysical Research, 98(D7), 839–847. https://doi.org/10.1029/93jd01085

McConnell, J. R., Arthern, R. J., Mosley-Thompson, E., Davis, C. H., Bales, R. C., Thomas, R., Burkhart, J. F., & Kyne, J. D. (2000). Changes in Greenland ice sheet elevation attributed primarily to snow accumulation variability, *Nature*, 406, 877–879.

Mcgrath, D., Colgan, W., Bayou, N., Muto, A., & Steffen, K. (2013). Recent warming at Summit, Greenland: Global context and implications. *Geophysical Research Letters*, 40(10), 2091–2096. doi:10.1002/grl.50456

Meese, D.A., Gow, A. J., Alley, R. B., Abbott, G. A., Grootes, P., Ram, M., et al. (1997). The Greenland Ice Sheet Project 2 depth-age scale: Methods and results, *Journal of Geophysical Research*, 102(C12), 26411–26423.

Mernild, S. H., Hanna, E., McConnell, J. R., Sigl, M., Beckerman, A. P., Yde, J. C., et al (2015). Greenland precipitation trends in a long-term instrumental climate context (1890–2012): Evaluation of coastal and ice core records. *International Journal of Climatology*, *35*(2), 303–320.

Miège, C., Forster, R., Box, J., Burgess, E., McConnell, J., Pasteris, D., & Spikes, V. (2013). Southeast Greenland high accumulation rates derived from firn cores and ground-penetrating radar. *Annals of Glaciology,* 54(63), 322-332. doi:10.3189/2013AoG63A358

Mojtabavi, S., Wilhelms, F., Cook, E., Davies, S. M., Sinnl, G., Jensen, S., et al. (2020). A first chronology for the East GReenland Ice-core Project (EGRIP) over the Holocene and last glacial termination. *Climate of the Past*, 16, 2359-2380.

Moore, J. C., & Paren, J. G. (1987). A new technique for dielectric logging of Antarctic ice cores, *Journal of Physics (Paris)*, 48(C1), 155-160.

Morlighem, M., Williams, C. N., Rignot, E., An, L., Arndt, J. E., Bamber, J. L., et al. (2017). BedMachine v3: Complete Bed Topography and Ocean Bathymetry Mapping of Greenland From Multibeam Echo Sounding Combined With Mass Conservation, *Geophysical Research Letters*, 44, 11051–11061.

Mosley-Thompson, E., McConnell, J. R., Bales, R. C., Li, Z., Lin, P. N., Steffen, K., et al. (2001). Local to regional-scale variability of annual net accumulation on the Greenland ice sheet from PARCA cores. *Journal of Geophysical Research: Atmospheres*, 106(D24), 33839–33851. https://doi.org/10.1029/2001JD900067

Muller, F. (1962). Zonation in the accumulation area of the glaciers of Axel Heiberg Island,N.W.T., Canada. *Journal of Glaciology*, 4, 302–313.

Mulvaney, R., Wolff, E.W., & Oates, K. (1988). Sulphuric acid at grain boundaries in Antarctic ice. *Nature*, 331(6153), 247–249. doi:10.1038/331247a0

Nagatsuka, N., Goto-Azuma, K., Tsushima, A., Fujita, K., Matoba, S., Onuma, Y., et al. (2021). Variations in mineralogy of dust in an ice core obtained from northwestern Greenland over the past 100 years, *Climate of the Past*, 17, 1341–1362. https://doi.org/10.5194/cp-17-1341-2021

NEEM community members (2013). Eemian interglacial reconstructed from a Greenland folded ice core. *Nature*, 493, 489–494.

Neff, W., Compo, G. P. Ralph, F. M., & Shupe, M. D. (2014). Continental heat anomalies and the extreme melting of the Greenland ice surface in 2012 and 1889. *Journal of Geophysical Research*, 119 (11), 6520–6536.

Nghiem, S. V., Steffen, K., Neumann, G., & Huff, R. (2005). Mapping of ice layer extent and snow accumulation in the percolation zone of the Greenland ice sheet, *Journal of Geophysical Research*, 110, F02017, doi:10.1029/2004JF000234.

Nghiem, S. V., Hall, D. K., Mote, T. L., Tedesco, M., Albert, M. R., Keegan, K., et al. (2012). The extreme melt across the Greenland ice sheet in 2012, *Geophysical Research Letters*, 39. doi:10.1029/2012GL053611

North Greenland Ice Core Project members. (2004). High resolution climate record of The northern hemisphere reaching into the last interglacial period. *Nature*, 431, 147–151.

Obbard, R., Iliescu, D., Cullen, D., & Baker, I. (2003). SEM/EDS comparison of polar and seasonal temperate ice. *Microscopy Research Technique*, 62(1), 49–61. doi: 10.1002/jemt.10381

Ohno, H., Igarashi, M., & Hondoh, T. (2005). Salt inclusions in polar ice core: Location and chemical form of water-soluble impurities. *Earth and Planetary Science Letters*, 232(1–2), 171–178 (doi:10.1016/j.epsl.2005.01.001)

Ohno, H., Igarashi, M., & Hondoh, T. (2006). Characteristics of salt inclusions in polar ice from Dome Fuji, East Antarctica. *Geophysical Research Letters*, 33, L08501. doi:10.1029/2006GL025774

Ohno, H., Iizuka, Y., Horikawa, S., Sakurai, T., Hondoh, T., & Motoyama, H. (2014). Potassium alum and aluminum sulfate micro-inclusions in polar ice from Dome Fuji, East Antarctica. *Polar Science*, 8(1), 1-9.

Ohno, H., Iizuka, Y., Hori, A., Miyamoto, A., Hirabayashi, M., Miyake, T., et al. (2016). Physicochemical properties of bottom ice from Dome Fuji, inland East Antarctica. *Journal of Geophysical Research: Earth Surface*, 121(7), 1230-1250.

O'Neil, J.R. (1968). Hydrogen and oxygen isotope fractionation between ice and water. *Journal of Physical Chemistry*, 72(10), 3683–3684. doi:10.1021/j100856a060

Otosaka, I. N., Shepherd, A., Casal, T. G., Coccia, A., Davidson, M., Di Bella, A., et al. (2020). Surface melting drives fluctuations in airborne radar penetration in West Central Greenland. *Geophysical Research Letters*, 47(17), e2020GL088293.

Oyabu, I., Iizuka, Y., Uemura, R., Miyake, T., Hirabayashi, M., Motoyama, H., et al. (2014). Chemical compositions of sulfate and chloride salts over the last termination reconstructed from the Dome Fuji ice core, inland Antarctica, *Journal of Geophysical Research Atmosphere*, 119, 14,045– 14,058. doi:10.1002/2014JD022030

Oyabu, I., Iizuka, Y., Fischer, H., Schüpbach, S., Gfeller, G., Svensson, A., et al. (2015). Chemical compositions of solid particles present in the Greenland NEEM ice core over the last 110,000 years, *Journal of Geophysical Research Atmosphere*, 120, 9789– 9813. doi:10.1002/2015JD023290

Oyabu, I., Iizuka, Y., Kawamura, K., Wolff, E., Severi, M., Ohgaito, R., et al. (2020). Compositions of dust and sea salts in the Dome C and Dome Fuji ice cores from Last Glacial Maximum to early Holocene based on ice-sublimation and single-particle measurements. *Journal of Geophysical Research: Atmospheres*, 125, e2019JD032208. https://doi.org/10.1029/2019JD032208

Paterson, W. S. B. (1991). Why ice-age ice is sometimes 'soft'. *Cold Regions Science Technology*, 20(1),75–98.

Paterson, W. S. B. (2006) The physics of glaciers -4th ed.

Paden, J., Li, J., Leuschen, C., Rodriguez-Morales, F., & Hale, R. (2010). IceBridge MCoRDS L2 Ice Thickness, Version 1, NASA National Snow and Ice Data Center Distributed Active Archive Center, Boulder, Colorado, USA, https://doi.org/10.5067/GDQ0CUCVTE2Q.

Porter, C., Morin, P., Howat, I., Noh, M.-J., Bates, B., Peterman, K., et al. (2018). ArcticDEM [data set], V1, Harvard Dataverse, https://doi.org/10.7910/DVN/OHHUKH.

Qiao, J., Colgan, W., Jakobs, G., & Nielsen, S. (2021). High-Resolution Tritium Profile in an Ice Core from Camp Century, Greenland. *Environmental Science & Technology*, 55, 20, 13638–13645.

Rasmussen, S. O., Seierstad, I. K., Andersen, K.K., Bigler, M., Dahl-Jensen, D., Johnsen, S.J., et al. (2008). Synchronization of the NGRIP, GRIP, and GISP2 ice cores across MIS 2 and paleoclimatic implications. *Quaternary Science Reviews*, 27(1-2), 18-28. https://doi.org/10.1016/j.quascirev.2007.01.016

Rasmussen, S. O., Bigler, M., Blockley, S. P., Blunier, T., Buchardt, S. L., Clausen, H. B., et al. (2014). A stratigraphic framework for abrupt climatic changes during the Last Glacial period based on three synchronized Greenland ice core records: refining and extending the INTIMATE event stratigraphy. *Quaternary Science Reviews*, 106,14–28.

Sakai, A., Nuimura, T., Fujita, K., Takenaka, S., Nagai, H., & Lamsal, D. (2015). Climate regime of Asian glaciers revealed by GAMDAM glacier inventory, *The Cryosphere*, 9, 865–880. https://doi.org/10.5194/tc-9-865-2015

Sakurai, T., Ohno, H., Genceli, F., Horikawa, S., Iizuka, Y., Uchida, T., & Hondoh, T. (2010a). Magnesium methanesulfonate salt found in the Dome Fuji (Antarctica) ice core. *Journal of Glaciology,* 56(199), 837-842. doi:10.3189/002214310794457335

Sakurai, T., Ohno, H., Horikawa, S., Iizuka, Y., Uchida, T., & Hondoh, T. (2010b). A Technique for Measuring Microparticles in Polar Ice Using Micro-Raman Spectroscopy. *International Journal of Spectroscopy*, 384956. doi:10.1155/2010/384956

Sakurai, T. (2010c). Studies on phase equilibrium states and spatial distributions of water-soluble microparticles preserved in polar ice sheets. Ph.D. thesis, Hokkaido University, Sapporo, Japan.

Sakurai, T., Ohno, H., Horikawa, S., Iizuka, Y., Uchida, T., Hirakawa, K., & Hondoh, T. (2011). The chemical forms of water-soluble microparticles preserved in the Antarctic ice sheet during Termination I. *Journal of Glaciology,* 57(206), 1027-1032. doi:10.3189/002214311798843403

Sakurai, T., Ohno, H., Horikawa, S., Motoyama, H., & Uchida, T. (2017). Micro-droplets containing sulfate in the Dome Fuji deep ice core, Antarctica: findings using micro-Raman spectroscopy Micro-droplets containing sulfate in the Dome Fuji deep ice core, Antarctica. *Journal of Raman spectroscopy*, 48(3),448–452. doi:10.1002/jrs.5040

Salamatin, A. N., Lipenkov, V. Y., Barnola, J. M., Hori, A., Duval, P., & Hondoh, T. (2009). Snow/firn densification in polar ice sheets, In Hondoh, T. (ed.), Institute of Low Temperature Science, Special Issue, 68, 195–222.

Saros, J. E., Anderson, N. J., Juggins, S., Mcgowan, S., Yde, J. C., Telling, J., et al. (2019). Arctic climate shifts drive rapid ecosystem responses across the West Greenland landscape. *Environmental Research Letters*, 14(7), 074027. https://doi.org/10.1088/1748-9326/ab2928

Scambos, T., Stroeve, J., & Koenig, L. (2021). Rain at the Summit of Greenland. Published in Greenland Ice Sheet Today on August 18, 2021, by the National Snow and Ice Data Center, http://nsidc.org/greenlandtoday/2021/08/rain-at-the-summit-of-greenland/

Schüpbach, S., Fischer, H., Bigler, M., Erhardt, T., Gfeller, G., Leuenberger, D., et al. (2018). Greenland records of aerosol source and atmospheric lifetime changes from the Eemian to the Holocene. *Nature communications*, 9(1), 1-10.

Serreze, M. C., & Francis, J. A. (2006). The Arctic amplification debate. *Climatic Change*, *76*, 241–264. https://doi.org/10.1007/s10584-005-9017-y

Shepherd, A., Ivins, E. R., Barletta, V. R., Bentley, M. J., Bettadpur, S., Briggs, K. H., et al. (2012). A reconciled estimate of ice-sheet mass balance. *Science*, 338(6111), 1183-1189.

Sigg, A., & Neftel, A. (1988). Seasonal Variations in Hydrogen Peroxide in Polar Ice Cores, *Annals of Glaciology*, 10, 157–162. https://doi.org/10.3189/S0260305500004353

Sigl, M., McConnell, J.R., Layman, L., Maselli, O., McGwire, K., Pasteris, D., et al. (2013). A new bipolar ice core record of volcanism from WAIS Divide and NEEM and implications for climate forcing of the last 2000 years, *Journal of Geophysical Research*, 118 (3), 1151–1169.

Silvente, E., & Legrand, M. (1993). Ammonium to sulphate ratio in aerosol and snow of Greenland and Antarctic regions. *Geophysical Research Letters*, 20, 8, 687–690. doi: 10.1029/93GL00982

Souchez, R.A., & Jouzel, J. (1984). On the isotopic composition in δD and $\delta^{18}O$ of water and ice during freezing. *Journal of Glaciology*, 30(106), 369–372. doi:10.3189/S0022143000006249

Souchez. R.A., & de Groote, J.M. (1985). δD-$\delta^{18}O$ relationship in ice formed by subglacial freezing: paleoclimatic implications. *Journal of Glaciology*, 31(109), 229–232.

Steen-Larsen, H.C., Masson-Delmotte, V., Sjolte, J., Johnsen, S. J., Vinther, B. M., Bréon, F. M., et al. (2011). Understanding the climatic signal in the water stable isotope records from the NEEM shallow firn/ice cores in northwest Greenland. *Journal of Geophysical Research: Atmospheres*, 116(D6), 6108. https://doi.org/10.1029/2010JD014311

Stoll, N., Eichler, J., Hörhold, M., Shigeyama, W., & Weikusat, I. (2020). A Review of the Microstructural Location of Impurities in Polar Ice and Their Impacts on Deformation. *Frontier Earth Science*, 8:615613. doi:10.3389/feart.2020.615613

Svensson, A., Andersen, K. K., Bigler, M., Clausen, H. B., Dahl-Jensen, D., Davies, S. M., et al. (2008). A 60000 year Greenland stratigraphic ice core chronology, *Climate of the Past*, 4, 47–57. doi:10.5194/cp-4-47-2008

Takenaka, N., Ueda, A., Daimon, T., Bandow, H., Dohmaru, T., & Maeda, Y., (1996). Acceleration Mechanism of Chemical Reaction by Freezing: The Reaction of Nitrous Acid with Dissolved Oxygen. *Journal of Physical Chemistry*, 100, 13874–13884. doi:10.1021/jp9525806

Tedesco, M., Fettweis, X., Mote, T., Wahr, J., Alexander, P., Box, J. E., & Wouters, B. (2013) Evidence and analysis of 2012 Greenland records from spaceborne observations, a regional climate model and reanalysis data, *The Cryosphere*, 7, 615–630. https://doi.org/10.5194/tc-7-615-2013

Trusel, L. D., Das, S. B., Osman, M. B., Evans, M. J., Smith, B. E., Fettweis, X., et al. (2018). Nonlinear rise in Greenland runoff in response to post-industrial arctic warming. *Nature*, 564(7734), 104–108. https://doi.org/10.1038/s41586-018-0752-4

van den Broeke, M. R., Enderlin, E. M., Howat, I. M., Kuipers Munneke, P., Noël, B. P. Y., van de Berg, W. J., van Meijgaard, E., & Wouters, B. (2016). On the recent contribution of the Greenland ice sheet to sea level change, *The Cryosphere*, 10, 1933–1946. https://doi.org/10.5194/tc-10-1933-2016

Vinther, B. M., Jones, P. D., Briffa, K. R., Clausen, H. B., Andersen, K. K., Dahl-Jensen, D., & Johnsen, S. J. (2010). Climatic signals in multiple highly resolved stable isotope records from Greenland. *Quaternary Science Reviews*, 29(3-4), 522–538. https://doi.org/10.1016/j.quascirev.2009.11.002

Virkkunen, K., Moore, J. C., Isaksson, E., Pohjola, V., Perämäki, P., Grinsted, A., & Kekonen, T. (2007). Warm summers and ion concentrations in snow: Comparison of present day with Medieval Warm Epoch from snow pits and an ice core from Lomonosovfonna, Svalbard. *Journal of Glaciology*, 53(183), 623–634. https://doi.org/10.3189/002214307784409388

Wang, S., Shi, X., Cao, W., & Pu, T. (2018). Seasonal variability and evolution of glaciochemistry at an Alpine temperate glacier on the Southeastern Tibetan Plateau. *Water*, 10(2), 114. https://doi.org/10.3390/w10020114

Wang, Y., Sugiyama, S., & Bjørk, A. A. (2021). Surface elevation change of glaciers along the coast of Prudhoe Land, northwestern Greenland from 1985 to 2018. *Journal of Geophysical Research: Earth Surface*, 126, e2020JF006038. https://doi.org/10.1029/2020JF006038

Weinhart, A. H., Kipfstuhl, S., Hörhold, M.,Eisen, O., & Freitag, J., (2021). Spatial Distribution of Crusts in Antarctic and Greenland Snowpacks and Implications for Snow and Firn Studies. *Frontier Earth Science*, 9:630070, doi: 10.3389/feart.2021.630070

Westhoff, J., Sinnl, G., Svensson, A., Freitag, J., Kjær, H. A., Vallelonga, P., et al. (2022). Melt in the Greenland EastGRIP ice core reveals Holocene warm events, *Climate of the Past*, 18, 1011–1034. https://doi.org/10.5194/cp-18-1011-2022, 2022.

Whitby, K.T. (1978). The physical characteristics of sulfur aerosols. *Atmospheric Environment*, 12, 135–159. doi:10.1016/0004-6981(78)90196-8

Whitlow, S., Mayewski, P.A., & Dibb, J.E. (1992). A comparison of major chemical species seasonal concentration and accumulation at the South Pole and Summit, Greenland. *Atmosphere Enviroment*, 26A (11), 2045–2054.

Wilhelms, F., Kipfstuhl, J., Miller, H., Heinloth, K., & Firestone, J. (1998). Precise dielectric profiling of ice cores: a new device with improved guarding and its theory, *Journal of Glaciology*, 44(146), 171-174.

Wolff, E.W., & Paren, J.G. (1984). A two-phase model of electrical conduction in polar ice sheets. *Journal of Geophysical Research. Solid Earth*, 89, 9433–9438. (doi:10.1029/JB089iB11p09433)

Wolff, E.W. (2000). Electrical stratigraphy of polar ice cores: principles, methods, and findings, in *Physics of Ice Core Records*, edited by T. Hondoh, pp. 155-171, Hokkaido University Press, Sapporo.

Zennaro, P., Kehrwald, N., McConnell, J. R., Schuepbach, S., Maselli, O. J., Marlon, J., et al. (2014). Fire in ice: Two millennia of boreal forest fire history from the Greenland NEEM ice core. *Climate of the Past*, 10, 1905– 1924.

Zhang, Q., Huai, B., van Den Broeke, M. R., Cappelen, J., Ding, M., Wang, Y., & Sun, W. (2022). Temporal and Spatial Variability in Contemporary Greenland Warming (1958–2020). *Journal of Climate*, 35(9), 2755-2767.

Zielinski, G. A., Mayewski, P. A., Meeker, L. D., Whitlow, S., Twickler, M. S., Morrison, M., et al. (1994). Record of volcanism since 7000 BC from the GISP2 Greenland ice core and implications for the volcano-climate system. *Science*, 264(5161), 948–952.

Supplementary figure

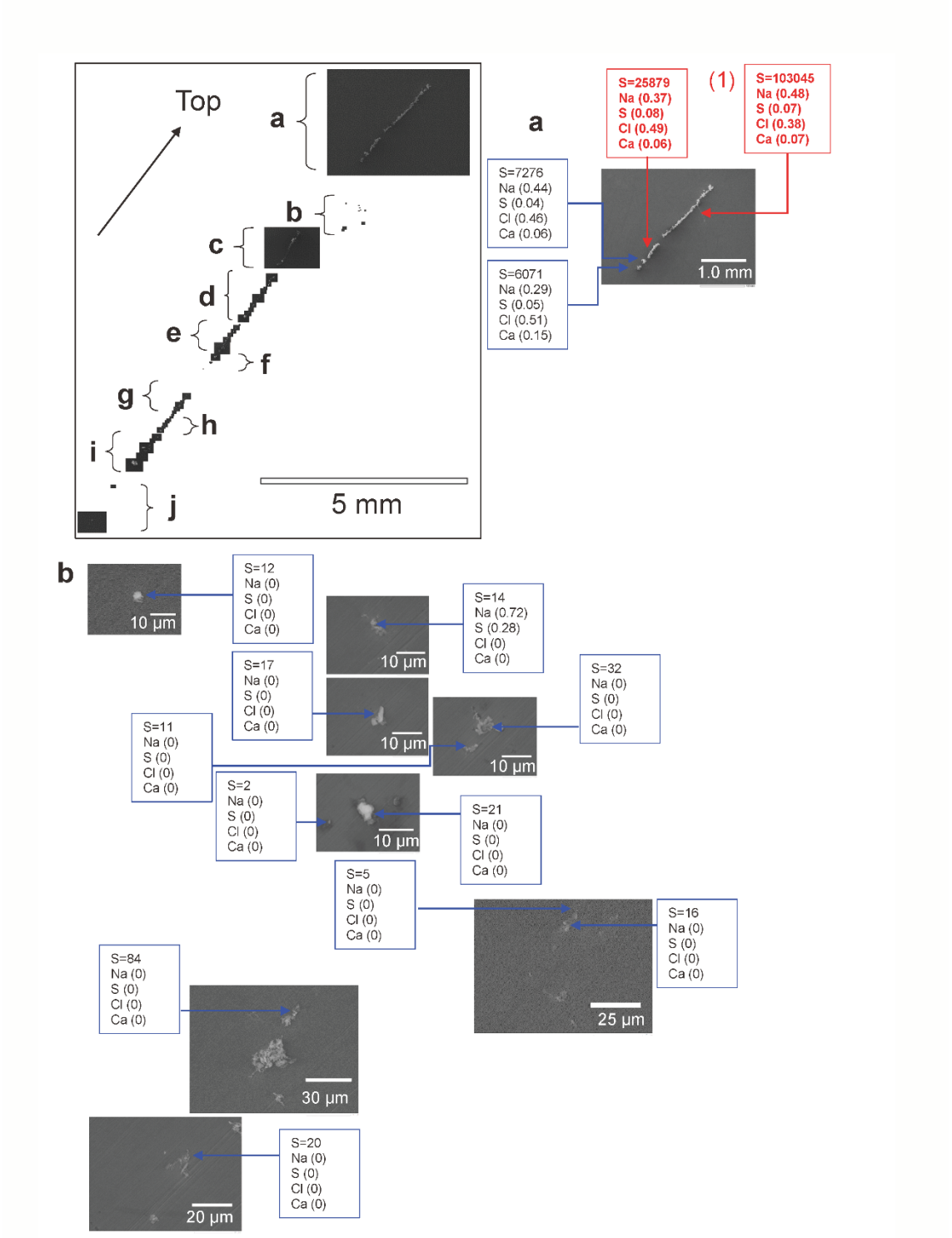

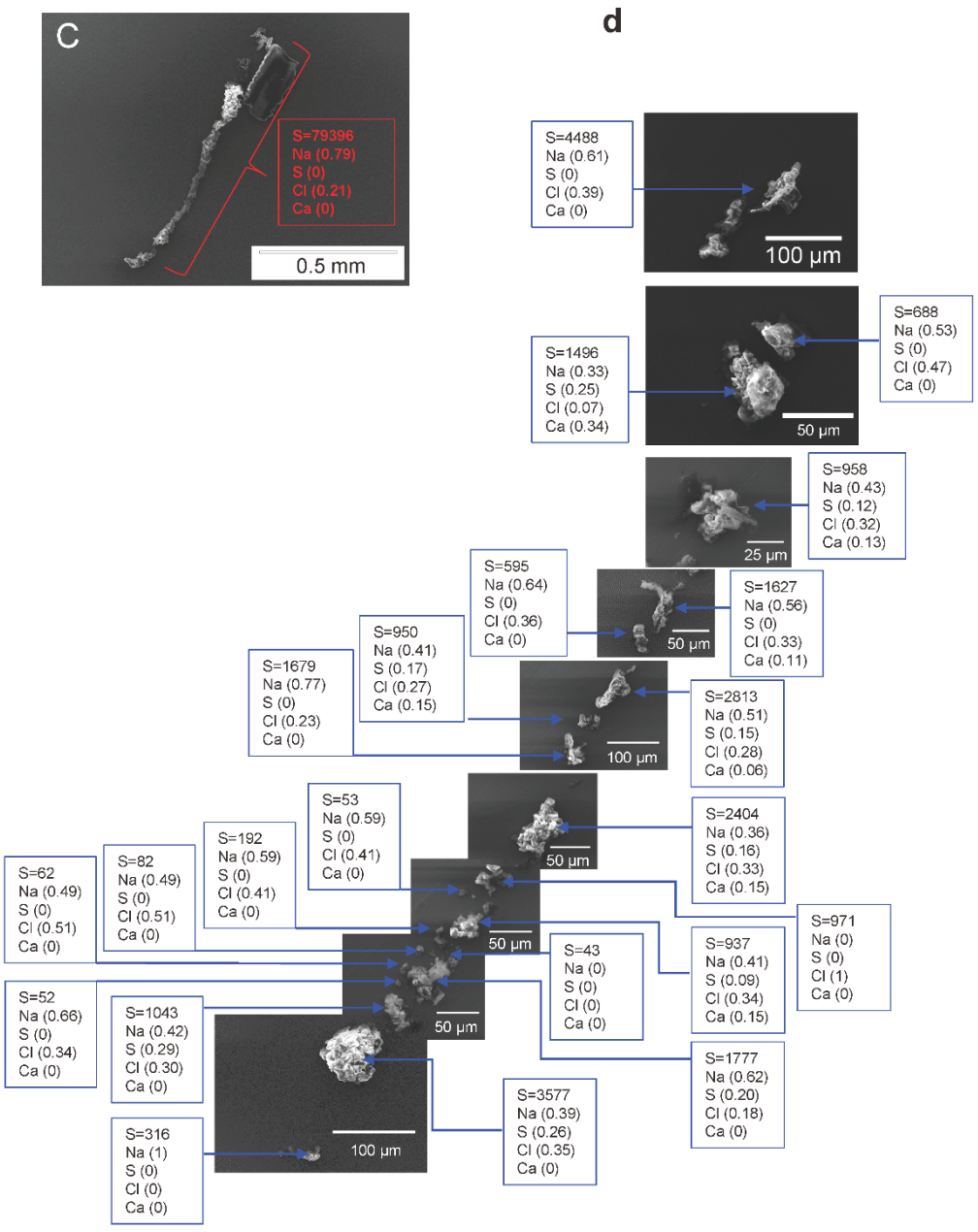
C
S=79396
Na (0.79)
S (0)
Cl (0.21)
Ca (0)
0.5 mm
d
S=4488
Na (0.61)
S (0)
Cl (0.39)
Ca (0)
100 µm
S=1496
Na (0.33)
S (0.25)
Cl (0.07)
Ca (0.34)
S=688
Na (0.53)
S (0)
Cl (0.47)
Ca (0)
50 µm
S=958
Na (0.43)
S (0.12)
Cl (0.32)
Ca (0.13)
25 µm
S=595
Na (0.64)
S (0)
Cl (0.36)
Ca (0)
S=1627
Na (0.56)
S (0)
Cl (0.33)
Ca (0.11)
50 µm
S=1679
Na (0.77)
S (0)
Cl (0.23)
Ca (0)
S=950
Na (0.41)
S (0.17)
Cl (0.27)
Ca (0.15)
S=2813
Na (0.51)
S (0.15)
Cl (0.28)
Ca (0.06)
100 µm
S=53
Na (0.59)
S (0)
Cl (0.41)
Ca (0)
S=2404
Na (0.36)
S (0.16)
Cl (0.33)
Ca (0.15)
50 µm
S=62
Na (0.49)
S (0)
Cl (0.51)
Ca (0)
S=82
Na (0.49)
S (0)
Cl (0.51)
Ca (0)
S=192
Na (0.59)
S (0)
Cl (0.41)
Ca (0)
S=971
Na (0)
S (0)
Cl (1)
Ca (0)
50 µm
S=43
Na (0)
S (0)
Cl (0)
Ca (0)
S=937
Na (0.41)
S (0.09)
Cl (0.34)
Ca (0.15)
S=52
Na (0.66)
S (0)
Cl (0.34)
Ca (0)
S=1043
Na (0.42)
S (0.29)
Cl (0.30)
Ca (0)
50 µm
S=1777
Na (0.62)
S (0.20)
Cl (0.18)
Ca (0)
S=3577
Na (0.39)
S (0.26)
Cl (0.35)
Ca (0)
S=316
Na (1)
S (0)
Cl (0)
Ca (0)
100 µm

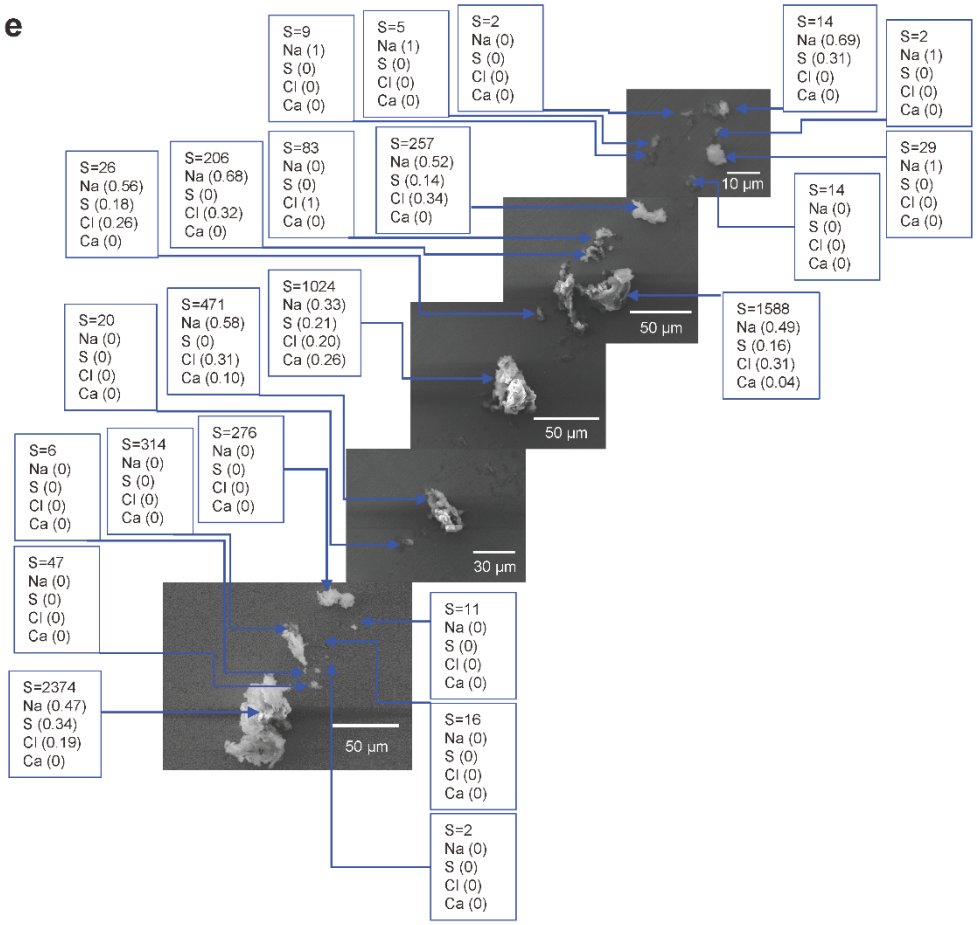
e
S=9
Na (1)
S (0)
Cl (0)
Ca (0)
S=5
Na (1)
S (0)
Cl (0)
Ca (0)
S=2
Na (0)
S (0)
Cl (0)
Ca (0)
S=14
Na (0.69)
S (0.31)
Cl (0)
Ca (0)
S=2
Na (1)
S (0)
Cl (0)
Ca (0)
S=26
Na (0.56)
S (0.18)
Cl (0.26)
Ca (0)
S=206
Na (0.68)
S (0)
Cl (0.32)
Ca (0)
S=83
Na (0)
S (0)
Cl (1)
Ca (0)
S=257
Na (0.52)
S (0.14)
Cl (0.34)
Ca (0)
S=29
Na (1)
S (0)
Cl (0)
Ca (0)
10 µm
S=14
Na (0)
S (0)
Cl (0)
Ca (0)
S=1024
Na (0.33)
S (0.21)
Cl (0.20)
Ca (0.26)
S=471
Na (0.58)
S (0)
Cl (0.31)
Ca (0.10)
S=20
Na (0)
S (0)
Cl (0)
Ca (0)
50 µm
S=1588
Na (0.49)
S (0.16)
Cl (0.31)
Ca (0.04)
S=6
Na (0)
S (0)
Cl (0)
Ca (0)
S=314
Na (0)
S (0)
Cl (0)
Ca (0)
S=276
Na (0)
S (0)
Cl (0)
Ca (0)
50 µm
S=47
Na (0)
S (0)
Cl (0)
Ca (0)
30 µm
S=11
Na (0)
S (0)
Cl (0)
Ca (0)
S=2374
Na (0.47)
S (0.34)
Cl (0.19)
Ca (0)
S=16
Na (0)
S (0)
Cl (0)
Ca (0)
50 µm
S=2
Na (0)
S (0)
Cl (0)
Ca (0)

f

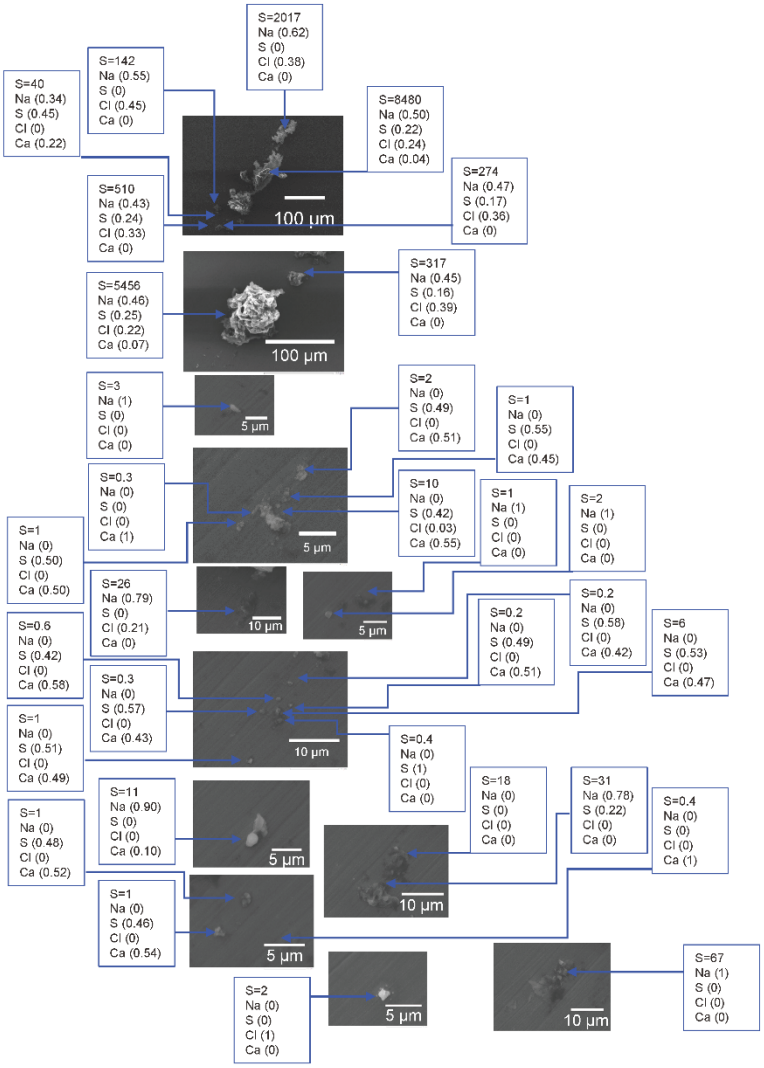
S=2017
Na (0.62)
S (0)
Cl (0.38)
Ca (0)
S=142
Na (0.55)
S (0)
Cl (0.45)
Ca (0)
S=40
Na (0.34)
S (0.45)
Cl (0)
Ca (0.22)
S=8480
Na (0.50)
S (0.22)
Cl (0.24)
Ca (0.04)
S=274
Na (0.47)
S (0.17)
Cl (0.36)
Ca (0)
S=510
Na (0.43)
S (0.24)
Cl (0.33)
Ca (0)
100 µm
S=317
Na (0.45)
S (0.16)
Cl (0.39)
Ca (0)
S=5456
Na (0.46)
S (0.25)
Cl (0.22)
Ca (0.07)
100 µm
S=3
Na (1)
S (0)
Cl (0)
Ca (0)
5 µm
S=2
Na (0)
S (0.49)
Cl (0)
Ca (0.51)
S=1
Na (0)
S (0.55)
Cl (0)
Ca (0.45)
S=0.3
Na (0)
S (0)
Cl (0)
Ca (1)
5 µm
S=10
Na (0)
S (0.42)
Cl (0.03)
Ca (0.55)
S=1
Na (1)
S (0)
Cl (0)
Ca (0)
S=2
Na (1)
S (0)
Cl (0)
Ca (0)
S=1
Na (0)
S (0.50)
Cl (0)
Ca (0.50)
S=26
Na (0.79)
S (0)
Cl (0.21)
Ca (0)
10 µm
5 µm
S=0.2
Na (0)
S (0.58)
Cl (0)
Ca (0.42)
S=0.2
Na (0)
S (0.49)
Cl (0)
Ca (0.51)
S=6
Na (0)
S (0.53)
Cl (0)
Ca (0.47)
S=0.6
Na (0)
S (0.42)
Cl (0)
Ca (0.58)
S=0.3
Na (0)
S (0.57)
Cl (0)
Ca (0.43)
10 µm
S=1
Na (0)
S (0.51)
Cl (0)
Ca (0.49)
S=0.4
Na (0)
S (1)
Cl (0)
Ca (0)
S=18
Na (0)
S (0)
Cl (0)
Ca (0)
S=31
Na (0.78)
S (0.22)
Cl (0)
Ca (0)
S=0.4
Na (0)
S (0)
Cl (0)
Ca (1)
S=1
Na (0)
S (0.48)
Cl (0)
Ca (0.52)
S=11
Na (0.90)
S (0)
Cl (0)
Ca (0.10)
5 µm
10 µm
S=1
Na (0)
S (0.46)
Cl (0)
Ca (0.54)
5 µm
S=2
Na (0)
S (0)
Cl (1)
Ca (0)
5 µm
10 µm
S=67
Na (1)
S (0)
Cl (0)
Ca (0)

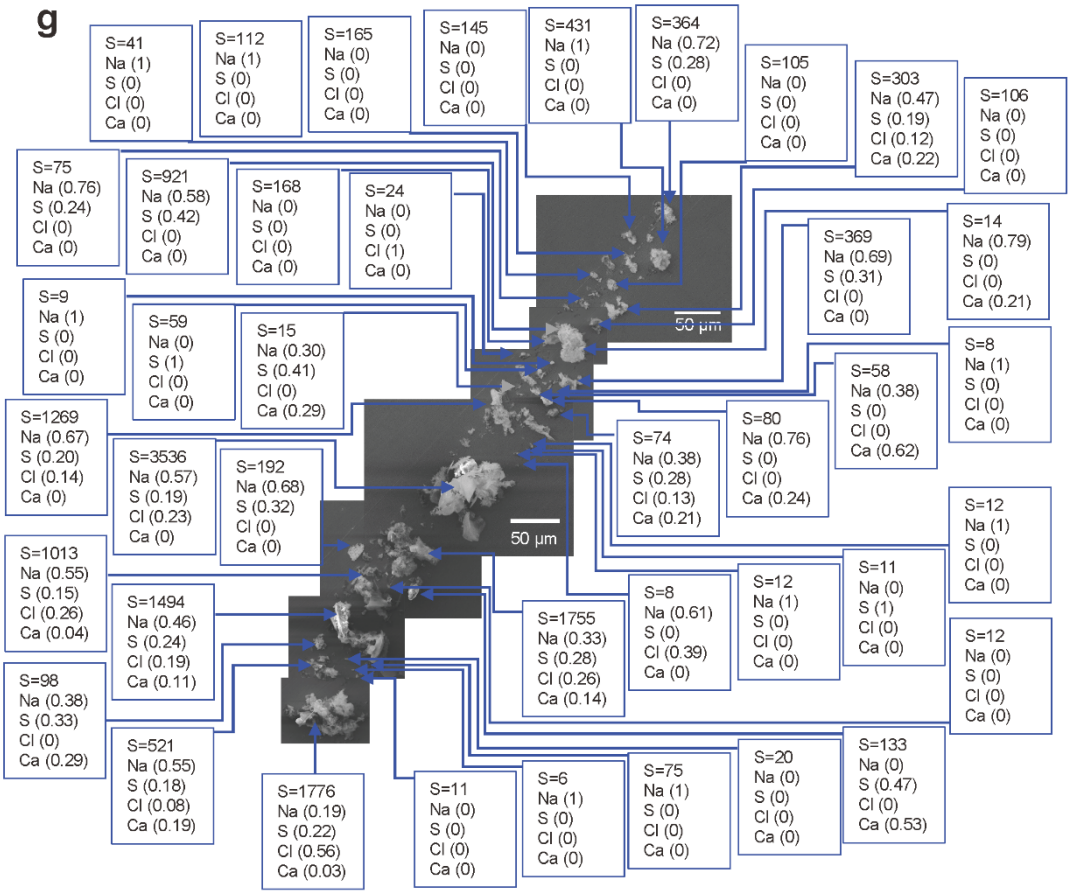
g
S=41
Na (1)
S (0)
Cl (0)
Ca (0)
S=112
Na (1)
S (0)
Cl (0)
Ca (0)
S=165
Na (0)
S (0)
Cl (0)
Ca (0)
S=145
Na (0)
S (0)
Cl (0)
Ca (0)
S=431
Na (1)
S (0)
Cl (0)
Ca (0)
S=364
Na (0.72)
S (0.28)
Cl (0)
Ca (0)
S=105
Na (0)
S (0)
Cl (0)
Ca (0)
S=303
Na (0.47)
S (0.19)
Cl (0.12)
Ca (0.22)
S=106
Na (0)
S (0)
Cl (0)
Ca (0)
S=75
Na (0.76)
S (0.24)
Cl (0)
Ca (0)
S=921
Na (0.58)
S (0.42)
Cl (0)
Ca (0)
S=168
Na (0)
S (0)
Cl (0)
Ca (0)
S=24
Na (0)
S (0)
Cl (1)
Ca (0)
S=369
Na (0.69)
S (0.31)
Cl (0)
Ca (0)
S=14
Na (0.79)
S (0)
Cl (0)
Ca (0.21)
S=9
Na (1)
S (0)
Cl (0)
Ca (0)
S=59
Na (0)
S (1)
Cl (0)
Ca (0)
S=15
Na (0.30)
S (0.41)
Cl (0)
Ca (0.29)
50 µm
S=8
Na (1)
S (0)
Cl (0)
Ca (0)
S=58
Na (0.38)
S (0)
Cl (0)
Ca (0.62)
S=1269
Na (0.67)
S (0.20)
Cl (0.14)
Ca (0)
S=3536
Na (0.57)
S (0.19)
Cl (0.23)
Ca (0)
S=192
Na (0.68)
S (0.32)
Cl (0)
Ca (0)
S=74
Na (0.38)
S (0.28)
Cl (0.13)
Ca (0.21)
S=80
Na (0.76)
S (0)
Cl (0)
Ca (0.24)
S=12
Na (1)
S (0)
Cl (0)
Ca (0)
S=1013
Na (0.55)
S (0.15)
Cl (0.26)
Ca (0.04)
S=1494
Na (0.46)
S (0.24)
Cl (0.19)
Ca (0.11)
S=1755
Na (0.33)
S (0.28)
Cl (0.26)
Ca (0.14)
S=8
Na (0.61)
S (0)
Cl (0.39)
Ca (0)
S=12
Na (1)
S (0)
Cl (0)
Ca (0)
S=11
Na (0)
S (1)
Cl (0)
Ca (0)
S=98
Na (0.38)
S (0.33)
Cl (0)
Ca (0.29)
S=521
Na (0.55)
S (0.18)
Cl (0.08)
Ca (0.19)
S=1776
Na (0.19)
S (0.22)
Cl (0.56)
Ca (0.03)
S=11
Na (0)
S (0)
Cl (0)
Ca (0)
S=6
Na (1)
S (0)
Cl (0)
Ca (0)
S=75
Na (1)
S (0)
Cl (0)
Ca (0)
S=20
Na (0)
S (0)
Cl (0)
Ca (0)
S=133
Na (0)
S (0.47)
Cl (0)
Ca (0.53)

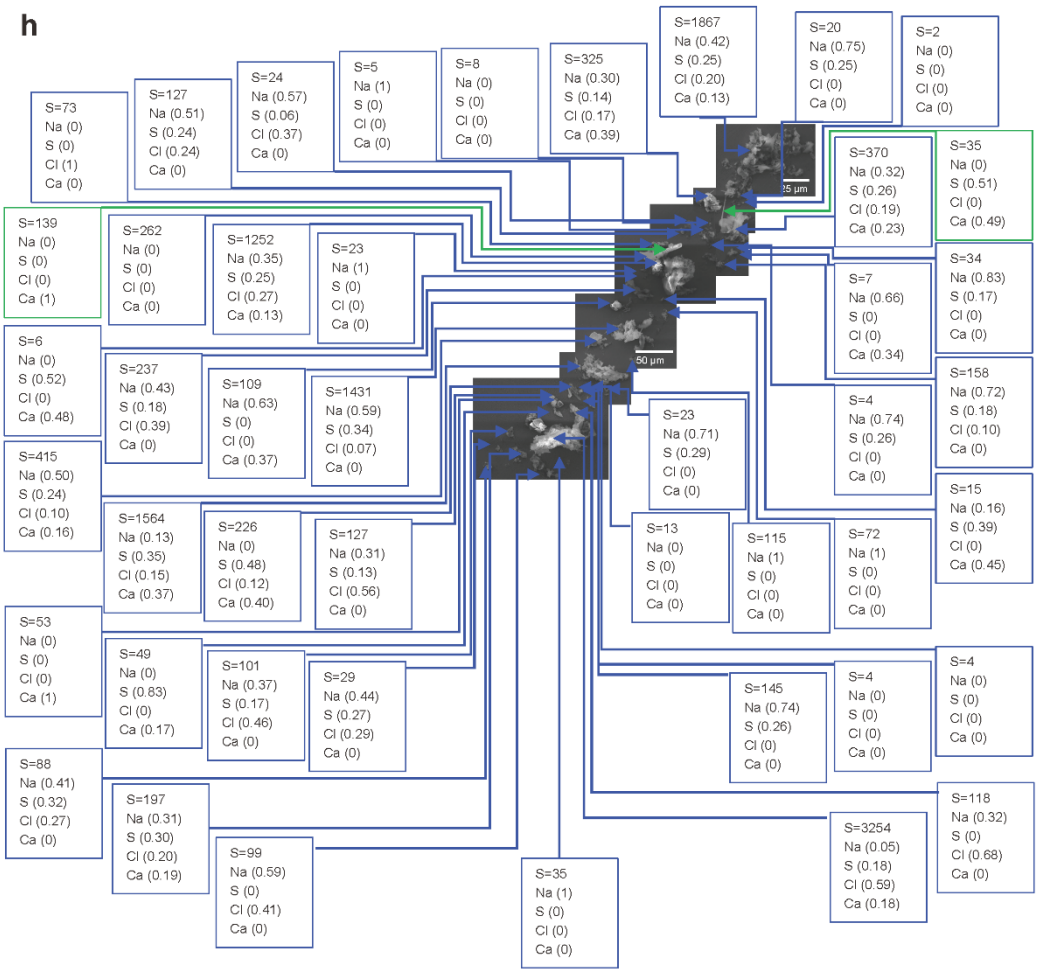
h
S=73
Na (0)
S (0)
Cl (1)
Ca (0)
S=127
Na (0.51)
S (0.24)
Cl (0.24)
Ca (0)
S=24
Na (0.57)
S (0.06)
Cl (0.37)
Ca (0)
S=5
Na (1)
S (0)
Cl (0)
Ca (0)
S=8
Na (0)
S (0)
Cl (0)
Ca (0)
S=325
Na (0.30)
S (0.14)
Cl (0.17)
Ca (0.39)
S=1867
Na (0.42)
S (0.25)
Cl (0.20)
Ca (0.13)
S=20
Na (0.75)
S (0.25)
Cl (0)
Ca (0)
S=2
Na (0)
S (0)
Cl (0)
Ca (0)
S=370
Na (0.32)
S (0.26)
Cl (0.19)
Ca (0.23)
S=35
Na (0)
S (0.51)
Cl (0)
Ca (0.49)
S=139
Na (0)
S (0)
Cl (0)
Ca (1)
S=262
Na (0)
S (0)
Cl (0)
Ca (0)
S=1252
Na (0.35)
S (0.25)
Cl (0.27)
Ca (0.13)
S=23
Na (1)
S (0)
Cl (0)
Ca (0)
S=7
Na (0.66)
S (0)
Cl (0)
Ca (0.34)
S=34
Na (0.83)
S (0.17)
Cl (0)
Ca (0)
S=6
Na (0)
S (0.52)
Cl (0)
Ca (0.48)
S=237
Na (0.43)
S (0.18)
Cl (0.39)
Ca (0)
S=109
Na (0.63)
S (0)
Cl (0)
Ca (0.37)
S=1431
Na (0.59)
S (0.34)
Cl (0.07)
Ca (0)
S=4
Na (0.74)
S (0.26)
Cl (0)
Ca (0)
S=158
Na (0.72)
S (0.18)
Cl (0.10)
Ca (0)
S=415
Na (0.50)
S (0.24)
Cl (0.10)
Ca (0.16)
S=23
Na (0.71)
S (0.29)
Cl (0)
Ca (0)
S=1564
Na (0.13)
S (0.35)
Cl (0.15)
Ca (0.37)
S=226
Na (0)
S (0.48)
Cl (0.12)
Ca (0.40)
S=127
Na (0.31)
S (0.13)
Cl (0.56)
Ca (0)
S=13
Na (0)
S (0)
Cl (0)
Ca (0)
S=115
Na (1)
S (0)
Cl (0)
Ca (0)
S=72
Na (1)
S (0)
Cl (0)
Ca (0)
S=15
Na (0.16)
S (0.39)
Cl (0)
Ca (0.45)
S=53
Na (0)
S (0)
Cl (0)
Ca (1)
S=49
Na (0)
S (0.83)
Cl (0)
Ca (0.17)
S=101
Na (0.37)
S (0.17)
Cl (0.46)
Ca (0)
S=29
Na (0.44)
S (0.27)
Cl (0.29)
Ca (0)
S=145
Na (0.74)
S (0.26)
Cl (0)
Ca (0)
S=4
Na (0)
S (0)
Cl (0)
Ca (0)
S=4
Na (0)
S (0)
Cl (0)
Ca (0)
S=88
Na (0.41)
S (0.32)
Cl (0.27)
Ca (0)
S=197
Na (0.31)
S (0.30)
Cl (0.20)
Ca (0.19)
S=99
Na (0.59)
S (0)
Cl (0.41)
Ca (0)
S=35
Na (1)
S (0)
Cl (0)
Ca (0)
S=3254
Na (0.05)
S (0.18)
Cl (0.59)
Ca (0.18)
S=118
Na (0.32)
S (0)
Cl (0.68)
Ca (0)
50 µm

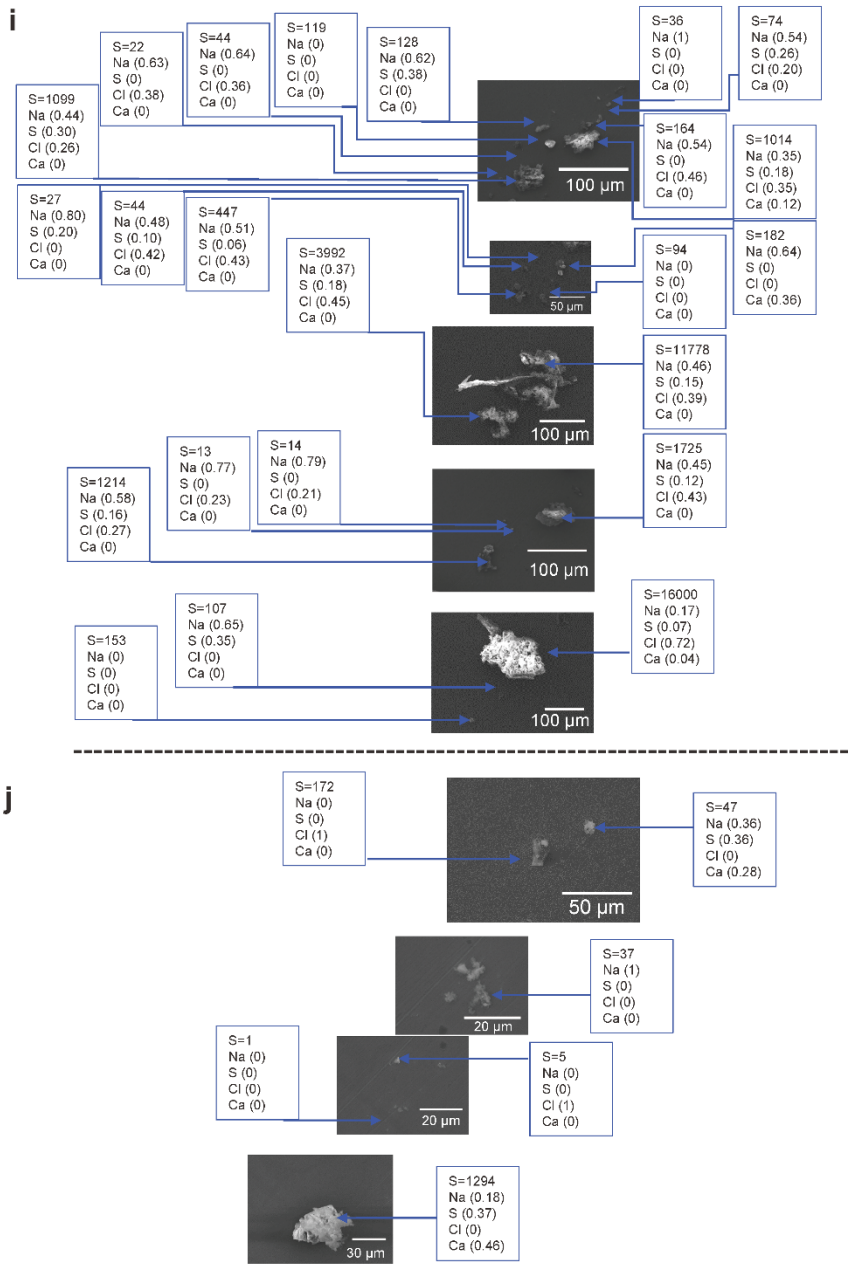
i
S=1099
Na (0.44)
S (0.30)
Cl (0.26)
Ca (0)
S=22
Na (0.63)
S (0)
Cl (0.38)
Ca (0)
S=44
Na (0.64)
S (0)
Cl (0.36)
Ca (0)
S=119
Na (0)
S (0)
Cl (0)
Ca (0)
S=128
Na (0.62)
S (0.38)
Cl (0)
Ca (0)
S=36
Na (1)
S (0)
Cl (0)
Ca (0)
S=74
Na (0.54)
S (0.26)
Cl (0.20)
Ca (0)
100 µm
S=164
Na (0.54)
S (0)
Cl (0.46)
Ca (0)
S=1014
Na (0.35)
S (0.18)
Cl (0.35)
Ca (0.12)
S=27
Na (0.80)
S (0.20)
Cl (0)
Ca (0)
S=44
Na (0.48)
S (0.10)
Cl (0.42)
Ca (0)
S=447
Na (0.51)
S (0.06)
Cl (0.43)
Ca (0)
S=3992
Na (0.37)
S (0.18)
Cl (0.45)
Ca (0)
50 µm
S=94
Na (0)
S (0)
Cl (0)
Ca (0)
S=182
Na (0.64)
S (0)
Cl (0)
Ca (0.36)
100 µm
S=11778
Na (0.46)
S (0.15)
Cl (0.39)
Ca (0)
S=1214
Na (0.58)
S (0.16)
Cl (0.27)
Ca (0)
S=13
Na (0.77)
S (0)
Cl (0.23)
Ca (0)
S=14
Na (0.79)
S (0)
Cl (0.21)
Ca (0)
100 µm
S=1725
Na (0.45)
S (0.12)
Cl (0.43)
Ca (0)
S=153
Na (0)
S (0)
Cl (0)
Ca (0)
S=107
Na (0.65)
S (0.35)
Cl (0)
Ca (0)
100 µm
S=16000
Na (0.17)
S (0.07)
Cl (0.72)
Ca (0.04)
j
S=172
Na (0)
S (0)
Cl (1)
Ca (0)
50 µm
S=47
Na (0.36)
S (0.36)
Cl (0)
Ca (0.28)
20 µm
S=37
Na (1)
S (0)
Cl (0)
Ca (0)
S=1
Na (0)
S (0)
Cl (0)
Ca (0)
20 µm
S=5
Na (0)
S (0)
Cl (1)
Ca (0)
30 µm
S=1294
Na (0.18)
S (0.37)
Cl (0)
Ca (0.46)

Fig. S1. Photomicrographs and compositions of inclusions in the last region of refreezing in the 2012 ice layer (4.370–4.390 m). The map at the top left shows the spatial distribution of inclusions, grouped into seven sections that are enlarged separately (a–j). For each inclusion, a small box gives the inclusion cross-sectional area S (μm^2) and the atomic fraction of each element (Na, S, Cl, Ca). Nearly all are particle type and marked as such with a blue frame on the box. The two red boxes in (a) and one in (c) indicate rod type, whereas the three green boxes in (h) indicate columnar.